UNIVERSITY OF CAPE TOWN

Development of An Efficient Finite Volume Computational Platform For The Simulation of Complex Flows of Complex Fluids Governed By The Rolie-Poly Model

Jade Gesare Abuga

Supervisor: Dr.Tiri Chinyoka

Thesis Presented for the Degree of
DOCTOR OF PHILOSOPHY
in the Department of Mathematics and Applied Mathematics
University of Cape Town

March 2019

Declaration

I, Jade Gesare Abuga, do hereby declare that this Ph.D thesis entitled "Development of an efficient finite volume computational platform for the simulation of complex flows of complex fluids governed by the Rolie-Poly model" is my own unaided work, save for that which is properly acknowledged.
It is being submitted for the degree of DOCTOR OF PHILOSOPHY at the University of Cape Town. It has not been submitted before for any degree or examination in any other University.

Signed: Signed by candidate

Date: 15^{th} March 2019

Acknowledgement

I wish to express my sincere appreciation to all those who were instrumental in one way or another to this study.

Words cannot express my sincere gratitute to my supervisor, Dr.Tiri, for his consistent and untiring guidance, advice and useful critiques of this research work.

Special thanks go to the Organisation for Women in Science for the Developing world (OWSD) for awarding me a scholarship that financed studying and living expenses throughout the course of this study. Their travel grants made conference attendance possible where, through networking, I garnered valuable information for my studies.

I acknowledge the support and resources from the Center of High Performance Computing (CHPC) at Rosebank, Cape Town. Special thanks to Dr. Andrew Gill for his guidance. I also acknowledge UCT High Perfomance Computing (HPC) facility for their resourses.

My sincere thanks go to the staff at the Department of Mathematics at UCT for their willingness to help with all the administrative processes and to my colleagues in room M4.02 for their encouragement, brilliant comments, suggestions and the numerous discussions that we had.

I would also like to sincerely thank my "family" in Cape Town, the Aritos, the Nyamwanges, the Christones, the Safaris, Karen, Joshua, Albert, Billy, Sarah, Joan, Lydia, Terry, Winnie, Ruth, Robert, Sandra, Janet and Prof. Himonga for the time they took to encourage and support me. They made my stay in Cape Town pleasant.

Words can not express how grateful I am to my parents-in-law, Mr. and Mrs. Abuto, for their encouragement and prayers.

I also wish to express my earnest gratitude to my parents, Mr. and Mrs. Nyakang'o, and my siblings Viberti, Edith and Dora for their boundless support and continuous encouragement throughout my years of study and through the process of researching and writing this thesis. This accomplishment would not have been possible without them. A special gratitude to my beloved husband, Edgar Abuto for supporting me in everything, and especially encouraging me throughout this

experience and to my beloved sons, Gavin and Gavril, for always cheering me on. Above all, this would have been impossible without the sustaining power of God. I am thankful for His mercies and grace.

UNIVERSITY OF CAPE TOWN

Abstract

Faculty of Science

Department of Mathematics and Applied Mathematics

Doctor of Philosophy

by Jade Gesare Abuga

ABSTRACT

The flow of non-Newtonian fluids, also known as complex fluids, is an important area of fluid mechanics due to their applications in industries such as food processing, mining, chemical and plastic industries. It is therefore essential to understand the flow and general behaviour of such fluids. Examples of these include polymeric liquids (both solutions and melts), immiscible polymer blends, emulsions, suspensions of rigid and deformable particles (such as biological cells, capsules or lipid vesicles) and colloidal dispersions.

Polymer melts are a category of fluids known as viscoelastic fluids and it is only recently that different forms of constitutive equations derived as simplified versions of molecular reptation-based models have been developed to describe molten polymers. The most adept mathematical models being the tube-based models which are derived from the Doi-Edwards tube-based model.

These constitutive equations are able to replicate experimental data is some fairly complex flows but are not able to do so in some cases, shear-banding phenomena being one of them. Under certain flow conditions, some complex fluids have been shown to exhibit different shear bands in the flow field due to flow-induced material non-homogeneities. It is becoming increasingly clear that non-homogeneities should not be ignored in polymers or other complex fluids since flow-induced non-homogeneities may, in some instances, be as important as the complex rheology in differentiating the flow behaviour of Newtonian and complex fluids.

Thus, with the use of technology to simulate fluid flows, there has been an increase in the research towards viscoelastic models and shear banding. This has also led to an increase in the development of CFD tools to solve such flows. One of the CFD tools is the OpenFOAM CFD viscoelastic solver that has already been developed. Therefore, the development of an efficient finite volume computation platform for complex flows governed by the Rolie-Poly constitutive equation has been presented in this thesis. The test cases of the lid-driven cavity flow and the planar 4:1 contraction flow were used to validate the solver which was used with the OpenFOAM CFD package. Discrete Elastic Viscous Stress Splitting (DEVSS) technique and the Log-conformation Reformulation (LCR) methodology of Fattal

and Kupferman were employed to stabilise the numerical algorithm at high Weissenberg number.

For the 4:1 planar contraction flow, it is observed that the numerical results using the LCR stabilazation technique are in good agreement for a range of Weissenberg numbers whereas the DEVSS method shows good agreement for low Weissenberg numbers. The numerical results for the lid-driven cavity flow are in good agreement with the existing literature for low Weissenberg numbers for both stabilization techniques.

In the course of this thesis however, capacity to deal with Rolie-Poly constitutive equation was added to the rheoTool which is a tool box for simulation viscoelastic fluid flows in OpenFOAM. A subsequent comparison of the numerical results with those from the rheoTooL solver show good agreement.

Furthermore, this thesis uses a two-fluid model by coupling the stress to concentration equation to study the shear banding phenomena in Rolie-Poly fluid flow. Validation is done by comparing existing literature of shear bands using the Giesekus and Johnson-Segalman constitutive equations. The numerical results show good agreement with existing literature for the DEVSS stabilization technique.

Contents

List of Figures

List of Tables

Dedicated to my parents

Chapter 1

Introduction

1.1 INTRODUCTION TO RHEOLOGY AND COMPLEX FLUIDS

The term rheology means the flow of matter. It is a term that was thought up in 1920 at Lafayette College situated in Indiana USA by Professor Eugene Bingham. It was motivated by the excerpt "ta panta rhei" to mean everything flows. It thus endorses the idea that everything has a time scale, and given enough time, everything will flow [8].

Thus, it is not easy to classify materials as solids or liquids since there is no clear distinction. This is due to the fact that this distinction is dependent on the relative time of the experiment or observation and the time scale of the material concerned or relaxation. The time scale of a material is the time required by the material to make adjustments to the stresses or deformations applied.

Thus, some materials act like liquids or solids depending on the time scale. An example of such a material is the "silly putty". It is a silicone material. The putty flows slowly over a long time scale, thus behaving like a liquid. However, it will behave like a solid on shorter time scales. For example, if a ball of it is dropped on the floor, it will bounce back and when given a sharp blow, it will break [9].

The ratio of the time of relaxation to that of observation is a well-defined non-dimensional number called the Deborah number. For small values of Deborah

number, the material will be classified as a viscous fluid and if it is a large value, the material will then be characterized as a solid. For values that are in between, the material will be characterized as a complex fluid.

There is much academic and industrial attention attracted to Rheology especially for complex fluids since a comprehensive study is a key step in defining the composition, standard of the complete product and the outcome when different parameters are applied. They are designated as non-Newtonian because their mechanical behaviour does not fit the pattern of a classical Newtonian fluid.

All Newtonian fluids follow the Newtonian postulate of the linear relationship between the stress, τ, and shear rate,γ, in simple shear. That is to say, the shear stress τ is proportionate to the rate of shear γ, for all Newtonian fluid flow at constant temperature and pressure, in simple shear. The constant of proportionality is called the dynamic viscosity, η [10]. Non-Newtonian flows however cannot be described by all encompassing laws as Newtonian flows.

1.2 NEWTONIAN FLUIDS

Newtonian fluids can be described as those that follow "Newton's law of viscosity" which states that "the shearing force given per unit area is proportional to the shear rates" [11]. It is expressed in tensor index notation as:

$$\tau_{21} = \eta_0 \frac{\partial u_1}{\partial x_2} \tag{1.1}$$

Newtonian fluids tend to manifest a constant viscosity at all shear rates.

Thus, for a fluid between two plates, one moving and the other fixed (see Figure 1.1), the velocity will produce a corresponding force whose magnitude is indirectly proportional to distance between the plates but directly proportional to the velocity and area being given by:

$$F = \mu A \frac{\delta U}{\delta y} \tag{1.2}$$

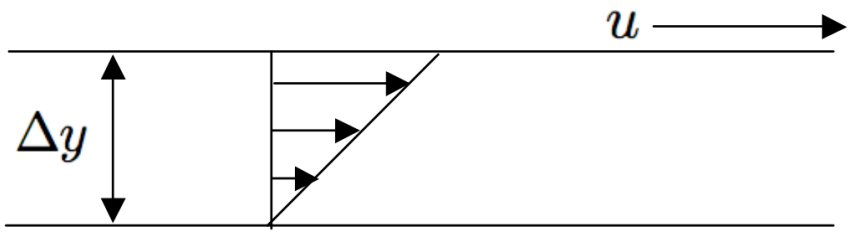

FIGURE 1.1: Fluid flow

There is a linear relationship between the shear stress τ and the shear rate γ and is given as

$$\tau = \eta * \gamma \tag{1.3}$$

where η is the viscosity. The viscosity for Newtonian fluids at constant temperature, pressure and concentration does not vary. Most common fluids such as water and oil, glycerine, gasoline, alcohol, air and thin motor oils are Newtonian.

1.3 NON-NEWTONIAN FLUIDS

Non-newtonian fluids can generally be described as fluids that do not follow the Newtonian constitutive equation given in Equation 1.1. The shear stress τ and shear rate γ relationship is non-linear, thus, the viscosity is not a given value but a rather, it varies depending on the shear stress, τ, or shear rate, γ. The shear stress τ and γ relationship is thus given as:

$$\eta(\gamma) = \frac{\tau}{\gamma} \tag{1.4}$$

Generally, Non-newtonian fluids can be sub-divided broadly into three groups [10].

1. Time-independent fluids (purely viscous or generalized Newtonian fluids (GNF))
2. Time-dependent fluids
3. viscoelastic fluids

1.3.1 Time-Independent Fluids

1.3.1.1 Generalized Newtonian Fluids

These are fluids whose current value of shear stress τ dictate the value of the shear rate,γ. The stress tensor is given as [12]:

$$\tau = 2\eta\mathbf{D} \tag{1.5}$$

where $\mathbf{D}$ is the rate of deformation tensor given as:

$$\mathbf{D} = \frac{1}{2}[\nabla v + (\nabla v)^T] \tag{1.6}$$

η is the apparent viscosity and it depends on the second principal invariant which can be written as the magnitude of D [13]:

$$|\mathbf{D}| = \sqrt{2\mathbf{D} : \mathbf{D}^T} = \sqrt{2\sum_i \sum_j D_{ij}^2} = \gamma \tag{1.7}$$

The common models are:

- Power law model whose equation is given as:

$$\mu(\gamma) = K\gamma^(m-1) \tag{1.8}$$

  where K is the consistency factor and m is the index of the power law

- Bird-carreau model whose equation is given as:

$$\mu - \mu_\infty = \frac{\mu_0 - \mu_\infty}{[1 + (\lambda\gamma)^2]^{(m-1)/2}} \tag{1.9}$$

  where λ is the relaxation time of the material.

- Yasuda and cross model whose equation is given as:

$$\mu - \mu_\infty = \frac{\mu_0 - \mu_\infty}{[1 + (\lambda\gamma)^a]^{(m-1)/a}} \tag{1.10}$$

where a is the curve-fit parameter [14]

1.3.1.2 Viscoplastic fluids

These are fluids which behave like elastic solids for an applied stress that is less than the threshold stress. The threshold stress is also called the yield stress, τ_y. Once the stress that is applied exceeds more than the yield stress, the fluid will move. However,once the stress is withdrawn, the fluid reverts to its former state. The three constitutive equations that are used to model flow behaviour of viscoplastics are:

1. Bingham model
2. Herschel-Bulkley model
3. Casson model

Bingham model follows Newton's law of viscosity as it flows since the relationship between the shear stress, τ and shear rate, γ is linear. Herschel-Bulkley and Casson model predicts a non-linear relationship. Examples of viscoplastic fluids include mayonnaise, toothpaste, concrete, radioactive nuclear waste sludge and some paints[15].

1.3.1.3 Purely viscous

Purely viscous fluids can either be shear-thinning(pseudoplastic) or shear thickening (dilatant). The apparent viscosity becomes constant, η_0 and η_∞, at very low and very high shear rates respectively. They are referred to as the first and second Newtonian region. Examples of these fluids include cornstarch paste, tomato sauce and glass melts.[11].

Shear-thinning fluids are those whose viscosity η decreases with an increase in the shear rate, γ. Figure 1.2 is a plot of the shear stress against shear rate curve for the different viscous fluids and Newtonian fluids. For shear-thickening, also

known as antithixotropic fluids, an increase in viscosity, η, causes an increase in shear rate, γ. For such fluids, plotting a shear stress τ verses shear rate γ curve would curve upward as shown in Figure 1.2 taken from [16].

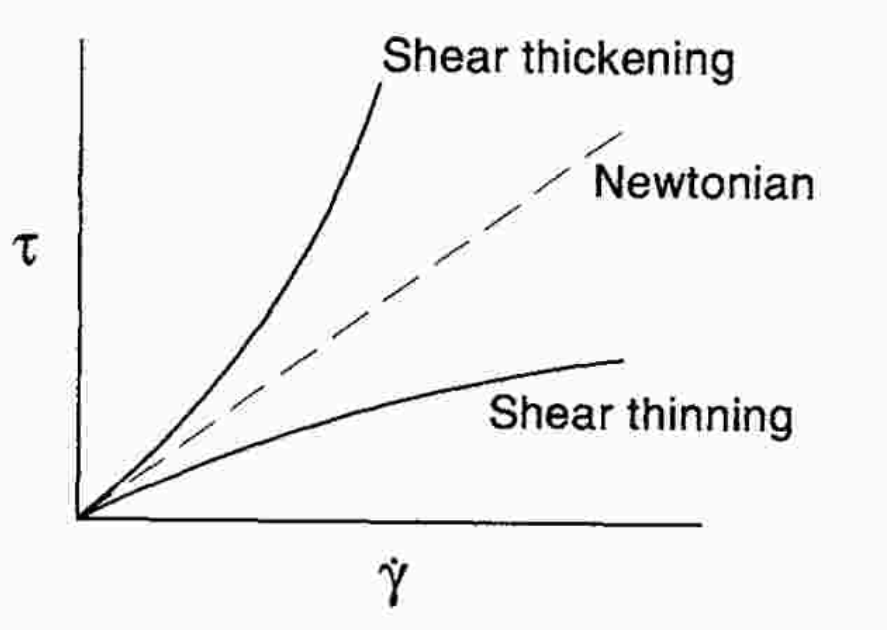

FIGURE 1.2: Plot of shear stress τ versus shear rate γ
(Reprinted from [16])

Examples include corn starch and clay slurries. The most popular form for the viscosity is the Carreau model given as:

$$\eta\gamma = \eta_\infty + \frac{\eta_0 - \eta_\infty}{(1 + \Gamma^2\gamma)^(1-n)/s} \tag{1.11}$$

where η_∞ is the infinite shear-rate viscosity, η_0 is the zero shear rate viscosity, n is the power law index and Γ is constant whose dimension is time [17].

1.3.2 Time-dependent fluids

These are fluids whose shear rate and time dictates the value of apparent viscosity. Therefore, for fixed shear rate and temperature, the stress will increase or decrease consistently with respect to time. In some cases, once the shear stress has been stopped, the viscosity will recover its original value. They are categorized as

1. Thixotropic fluids

2. Rheopectic fluids

A fluid whose shear stress diminishes with time is known as a thixotropic whereas those whose shear stress increases monotonically with time are known as rheopectic fluids also known as antithixotropic fluids.

1.3.3 Viscoelastic Fluids

Viscoelastic fluids can function as either elastic solids or a viscous fluids depending on the circumstances. Such fluids typically have a high molecular weight and their stress responses are as a result of not only their contemporaneous distortions but also on the record of their past deformations. They have some ability to stock and regain shear energy, exhibit stress relaxation and creep deformation[18]. At low deformations and low deformation rates, viscoelastic fluids are aptly modelled by linear viscoelastic models. At higher stress levels, the materials exhibit non-linear viscoelastic behaviours. Some examples include polymer solutions and melts, dense colloidal suspensions (such as corn starch in water), and suspensions of rigid and deformable particles (such as biological cells, capsules or lipid vesicles).The basic flow phenomena that are associated with the viscoelastic nature of fluids include rod-climbing and die or extrudate swell and tubeless siphon among others.

1.3.3.1 Linear viscoelastic fluids

A linear viscoelastic fluid exhibit properties of both elastic solids and Newtonian fluids. The elastic solids are denoted by springs whereas the Newtonian fluids by dashpots. The stress-strain relationship of an elastic solid under simple shear is modelled using Hooke's law and is given as:

$$\tau_e = k\gamma_e \tag{1.12}$$

where τ_e is the elastic stress, k is the spring constant and γ_e is the elastic strain. The stress-strain for a Newtonian fluid is given as:

$$\tau = \eta_0 \gamma \tag{1.13}$$

A linear viscoelastic fluid is then modelled using a combination of springs and dashpots using the Boltzmann superposition principle in which the effect of a compound cause is obtained by summing up the effects of the individual causes. General linear viscoelastic models have a limitation in that they are unable to describe normal stress phenomena in simple shear flow thus non-linear viscoelastic models are required. This is because normal stresses need to be accounted for.

1.3.3.2 Non-linear viscoelastic

Viscoelastic fluids display various flow behaviours like rod-climbing (Weissenberg effect), extrudate swell, elastic recoil and tubeless siphons. The normal stresses are responsible for this effects thus the need for non-linear viscoelastic models [12, 19]. To model these fluids, there are broadly three approaches that have been used [20]. These are;

- Dilute solution theory where the polymer molecules, modelled as a chain of beads and springs or rods, are treated individually. It is also known as the bead-spring model[21, 22]
- Network theory where the polymer molecules are deemed as an interconnected group of springs connected permanently at junction points which allows interaction between the polymer and flow to take place. Consequently, polymers then move together throughout[23]. An example of such a model is Phan-Thien-Tanner[24]
- Reptation theory is an amalgam of Dilute solution and Network theory. The polymer molecules are treated individually but each is contained in an imaginary tube. Tube-based models are derived using this concept [25]. An example of such a model is the Rolie-Poly model [26]

The constitutive equations use the spring-dashpot Maxwell models [27, 28] of linear viscoelastic, classified as either Upper or Lower convected Models, for the time derivative. They upper and lower convected derivatives are given as:

$$\overset{\triangledown}{\mathbf{T}} = \frac{D\mathbf{T}}{Dt} - \mathbf{T} \cdot (\nabla \mathbf{v})^T - \nabla \mathbf{v} \cdot \mathbf{T} \tag{1.14}$$

and

$$\overset{\triangle}{\mathbf{T}} = \frac{DT}{Dt} + \mathbf{T} \cdot (\nabla \mathbf{v})^T + \nabla \mathbf{v} \cdot \mathbf{T} \tag{1.15}$$

Another type of derivative used is the The Gordon-Schowalter which is given as:

$$\overset{\square}{\mathbf{T}} = \frac{D\mathbf{T}}{Dt} - \mathbf{T} \cdot (\nabla \mathbf{v})^T - \nabla \mathbf{v} \cdot \mathbf{T} + \eta(\mathbf{T} \cdot \mathbf{D} + \mathbf{D} \cdot \mathbf{T}) \tag{1.16}$$

where the material derivative is given as:

$$\frac{D\mathbf{T}}{Dt} = \frac{\partial \mathbf{T}}{\partial t} + \ \mathbf{v} \cdot \nabla \mathbf{T} \tag{1.17}$$

The constitutive equation that will be focussed on in this thesis is the Rolie-Poly, which stands for ROuse LInear Entangled POLYmers. It is a tube-based model. Tube-based models are proficient for modelling the dynamics of entangled polymer melts as they take into account mechanisms such as reptation, chain stretch, contour length fluctuations and convective and reptation-driven constraint release. The Rolie-Poly models incorporates three of the mechanisms which are chain retraction and convective constraint release and reptation. The equations is given as:

$$\frac{D\mathbf{T}}{Dt} = -\frac{1}{\lambda}(\mathbf{T} - \mathbf{I}) - \frac{2(1 - \sqrt{3/tr\mathbf{T}})}{\lambda_R}\left[\mathbf{T} + \hat{B}\left(\frac{tr\mathbf{T}}{3}\right)(\mathbf{T} - \mathbf{I})\right] \tag{1.18}$$

where λ is the reptation relaxation time, λ_R is the rouse relaxation,$\hat{B}$ is the convective-constraint release, $\mathbf{I}$ is the unit tensor and tr denotes the trace of a tensor. Other differential constitutive model equations are presented in Table 1.1

TABLE 1.1: Differential viscoelastic constitutive models

Constitutive model	Equation
Oldroyd-B	$\mathbf{T} + \lambda \overset{\nabla}{\mathbf{T}} = 2\eta\mathbf{D}$
Giesekus	$\mathbf{T} + \lambda \overset{\nabla}{\mathbf{T}} + \alpha\mathbf{T}^2 = 2\eta\mathbf{D}$
Leonov	$\mathbf{T} + \lambda \overset{\nabla}{\mathbf{T}} + \frac{1}{2}\mathbf{T}^2 = 2\eta\mathbf{D}$
John-Segalman	$\mathbf{T} + \lambda \overset{\square}{\mathbf{T}} = 2\eta\mathbf{D}$
Phan-Thien-Tanner	$exp(\varepsilon\frac{\lambda}{\eta})\mathbf{T} + \lambda \overset{\square}{\mathbf{T}} = 2\eta\mathbf{D}$
FENE-P	$\left(1 + \frac{(3)/(1-3/L_k^2) + \lambda/\eta tr\mathbf{T}}{L_k^2}\right)\mathbf{T} + \lambda \overset{\nabla}{\mathbf{T}} = 2\frac{1}{(1-3/L_k^2)}\eta\mathbf{D}$
FENE-CR	$\left(\frac{L_k^2 + (\lambda_k)/(\eta)tr(\mathbf{T})}{(L_k^2-3)}\right)\mathbf{T} + \lambda \overset{\nabla}{\mathbf{T}} = 2\left(\frac{L_k^2 + (\lambda_k)/(\eta)tr(\mathbf{T})}{(L_k^2-3)}\right)\mathbf{D}$
EPTT	$exp\left(\frac{\varepsilon\lambda}{\eta}tr(\mathbf{T})\right)\mathbf{T} + \lambda \overset{\square}{\mathbf{T}} = 2\eta\mathbf{D}$
LPTT	$\left(1 + \frac{\varepsilon\lambda}{\eta}tr(\mathbf{T})\right)\mathbf{T} + \lambda \overset{\square}{\mathbf{T}} = 2\eta\mathbf{D}$

1.4 INTRODUCTION TO COMPUTATIONAL METHOD

The finite volume method (FVM) is a numerical method that is applied in evaluating and representing partial differential methods in the form of algebraic equations [29]. It is suited for elliptical, parabolic and hyperbolic problems. The advantages of using FVM for numerical simulation is that it can be used on arbitrary geometries and it leads to sturdy schemes. The feature that has made FVM indispensable to fluid mechanics problems due to the importance of the flux is that the numerical flux is conserved [30].

It is based on integration of equations using the divergence formula over a discretization cell which is often called the control volume. The control volumes are the elements obtained by partitioning the domain where the space variable lives. Once the integration is done, the set of equations is then discretized and the set of resulting equations is then solved exactly or approximately. Depending on whether the set of resulting equations are linear or non-linear, the methods used are direct or iterative solvers for linear equations and fixed point or Newton type methods for non-linear equations.[31].

To illustrate how the FVM works, a simple transport equation is used. The equation is given as:

$$\frac{\partial \rho\phi}{\partial t} + \nabla \cdot (\rho\phi\mathbf{u}) = \nabla \cdot (\Gamma\nabla\phi) + S_\phi \tag{1.19}$$

where Γ is the diffusion coefficient and S_ϕ is the source term. The first step is to obtain the control volume by dividing the domain into discrete partitions as shown in Figure 1.3.

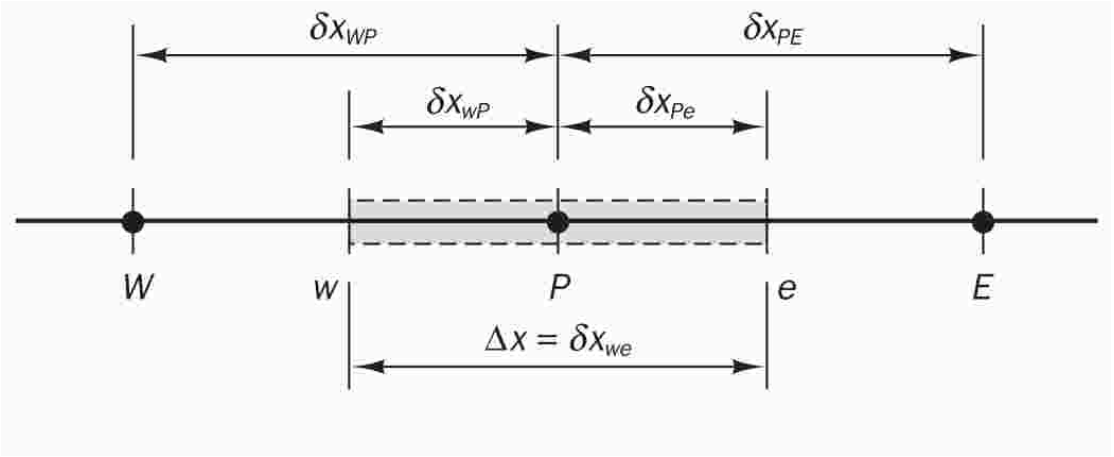

FIGURE 1.3: 1 D computation grid (reprinted from [1])

All the nodes are then referenced to using their position with regards to a general nodal point P, i.e., the nodes to the east and west of the point P are identified E and W respectively. w and e is the west side face and east side face of the control volume. δx gives the distance between the different points indicated by the subscript.

The second step involves discretizing the transport equation 1.19 over the control volume by first integrating over a control volume, cv, to obtain

$$\int_{cv} \frac{\partial \rho\phi}{\partial t} dV + \int_{cv} \nabla \cdot (\rho\phi\mathbf{u}) dA = + \int_{cv} \nabla \cdot (\Gamma\nabla\phi) dv + \int_{cv} S_\phi dV \tag{1.20}$$

A divergence theorem is then applied to Equation 1.20 to obtain:

$$\frac{\partial}{\partial t} \int_{cv} \rho\phi dV + \int_A \mathbf{n} \cdot \rho\phi\mathbf{u} dA = + \int_A \mathbf{n} \cdot (\Gamma\nabla\phi) dA + \int_{cv} S_\phi dV \tag{1.21}$$

1.5 SPATIAL DISCRETIZATION

Different schemes can be used to obtain the discretization of equations. For the numerical results to be realistic, there are three properties that a dicretization scheme must have. These are:

- Conservativeness: This implies that the flux of ϕ leaving a control volume and entering an adjacent one through the same face must be equal.
- Boundedness: A sign that discretized equations are bounded is that the coefficients have the same sign which is usually positive. This infers that if ϕ at one node is increased, the result will be an increase of ϕ at neighbouring nodes.
- Transportiveness: It can be defined as the relationship between the magnitude of the peclet number and the directionality of influencing.

1.5.0.1 Central differencing scheme

The central-differencing scheme obtains the variable face value, ϕ_f, by considering the differential operator in the central node of the considered patch. For an equally spaced grid, the property cell values are written as :

$$\phi_e = (\phi_P + \phi_E)/2$$

$$\phi_w = (\phi_W + \phi_P)/2$$

Therefore, considering a steady one-dimensional convection-diffusion equation excluding the source term, Equation 1.20 reduces to

$$\int_{cv} \nabla \cdot (\rho\phi\mathbf{u})dA = + \int_{cv} \nabla \cdot (\Gamma\nabla\phi)dv \tag{1.22}$$

Using the cell face values and dicretizing using the central difference method, Equation 1.22 is then given as:

$$F_e\frac{\phi_E+\phi_P}{2}-F_w\frac{\phi_W+\phi_P}{2}=D_e(\phi_E-\phi_P)-D_w(\phi_P-\phi_W) \tag{1.23}$$

where $F=\rho u$ and $D=\Gamma/\delta x$.

The advantages of using central difference scheme are that it is easy to understand and implement, uses less computer time per time step and when compared to first order upwind, it is more accurate to second-order for peclet number less than 2. Peclet number is obtained by getting the ratio of advective transport rate to that of diffusive transport rate.

1.5.0.2 Upward differencing scheme

The upward differencing scheme is best used for hyperbolic problems since information is disseminated as the waves travel. It takes into consideration the direction of the flow as the cell value of ϕ_f is equated to the value of the upstream node. Considering Figure 1.3, if the flow is from left to right i.e the positive direction, the cell values are given as: $\phi_w=\phi_W$ and $\phi_e=\phi_P$, thus discretizing using upward differencing scheme, Equation 1.22 becomes:

$$F_e\phi_P-F_w\phi_W=D_e(\phi_E-\phi_P)-D_w(\phi_P-\phi_W) \tag{1.24}$$

If the flow is from right to left, i.e the negative direction, the cell values are given as $\phi_w=\phi_P$ and $\phi_e=\phi_E$ and thus, the discretized equation becomes:

$$F_e\phi_E-F_w\phi_P=D_e(\phi_E-\phi_P)-D_w(\phi_P-\phi_W) \tag{1.25}$$

The upwind differencing scheme is as accurate as the central differencing scheme since it is first-order accurate. However, it always gives a solution that is bounded, consequently giving a physically correct solution.

1.5.0.3 Hybrid differencing scheme

The hybrid scheme combines the central differencing scheme's accuracy with the upwind differencing scheme's stability. The hybrid scheme uses a piecewise formula such that the central differences are used for peclet number less than 2 and for greater than 2, the upwind differencing scheme is used. The formula is based on the local peclet number, Pe, such that the net flux per unit area through the west face is given as

$$q_w = F_w \left[\frac{1}{2}\left(1 + \frac{2}{Pe_w}\right)\phi_w + \frac{1}{2}\left(1 - \frac{2}{Pe_w}\right)\phi_P\right] \quad for \quad -2 < Pe_w < 2$$

$$q_w = F_w \phi_W \quad Pe_w \geq 2$$

$$q_w = F_w \phi_P \quad Pe_w \leq 2 \tag{1.26}$$

1.5.0.4 Power law scheme

The advantage of the power law scheme is that it will yield a better outcome than the hybrid scheme. The diffusion is set in a way as to depend on the peclet number. For peclet number greater than 10, the diffusion is equated to zero, otherwise, a polynomial expression is used in assessing the flux. At the control volume in the west, the net flux per unit area is given as:

$$q_w = F_w \left[\phi_W - \frac{(1 - 0.1Pe_w)^5}{Pe_w}(\phi_P - \phi_W)\right] \quad for \quad 0 < Pe < 10$$

$$q_w = F_w \phi_W \quad for \quad Pe > 2 \tag{1.27}$$

1.5.1 Temporal discretization

The steady state problem that has been considered in the previous section has been discretized spatially. When considering unsteady state problems, the time derivatives need to be discretized. This is known as temporal discretization.

Consider Equation 1.20 given in the previous section. Integrating it with respect to time over a time-step and rewritting it we obtain:

$$\int_t^{t+\triangle t}\int_{cv}\frac{\partial\rho\phi}{\partial t}dVdt = \int_t^{t+\triangle t}\int_{cv}\nabla\cdot(\rho\phi\mathbf{u})dAdt\int_t^{t+\triangle t}\int_{cv}\nabla\cdot(\Gamma\nabla\phi)dVdt$$

$$+\int_t^{t+\triangle t}\int_{cv}S_\phi dVdt \tag{1.28}$$

or

$$\phi^{n+1}-\phi^n = \int_t^{t+\triangle t}\int_{cv}\nabla\cdot(\rho\phi\mathbf{u})dAdt\int_t^{t+\triangle t}\int_{cv}\nabla\cdot(\Gamma\nabla\phi)dVdt$$

$$+\int_t^{t+\triangle t}\int_{cv}S_\phi dVdt \tag{1.29}$$

The right hand side can be represented by a function $\int_t^{t+\triangle t} f(t,\phi(t))dt$ such that Equation 1.29 becomes:

$$\phi^{n+1} = \phi^n + \int_t^{t+\triangle t} f(t,\phi(t))dt \tag{1.30}$$

1.5.1.1 Explicit scheme

The explicit scheme approximates the integral using the values of f at the initial time t. Accordingly, using the explicit scheme yields to get the value of ϕ at time step $n+1$, Equation 1.30 gives:

$$\phi^{n+1} = \phi^n + f\left(t+\triangle t,\phi^n\right)\triangle t \tag{1.31}$$

Looking at Equation 1.31, it is clear that the right hand side has the old time step values. Therefore, the left hand side value is obtained by forward matching in time. One of the disadvantage of the explicit schemes is that to ensure stability,

a restriction on the time step is put which most often results in small time steps being used. Thus it becomes very expensive to ensure stability.

1.5.1.2 Implicit scheme

The implicit method approximates the value of ϕ using the values of f at the final time, $t + \triangle t$. We then have:

$$\phi^{n+1} = \phi^n + f(t + \triangle t, \phi^{n+1}(t)) \triangle t \tag{1.32}$$

Generally, such an equation will require an iterative procedure to solve for ϕ^{n+1} since the values of ϕ^{n+1} appear on both sides of Equation 1.32. The advantage of the implicit scheme is that for any time step size, the scheme is unconditionally unstable. An example of an implicit scheme in time is the Crank-Nicholson scheme which uses the central differencing scheme for spatial discretization

1.5.2 Solution algorithm for flows

1.5.2.1 SIMPLE

SIMPLE is an acronym for Semi-Implicit Method for Pressure-Linked Equations. It is a solution method where the velocity and pressure fields are solved singly and connecting them is attained through velocity and pressure corrections. On the first iteration, an approximate value of velocity is got after solving the momentum equation. It is at this first iteration that there is the largest local error approximation of the velocity field before the application of pressure corrections. However, local and global mass conservation is assured as the velocity field is corrected.
Starting with an initial velocity and pressure value denoted by using superscript, n, the momentum equation is solved. At any point during the iteration, the velocity and pressure values will be denoted using superscript *, the procedure is as follows:

- The initial velocity, pressure fields, u^n, v^n, p^n respectively, are used to work out the momentum equation to obtain velocity fields u* and v*.
- The velocity fields u* and v* obtained from the previous step are used to solve the pressure corrected equation.
- The pressure and velocity fields are then corrected.
- The corrected pressure and velocity fields are then used to solve all the other discretized transport equations.
- The process is stopped if there is convergence otherwise it will be repeated until there is convergence.

For unsteady flows, transient terms will be included in the discretized momentum equations and the pressure correction equation will contain terms that represent its transient behaviour. The same iterative procedure will be followed until there is convergence.

1.5.2.2 SIMPLER

SIMPLER algorithm which denotes SIMPLE-Revised is a modified version of SIMPLE algorithm. The difference is that the discretized equation for pressure is derived from the discretized continuity equation.

1.5.2.3 SIMPLEC

SIMPLEC denotes SIMPLE-Consistent. The steps followed in this algorithm are similar to those in the SIMPLE algorithm with the difference being that the momentum equations are worked out such that the less significant terms are omitted from the SIMPLEC velocity correction equations.

1.5.2.4 PISO

PISO is an acronym for Pressure Implicit with Splitting of Operators of Issa [32]. It is seen as an add-on version of the SIMPLE algorithm with an additional corrector step thus it has one predictor step and two corrector steps. The first 3 steps of the SIMPLE procedure are followed. The next step involves solving a another pressure correction equation. The pressure and velocity fields are then corrected and set. All the other discretized transport equations are then solved. The procedure will be repeated until there is a convergence.

1.6 OPENFOAM

OpenFOAM is an acronym for "Open Source Field Operation and Manipulations". It is an open source software that deals with continuum mechanics, including computational fluid dynamics.
It was first developed under the name FOAM in the year 1989 by Henry Weller. In December 2004, it was allowed as an Opensource software by Henry Weller, Chris Greenshields and Mattijs Jansens under the name OpenFOAM. However, in the same year there was a fork which was named OpenFOAM-extend and later renamed Foam-extend [33] founded by Jasak.
OpenFOAM is based on the Finite Volume Method (FVM) and used C++ as the programming language [34]. It is a collection of C++ libraries that contain executable applications which can be classified as solvers and utilities. The solvers, as the name suggests, are for solving a specific problem whereas the task of the utilities involves pre-processing and post-processing data [35].
In order to run an application, for example using OpenFOAM to solve a partial differential equation, one is required to create a case directory containing three subdirectories. The three subdirectories are [36]:

- Constant directory: It contains files that give the mesh description and those that list the physical properties required for the application.

- System directory: It contains three files that set the run control parameters, specify the discretization schemes to be used and files where the equation solvers, tolerances and algorithm are set.
- 'Time' directory: This contains files that specify initial and boundary conditions for the flow fields. More time directories are then created depending on the simulated time at which data is written.

One of the advantage of OpenFOAM is the ease with which users can create custom solvers since the syntax used for tensor operations and partial differential equations takes after the equation being solved. For example, the given Equation 1.33

$$\frac{\partial(\rho\mathbf{u})}{\partial t} + \nabla \cdot (\phi\mathbf{u}) - \mu\nabla^2\mathbf{u} = -\nabla p \tag{1.33}$$

will be represented by the code [37]:

```
solve
(
   fvm ::ddt(rho, U)
+   fvm ::div(phi,U)
-   fvm ::laplacian(mu,U)
== -   fvc::grad(p)
);
```

Due to the ease with which users can create custom solvers, there has been an increasing number of solvers added to OpenFOAM and Foam-extend. Particularly, of interest is the viscoelasticFluidFoam solver which was developed by Favero [38, 39].

Despite an increase in the development and use of computer technology in research, one of the problems that has plagued computational rheology for several decades is that of the high Weissenberg number problem (HWNP) [40]. It is the breakdown of numerical scheme once a critical value of the Weissenberg number is exceeded. The Weissenberg number is the ratio of the elastic to viscous forces.

To mitigate this, the viscoelastic solver applies the Discrete elastic viscous stress

spliting (DEVSS) stabilizing scheme. This is achieved by introducing a diffusion term to the momentum equation [41]. Considering Equation 1.34, the stabilized equation will finally be written as:

$$\frac{\partial(\rho\mathbf{u})}{\partial t} + \nabla\cdot(\phi\mathbf{u}) - (\eta_s + k)\nabla\cdot(\nabla\mathbf{u}) - \mu\nabla^2\mathbf{u} = -\nabla p - k\nabla\cdot(\nabla\cdot\mathbf{u}) \tag{1.34}$$

Another solver that deals with viscoelastic flows is the rheoFoam tool that was developed by Pimenta *et al.* It has an option of using the Log-conformation reformulation method that was developed by Fattal and Kuperfman [42, 43] to mitigate against the HWNP. Stabilizing using the LCR is done by designating the stress constitutive equation as a conformation tensor which is then replaced by a log representation.

The stress tensor is related to the conformation tensor by:

$$\tau = \frac{\eta_p}{\lambda}(\mathbf{c} - \mathbf{I}) \tag{1.35}$$

It is then diagonolized and used to change a variable in the constitutive model. It is given as:

$$\Psi = ln(\mathbf{c}) = \mathbf{R}ln(\Lambda)\mathbf{R}^T \tag{1.36}$$

$\mathbf{R}$ is the othorgonal matrix having the eigenvectors of A whereas Λ is the diagonal matrix having eigenvalues of A. Using the Oldroy-B constitutive equation given in Table 1.1, the log-conformation tensor will be given as:

$$\frac{\partial\Psi}{\partial t} + (\mathbf{u}\cdot\nabla)\Psi - (\Omega\Psi - \Psi\Omega) - 2\mathbf{E} = -\frac{1}{\lambda}(\mathbf{c} - \mathbf{I}) \tag{1.37}$$

and for a two-dimensional case:

$$\mathbf{R}(\nabla\mathbf{u})\mathbf{R} = \begin{Bmatrix} m_{11} & m_{12} \\ m_2 1 & m_{22} \end{Bmatrix} \tag{1.38}$$

$$E = \mathbf{R}\begin{Bmatrix} m_{11} & 0 \\ 0 & m_{22} \end{Bmatrix}\mathbf{R}^T \tag{1.39}$$

$$\Omega = \mathbf{R} \begin{Bmatrix} 0 & \omega_{12} \\ -\omega_{21} & 0 \end{Bmatrix} \mathbf{R}^T \tag{1.40}$$

$$\omega = \mathbf{R} \begin{Bmatrix} 0 & \zeta \\ -\zeta & 0 \end{Bmatrix} \mathbf{R}^T \tag{1.41}$$

where

$$\zeta = \frac{m_{12} + m_{21}}{\lambda_2 - \lambda_1} \tag{1.42}$$

The solution to Equation 1.37 is worked out in the viscoelasticFluidFoam solver and the conformation tensor recovered by getting the inverse of equation 1.36.

At the onset of present work, the viscoelasticFluidFOAM solver was lacking and still is lacking the Rolie-Poly constitutive relation, however in the course of this study, it was added in the rheoTool solver.

Therefore, the main intention of this work is incorporate the Rolie-Poly constitutive equation into the viscoelasticFluidFoam solver and to benchmark it using the planar 4:1 contraction flow and the lid-driven cavity. The present work seeks to also use the Rolie-Poly constitutive equation to look into the shear banding phenomena for simple planar shear flow.

Chapter 2

Benchmark solutions of the stabilized computations of flows of fluids governed by the Rolie-Poly constitutive model [1]

2.1 ABSTRACT

Recent studies demonstrate that flow-induced non-uniformities of concentration can trigger shear banding in the flow of certain viscoelastic fluids. These studies show that the driving mechanisms for such shear banding are related to the coupling of the polymer stresses to an inhomogeneous concentration profile. The Rolie-Poly (RP) viscoelastic constitutive model has been used in such studies since it has been comprehensively subjected to extensive experimental validation with regards to shear banding and has the demonstrated ability to accurately express the rheology of polymer solutions for a wide range of strain rates.

The primary aim of this work is to develop an efficient computational methodology that could be used to accurately simulate the flow of complex fluids governed

[1] The contents of this chapter are from Abuga and Chinyoka [44]

by the Rolie-Poly constitutive equation. The development of such a computational platform is crucially important for the purposes of our follow up studies on the computational analysis of shear banding phenomena by coupling polymer stress with inhomogeneous concentration profile. Our numerical algorithms will be based of a finite volume method (FVM) and will be implemented on the open source software package OpenFOAM®.

In this paper, we will present both validation results as well as new benchmark results from our FVM based OpenFOAM® numerical solver for flow of fluids governed by the Rolie-Poly constitutive model. We use two well-known benchmark problems, the lid-driven cavity flow and the 4:1 planar contraction flow problems. In order to stabilize the numerical algorithm at high Weissenberg numbers, we employ either of two stabilization techniques; the Discrete Elastic Viscous Stress Splitting (DEVSS) technique as well as the Log-Conformation Reformulation (LCR) methodology.

Validation of our results is done by comparing our (stabilized) numerical results, against data from existing literature. The numerical results obtained for the contraction flow using the LCR stabilization approach are in good agreement with the existing literature for a wider range of Weissenberg numbers. The DEVSS method shows a good agreement only for lower Weissenberg numbers. For the lid-driven cavity flow, good agreement with the existing literature is observed for low Weissenberg numbers using either of the two stabilization techniques.

2.2 INTRODUCTION

The recent studies by Cromer *et. al.* [7] demonstrate that flow-induced non-uniformities of concentration can trigger shear banding in shear flow of fluids governed by the Rolie-Poly constitutive model. In this work we develop and test a computational methodology that could be used to accurately simulate the flow of complex fluids governed by the Rolie-Poly constitutive equation. There are a number of benchmark flow problems that are often used as test cases when developing new numerical methods in computational rheology, primarily for validating the new numerical methodologies. Typical benchmark flows used include the lid-driven cavity flow, flows through axisymmetric and planar contractions and flows around cylinders or spheres. One advantage of the lid-driven cavity flow is that the geometry is simple and thus easily yields to numerical methodology. Notwithstanding its simple geometry, complex flow structures such as eddies and vortices can be visualized. Basically, a fluid is contained in a rectangular geometry whose top wall is translated horizontally at some specified velocity. Fluid motion is subsequently generated, similarly to wall driven shear flows. Discontinuity in the boundary conditions at the two top corners where the side walls meet the lid are inevitable, leading to the so called corner singularities [45]. In order to eliminate the effects of corner singularities, different techniques have been employed. One such technique involves incorporating a controlled amount of leakage at the upstream and downstream corners of the cavity as given in [46]. Another method involves regularizing the lid velocity. This is done by imposing a parabolic velocity distribution along the moving lid so as to have a vanishing velocity and velocity gradient at the two upper corners as given in the works of Poole *et. al.* [47], Habla *et. al.* [48] and Comminal *et. al.* [2] among others. For contraction flow benchmark problems, the focus is on predicting the formation, development and dynamics of the corner and lip vortices. The vortex lengths are then used in the comparison of numerical and/or experimental results. However, the numerical simulation of such flows of viscoelastic fluids present a huge challenge, in particular, the High Weissenberg Number Problem (HWNP). The HWNP is the breakdown of numerical schemes

beyond some critical value of the Deborah (or Weissenberg) number [40]. The Deborah number, determines the elastic character of the flow and is given as the ratio of the polymer relaxation time to the time scale of the flow. It has been observed that when the Deborah number exceeds some critical value, numerical methods for viscoelastic fluid flow computations break down. This critical value is dependent on the viscoelastic constitutive model, the flow type, the numerical method and mesh used. The HWNP is a result of steep exponential profiles which arise as due to the viscoelastic stresses experiencing a combination of deformation and convection. These exponential profiles are caused by the inappropriateness of polynomial based approximations that are used to represent the viscoelastic stress tensor. In particular, such polynomial based approximations are exponential in regions of high deformation rates, or near stagnation points [42]. The Discrete Elastic Viscous Stress Splitting (DEVSS) and LCR techniques are some of the methods, among many others, that have been developed to mitigate against the HWNP. The DEVSS method involves re-expressing the constitutive equation to include an explicit viscous stress and introducing the velocity gradient as an additional variable [49]. A variant of such method is the Elastic Viscous Stress Splitting (EVSS) technique [50]. Other methods aim to stabilise the advection terms in the constitutive equations. Such methods include, the up-winding techniques for convective equations, for example the Discontinuous Galerkin (DG) method [51] and the Streamline Upwind Petrov Galerkin (SUPG) method [52]. The LCR approach for numerical stabilization was recently proposed by Fattal and Kupferman [43]. This technique reformulates the constitutive law in terms of a matrix logarithm and improves the representation of large stress gradients by linearizing the stress profile. The LCR technique introduces a better polynomial interpolation via logarithmic variables and preserves the positive-definiteness of the conformation tensor. It is worth noting that the loss of the positive-definiteness of the stress tensor is a precursor to the HWNP. The LCR method has been implemented in various studies such as in the finite volume method (FVM) framework for creeping flows of viscoelastic fluids in steady and unsteady flows around a confined cylinder [53], the numerical simulation of viscoelastic flow in three-dimensional

lid-driven cavity flow in OpenFoam® [54] and in the robust simulations of viscoelastic flows at high Weissenberg numbers [2]. The LCR representation has also been used with the finite element method for simulating lid-driven cavity flow of Oldroyd-B fluids at high Weissenberg numbers [55]. A combination of the LCR and pure stream-function formulations was used in [56] for the two-dimensional flow of an Oldroyd-B fluid inside a lid-driven cavity simulated over a wide range of Weissenberg numbers while [57] employed a combination of LCR representation and an operator splitting lie scheme to simulate time-dependent cavity flow of an Oldroyd-B fluid using a regularized velocity to remove the discontinuities at the two upper corners. In this work, both the lid-driven cavity flow and 4:1 planar contraction flow will be used to benchmark the Rolie-Poly viscoelastic flow solver that we have developed. The solver is implemented on the open-source, OpenFoam® platform. Some of the advantages of using OpenFoam® are that, as an open source platform, it has no limiting aspects regarding licensing fees and that it has the ability to flexibly deal effectively with complex geometries. The OpenFoam® software is based on the finite volume method and has the ability of parallelization. OpenFoam® uses the C++ object oriented programming, making it convenient for users to incorporate their own models since existing solvers can be modified. For example, Favero *et. al.* [38] developed and incorporated a viscoelastic fluid flow solver into OpenFoam® which was later extended by Florian *et. al.* to handle two-phase flows of viscoelastic fluids. Silva and Lage [58] extended the two-phase flow solver to include a multi-phase flow formulation.

The purpose of the present work is to develop a viscoelastic flow solver for fluids governed by the Rolie-Poly constitutive model. The solver implements both the LCR Reformulation and DEVSS techniques. We assess the efficiency and accuracy of the solver by comparing the simulation results, for values of the material parameters corresponding to the widely studied Oldroyd-B fluid model, with those Oldroyd-B results in the existing literature. We then present benchmark simulation results and predictions obtained for the full Rolie-Poly constitutive model using the lid-driven cavity and 4:1 planar contraction benchmark flows.

2.3 METHODOLOGY

2.3.1 Governing equation

We consider the unsteady, incompressible, isothermal flow of a viscoelastic fluid. The governing equations for the flow include the mass conservation equation, the momentum equations and the constitutive equation for the viscoelastic stress $\boldsymbol{\tau}$. The equation of mass conservation reads,

$$\nabla \cdot \boldsymbol{u} = 0. \tag{2.1}$$

The momentum equations read,

$$\rho \left[\frac{\partial \boldsymbol{u}}{\partial t} + \nabla \cdot \boldsymbol{u}\boldsymbol{u} \right] = -\nabla p + \eta_s \nabla \cdot \nabla \boldsymbol{u} + \nabla \cdot \boldsymbol{\tau}. \tag{2.2}$$

We will use the Rolie-Poly constitutive equation of Likhtman and Graham [26] to model the dynamics of the viscoelastic stress $\boldsymbol{\tau}$. At present, the Rolie-Poly model remains the most advanced differential constitutive formulation of the Doi-Edwards tube models for linear entangled polymer melts and it includes the processes of reptation, convective and reptation-driven constraint release, chain stretch and contour length fluctuation. The Rolie-Poly constitutive equation may be written as,

$$\begin{aligned} \frac{\partial \boldsymbol{\tau}}{\partial t} + (\boldsymbol{u} \cdot \nabla)\boldsymbol{\tau} - (\nabla \boldsymbol{u})\boldsymbol{\tau} - \boldsymbol{\tau}(\nabla \boldsymbol{u})^{\dagger} = -\frac{1}{\lambda}(\boldsymbol{\tau} - \boldsymbol{I}) \\ - \frac{2(1 - \sqrt{3/\mathrm{tr}\,\boldsymbol{\tau}})}{\lambda_R} \left(\boldsymbol{\tau} + \beta^* \left(\frac{\mathrm{tr}\,\boldsymbol{\tau}}{3} \right) \boldsymbol{\tau} - \boldsymbol{I} \right), \end{aligned} \tag{2.3}$$

where λ is the reptation relaxation time, λ_R is the Rouse relaxation time, β^* is the convective-constraint release (CCR) parameter and often varies from 0 to 1. $\boldsymbol{I}$ is the identity tensor, $\dagger$ denotes the matrix transpose and tr denotes the trace. The parameter δ is obtained from experimental data and takes the value of -1/2. We note that when $\lambda_R \to \infty$ the Rolie-Poly model reduces to the Oldroyd-B model.

2.3.2 DEVSS approach

The DEVSS technique is used to improve the numerical stability by introducing an additional diffusion term on each side of the momentum equations [59]. The momentum equations (2.2) are then rewritten as,

$$\rho\left[\frac{\partial \boldsymbol{u}}{\partial t}+\nabla\cdot\boldsymbol{u}\boldsymbol{u}\right]-(\eta_s+k)\,\nabla\cdot(\nabla\boldsymbol{u})=-\nabla p+\nabla\cdot\boldsymbol{\tau}-\ k\nabla\cdot(\nabla\boldsymbol{u})\,, \tag{2.4}$$

where k is a positive number that is related to the parameters of the constitutive model and, according to Jovani [59], a good choice is $k = \eta_p$ where η_p is the polymer viscosity.

2.3.3 Log-Conformation Reformulation (LCR) approach

To improve the numerical stability, the log transformation known as the Log-Conformation Reformulation (LCR) approach is used. The approach consists in a change of variable for the polymeric extra stress which is related to the conformation tensor ($\mathbf{c}$) by the equation

$$\boldsymbol{\tau}=\frac{\eta_p}{\lambda}(\boldsymbol{c}-\boldsymbol{I}), \tag{2.5}$$

where λ is the relaxation time and η_p is the polymer viscosity. The viscoelastic constitutive equation can be written in terms of the conformation tensor as

$$\frac{\partial \boldsymbol{c}}{\partial t}+(\boldsymbol{u}\cdot\nabla)\boldsymbol{c}-(\boldsymbol{c}.\nabla\boldsymbol{u}^T+\nabla\boldsymbol{u}\cdot\boldsymbol{c})=-\frac{1}{\lambda}f_R(\boldsymbol{c}), \tag{2.6}$$

where $f_R(\boldsymbol{c})$ is the relaxation function which is a polynomial of the conformation tensor. The process outlined in this section is as suggested by Fattal and Kupferman [43]. Since the conformation tensor $\boldsymbol{c}$ is a positive-definite matrix, it can be diagonalized according to

$$\boldsymbol{c}=\boldsymbol{R}\cdot\Lambda\cdot\boldsymbol{R}^T, \tag{2.7}$$

where Λ is a diagonal matrix consisting of the eigenvalues of $\boldsymbol{c}$ and where the matrix $\boldsymbol{R}$ is orthogonal and contains the corresponding eigenvectors. Instead of solving the Equation 2.3, for the stress $\boldsymbol{\tau}$, this equation is reformulated in terms of the natural logarithm of the conformation tensor $\boldsymbol{c}$,

$$\boldsymbol{\Psi} = \log(\boldsymbol{c}) = \boldsymbol{R} \cdot \log(\Lambda) \cdot \boldsymbol{R}^T. \tag{2.8}$$

$\boldsymbol{\Psi}$ then becomes our new variable and the velocity gradient $\nabla \boldsymbol{U}$ is decomposed as

$$\nabla \boldsymbol{U} = \Omega + \boldsymbol{B} + \boldsymbol{N} \cdot \boldsymbol{c}^{-1}, \tag{2.9}$$

where Ω and $\boldsymbol{N}$, which both account for rotations are anti-symmetric tensors. $\boldsymbol{B}$ is a diagonal tensor which accounts for pure extensions. Substituting Equation 2.8 and velocity gradient decomposition 2.9 into Equation 2.6 yields the log-conformation equation,

$$\frac{\partial \boldsymbol{\Psi}}{\partial t} + (\boldsymbol{u} \cdot \nabla)\boldsymbol{\Psi} - (\Omega\boldsymbol{\Psi} - \boldsymbol{\Psi}\Omega) - 2\boldsymbol{B} = -\frac{1}{\lambda} \exp(-\boldsymbol{\Psi}) f_R \left[\exp(\boldsymbol{\Psi})\right], \tag{2.10}$$

where $\boldsymbol{B}$ and Ω are pure extension (symmetric, traceless) and pure rotation (anti-symmetric) matrices respectively that are obtained from the projection of the velocity gradient into the base of the stress tensor. The eigen decomposition of the conformation tensor in a two-dimensional flow is given as

$$\boldsymbol{c} = \boldsymbol{R} \begin{bmatrix} \lambda_1 & 0 \\ 0 & \lambda_2 \end{bmatrix} \boldsymbol{R}^T, \tag{2.11}$$

where λ_1 and λ_2 are the eigenvalues and $\mathbf{R}$ the orthogonal matrix containing the eigenvectors. The change of the base of velocity gradient is given as

$$\boldsymbol{R}^T (\nabla \boldsymbol{U}) \boldsymbol{R} = \begin{bmatrix} m_{11} & m_{12} \\ m_{21} & m_{22} \end{bmatrix}. \tag{2.12}$$

The pure extension and rotation matrices are obtained as,

$$\boldsymbol{B} = \boldsymbol{R} \begin{bmatrix} m_{11} & 0 \\ 0 & m_{22} \end{bmatrix} \boldsymbol{R}^T, \qquad \Omega = \boldsymbol{R} \begin{bmatrix} 0 & \zeta \\ -\zeta & 0 \end{bmatrix} \boldsymbol{R}^T, \tag{2.13}$$

where $\zeta = (m_{12} + m_{21})/(\lambda_2 - \lambda_1)$. For the first time step, Ω is set to be zero and $\boldsymbol{B} = 1/2\left[\nabla \boldsymbol{U} + (\nabla \boldsymbol{U})^T\right]$, since $\boldsymbol{c} = \boldsymbol{I}$ leads to $\lambda_2 = \lambda_1$ would result in an undefined division by zero.

The conformation tensor $\boldsymbol{c}$ is recovered from the matrix exponential of $\boldsymbol{\Psi}$, once Equation 2.10 has been solved. To verify the positive-definiteness of the conformation tensor $\det(\boldsymbol{c})$ must be greater than zero.

2.3.4 Solution algorithm and numerical method

We employ the finite volume method implemented on the open source software package OpenFoam®. The algorithm used to calculate the pressure field is the semi-implicit method for the pressure linked equation consistent (SIMPLEC) which is a modification of the SIMPLE algorithm since the SIMPLEC algorithm has been proved to have better convergence properties than the SIMPLE algorithm [60, 61]. The Convergent and Universally Bounded Interpolation Scheme for the Treatment of Advection (Cubista) scheme, a high resolution scheme with improved iterative convergence properties, is used to discretize the convective terms and temporal derivatives appearing in the momentum and transport equations. The Cubista scheme was devised by incorporating total-variation diminishing constraints, appropriate for unsteady problems, into an implicit time-marching method used for steady flow problems [62].

The computational steps followed by the solver are:

1. Initialize the variables;

2. For the LCR approach, solve for $\boldsymbol{\Psi}$ via Eq. (2.10), or alternatively;

2. For the DEVSS approach, Solve for $\boldsymbol{\tau}$ via Eq. (2.3);

3. Solve appropriate momentum equations;

4. Solve pressure equation;

5. Correct both pressure and velocity;

6. Advance in time, $t = t + \delta t$, and return to step 2 until the predetermined final time (or alternative terminating condition) is reached.

The solver for the stress constitutive equations as well as for the momentum equations is the bi-conjugate gradient stabilized (BiCGstab) solver with a Cholesky preconditioner. A preconditioned conjugate gradient (PCG) solver is used to solve the pressure equation in conjunction with a simplified diagonal-based incomplete LU (DILU) preconditioner.

2.4 LID-DRIVEN CAVITY FLOW

2.4.1 Geometry and boundary conditions

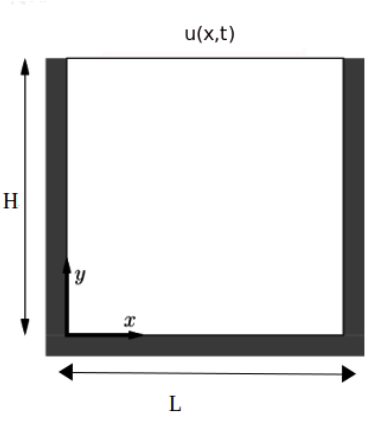

FIGURE 2.1: Geometry of the lid driven cavity

For the lid-driven cavity flow, see Fig. 1, a square cavity is used with the upper lid moving with a regularized velocity. The flow is assumed to be two dimensional

(2D), being limited to the xy-plane. No-slip boundary and impermeability conditions are ascribed to the velocity at the walls. Zero normal gradient boundary conditions are assigned for pressure, p. The polymeric extra stresses are linearly extrapolated at the walls. A time-space dependent condition is imposed for the lid-velocity so as to impose a smooth start of the flow. This form of regularization has the effect of avoiding local singularities at the top-right and top-left corners as it ensures both the velocity and velocity gradient vanish at the corners. The polynomial function used for the lid velocity is as in [42];

$$u(x,t) = 8[1 + tanh\,\{8(t-0.5)\}]x^2(1-x)^2. \tag{2.14}$$

2.4.2 Numerical validation

The analysis of the flow behaviour is based on simulating the regularized lid-driven cavity for Deborah numbers 3 and below as is done in the comparative, benchmarking literature. The Deborah number, De, is defined in terms of the polymer relaxation time, λ, characteristic fluid velocity, u, and a characteristic length scale, L, as

$$De = \frac{\lambda u}{L}.$$

For validation purposes of our Rolie-Poly solver, we take advantage of the fact that the Rolie-Poly model reduces to the Oldroyd-B model when $\lambda_R \to \infty$ as well as the fact that benchmark Oldroyd-B results widely exist in the literature. We therefore validate our solver by recovering the Oldroyd-B results from our Rolie-Poly solver and comparing these with existing literature on Oldroyd-B lid-driven cavity, say [56]. The maximum lid velocity is set to $u = 1$. A retardation ratio β of $1/2$ is used and the Reynolds number is set to negligible value of $Re = \rho u L/\eta_0 = 5 \times 10^{-4}$ which is considered as creeping flow. The velocity components and the components of the log-conformation tensor are obtained. The three components of the tensor, the velocity and log-conformation profiles along vertical line $x = 1/2$ and along

horizontal line $y = 3/4$ including the history of the specific Kinetic energy E_k are plotted, see Figures 2.2 - 2.13.

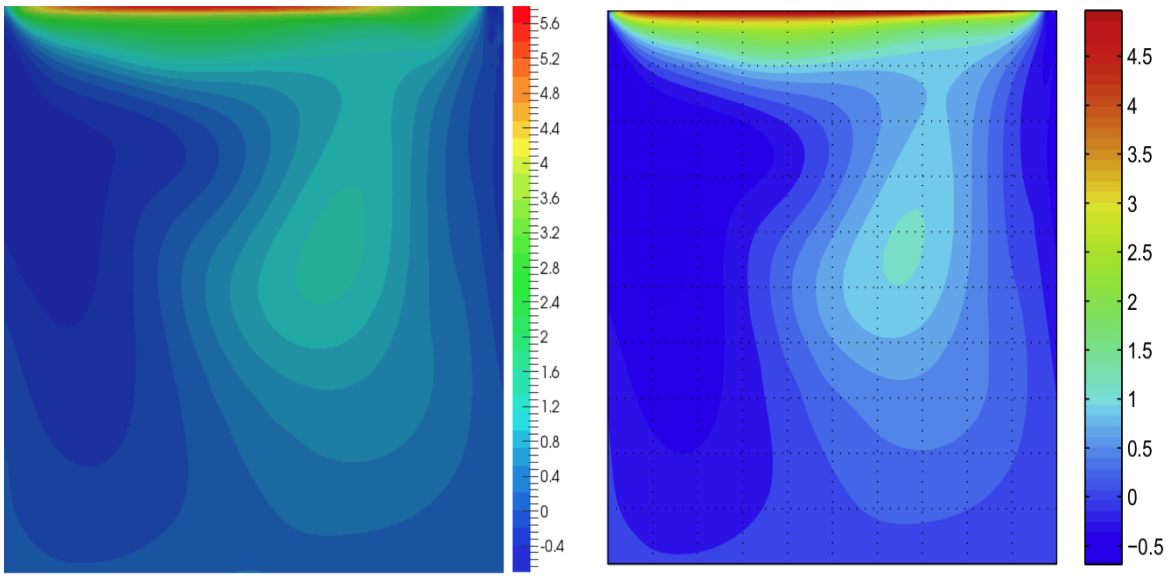

(a) (b)

FIGURE 2.2: Comparison of the component of the log-conformation tensor Log-Conf.Ψ_{11} from our simulations (a) and from Comminal *et. al.* [2] (b) at time $t = 8$ for $De = 1$.

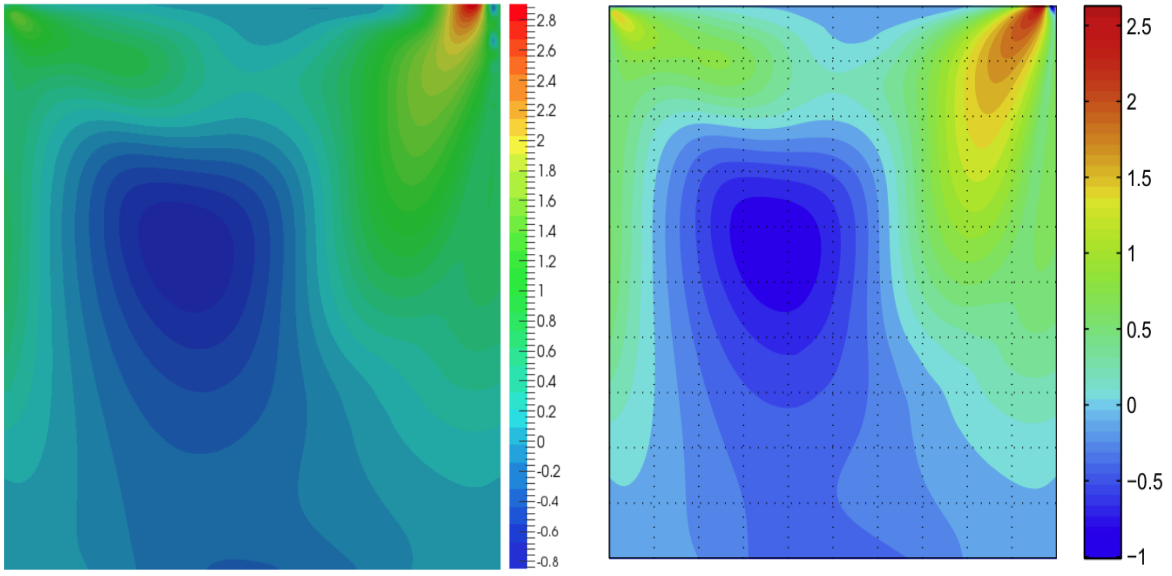

(a) (b)

FIGURE 2.3: Comparison of the component of the log-conformation tensor Log-Conf.Ψ_{12} from our simulations (a) and from Comminal *et. al.* [2] (b) at time $t = 8$ for $De = 1$.

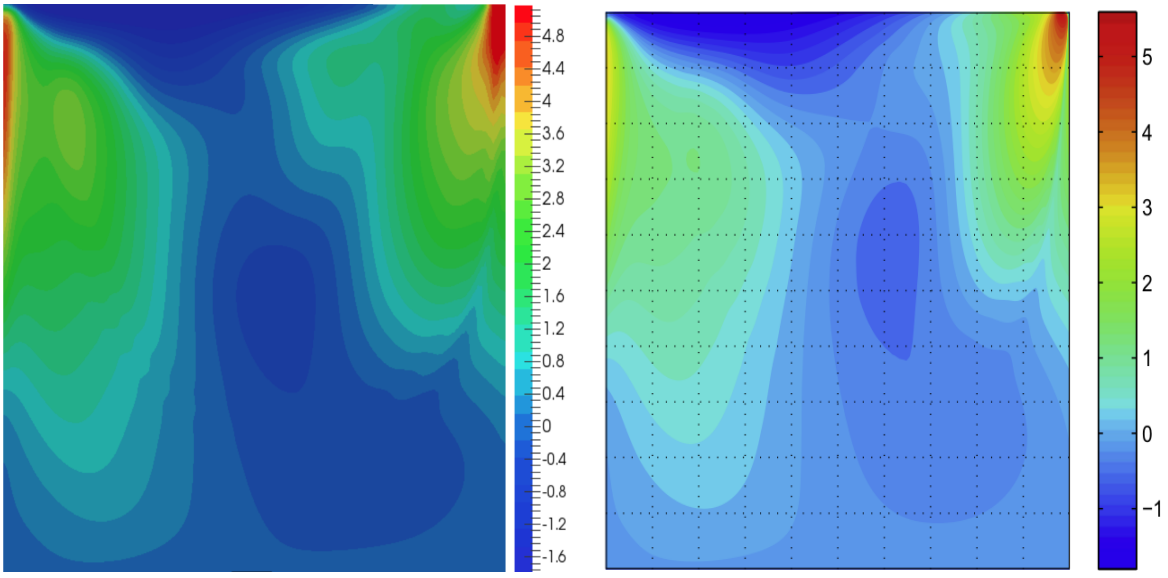

(a) (b)

FIGURE 2.4: Comparison of the component of the log-conformation tensor Log-Conf.Ψ_{22} from our simulations (a) and from Comminal *et. al.* [2] (b) at time $t = 8$ for $De = 1$.

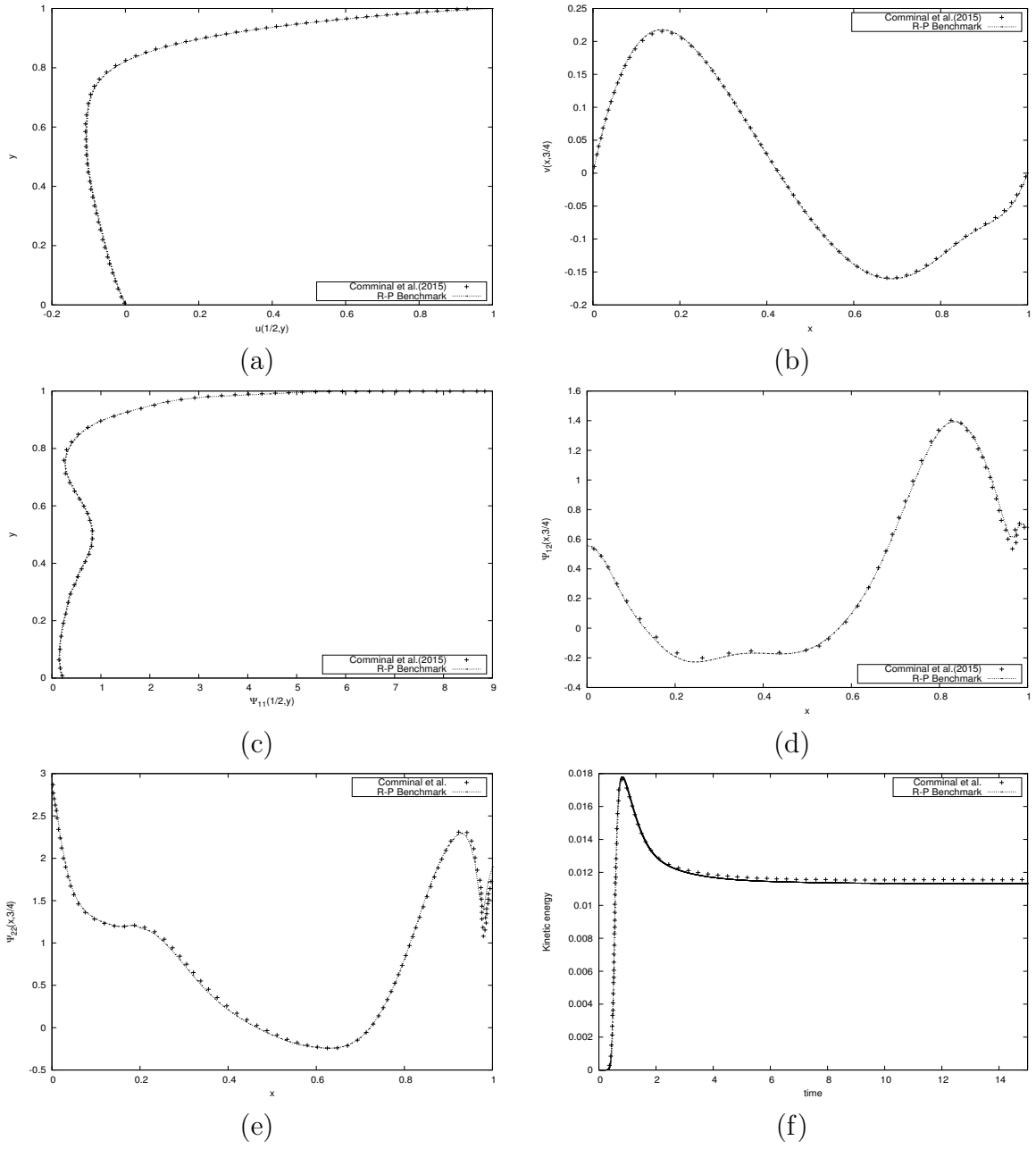

FIGURE 2.5: Results for LCR at time $t = 8$, for $De = 1$: velocity and stress profiles along the lines $x = 1/2$ and $y = 3/4$ (compared with references [2]) and history of the Kinetic Energy

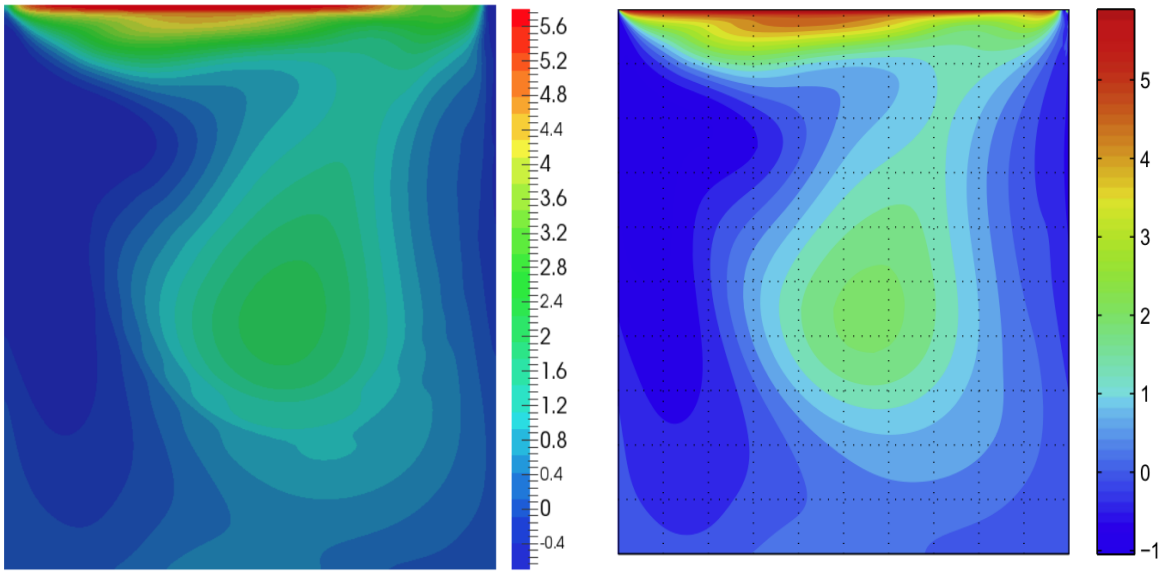

(a) (b)

FIGURE 2.6: Comparison of the component of the log-conformation tensor Log-Conf.Ψ_{11} from our simulations (a) and from Comminal *et. al.* [2] (b) at time $t = 40$ for $De = 2$.

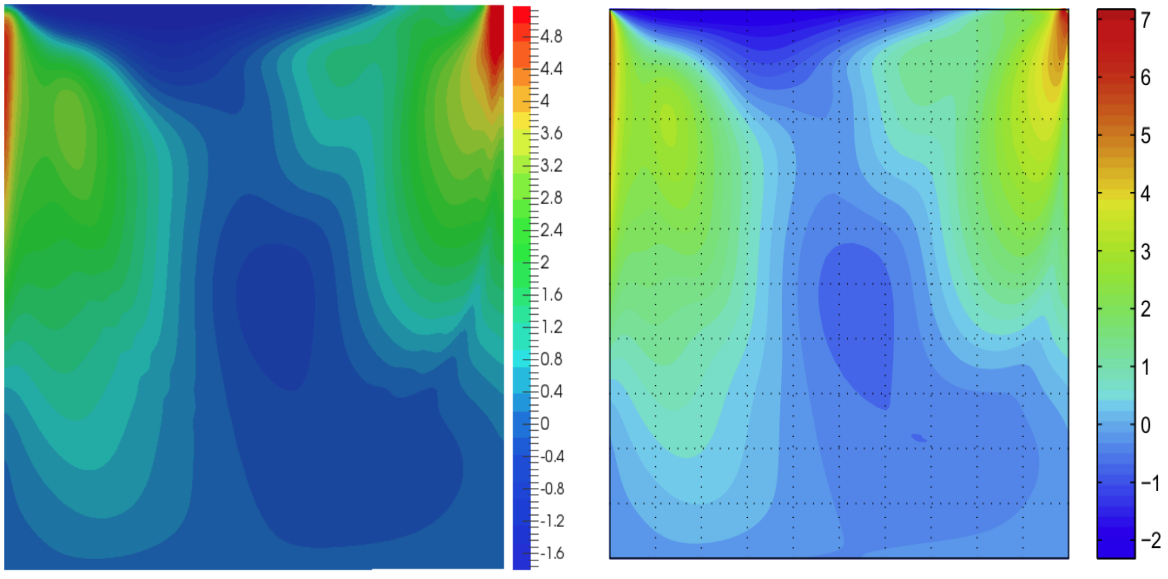

(a) (b)

FIGURE 2.7: Comparison of the component of the log-conformation tensor Log-Conf.Ψ_{12} from our simulations (a) and from Comminal *et. al.* [2] (b) at time $t = 40$ for $De = 2$.

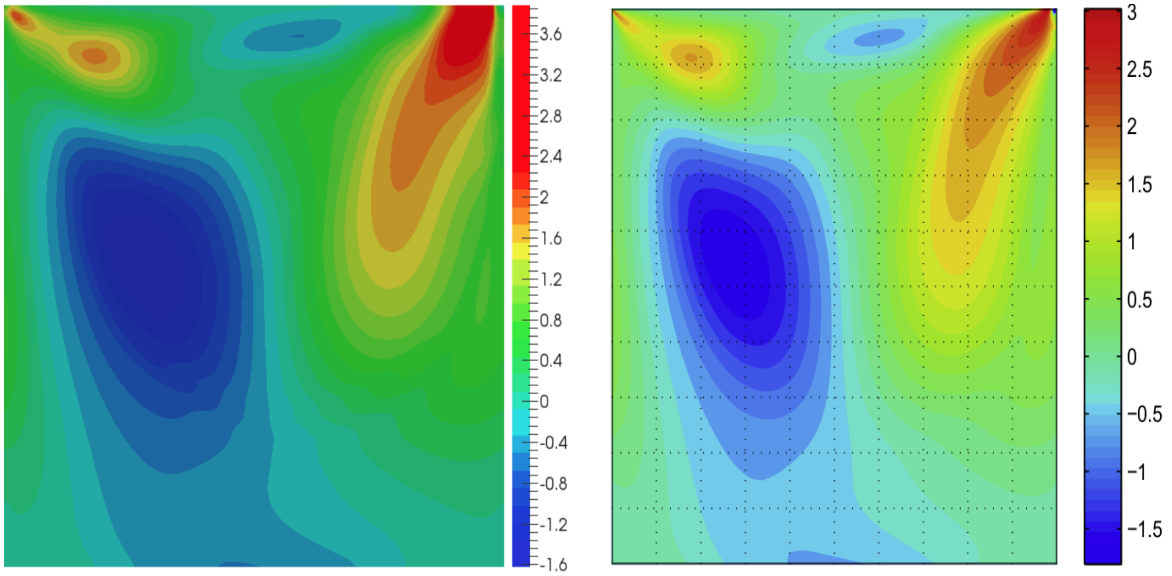

(a) (b)

FIGURE 2.8: Comparison of the component of the log-conformation tensor Log-Conf.Ψ_{22} from our simulations (a) and from Comminal *et. al.* [2] (b) at time $t = 40$ for $De = 2$.

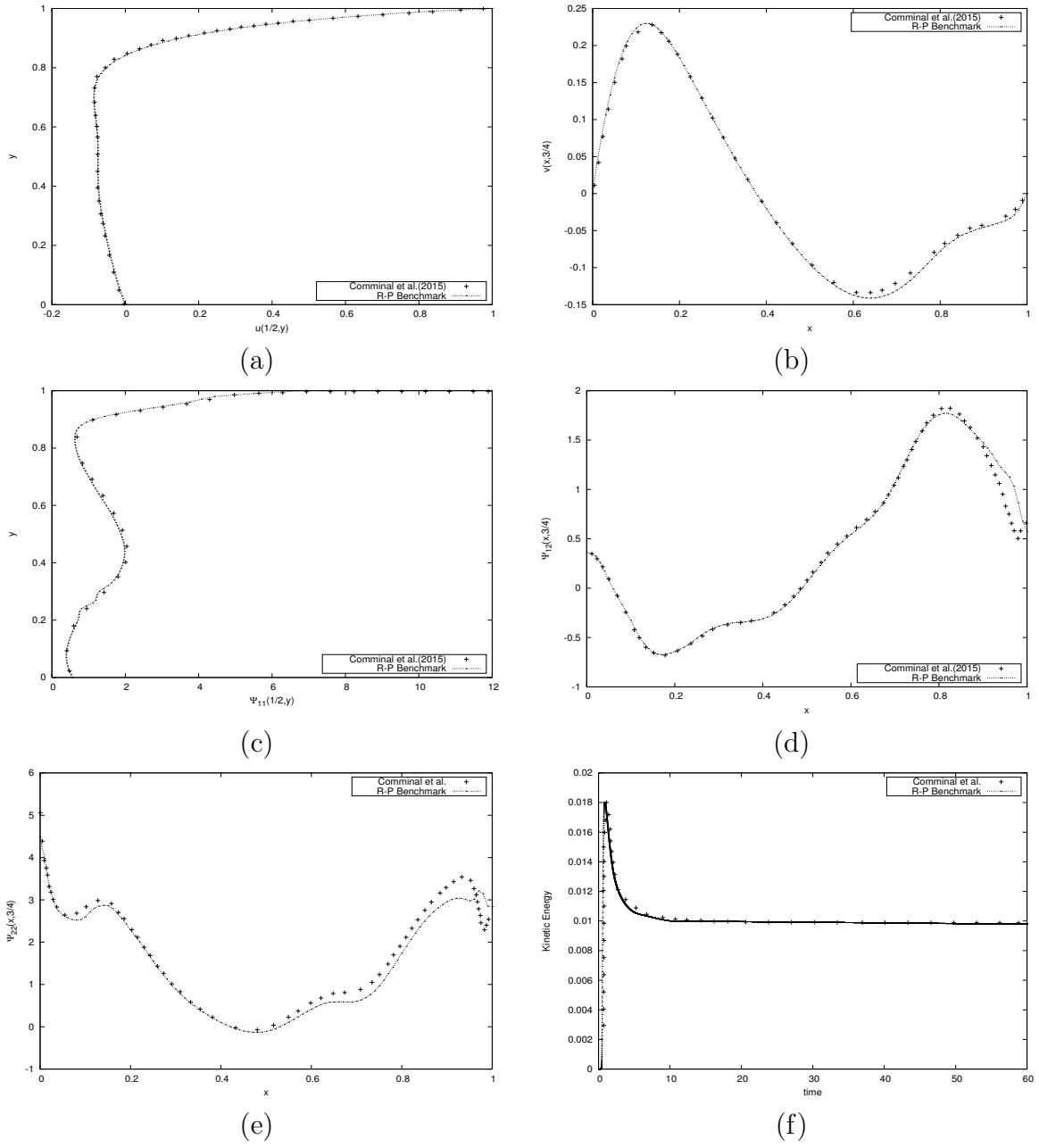

FIGURE 2.9: Results for LCR at time $t = 40$, for $De = 2$: velocity and stress profiles along the lines $x = 1/2$ and $y = 3/4$ (compared with references [2]) and history of the kinetic energy

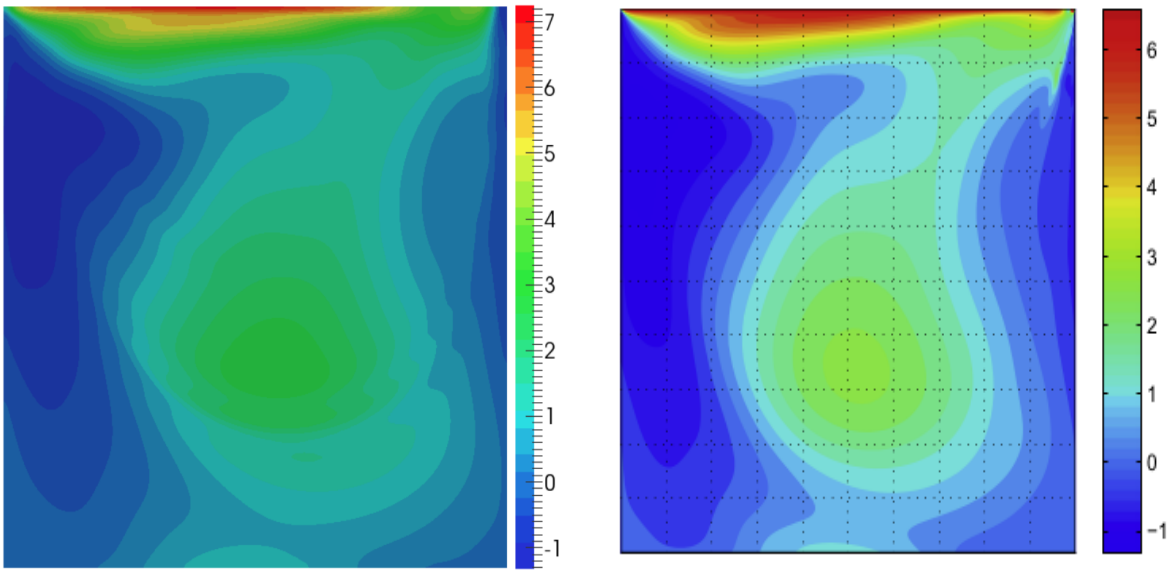

(a) (b)

FIGURE 2.10: Comparison of the component of the log-conformation tensor Log-Conf.Ψ_{11} from our simulations (a) and from Comminal *et. al.* [2] (b) at time $t = 40$ for $De = 3$.

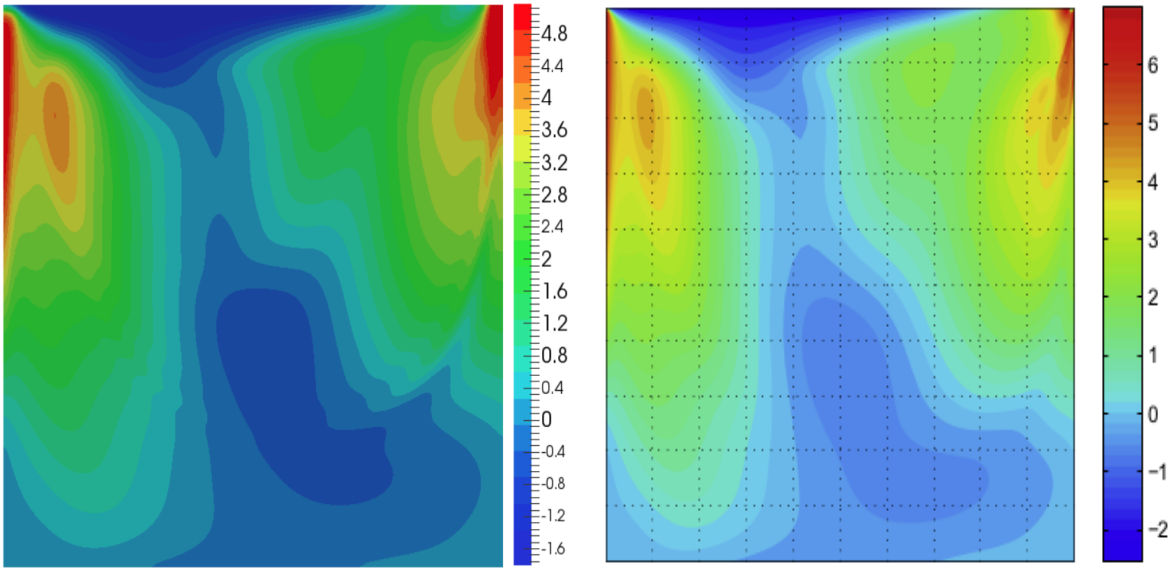

(a) (b)

FIGURE 2.11: Comparison of the component of the log-conformation tensor Log-Conf.Ψ_{12} from our simulations (a) and from Comminal *et. al.* [2] (b) at time $t = 40$ for $De = 3$.

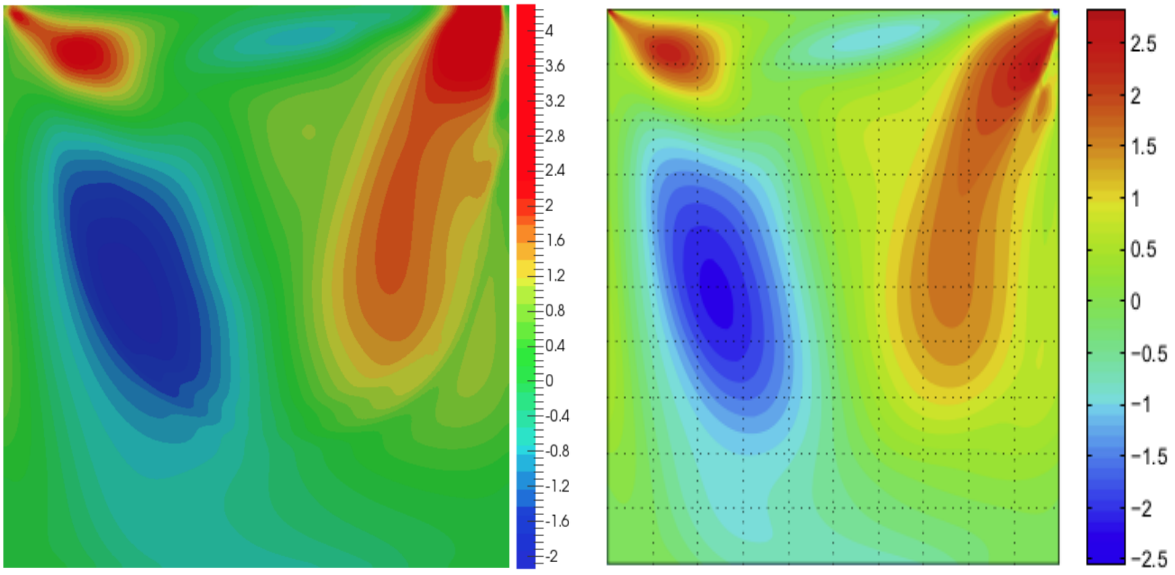

(a) (b)

FIGURE 2.12: Comparison of the component of the log-conformation tensor Log-Conf.Ψ_{22} from our simulations (a) and from Comminal *et. al.* [2] (b) at time $t = 40$ for $De = 3$.

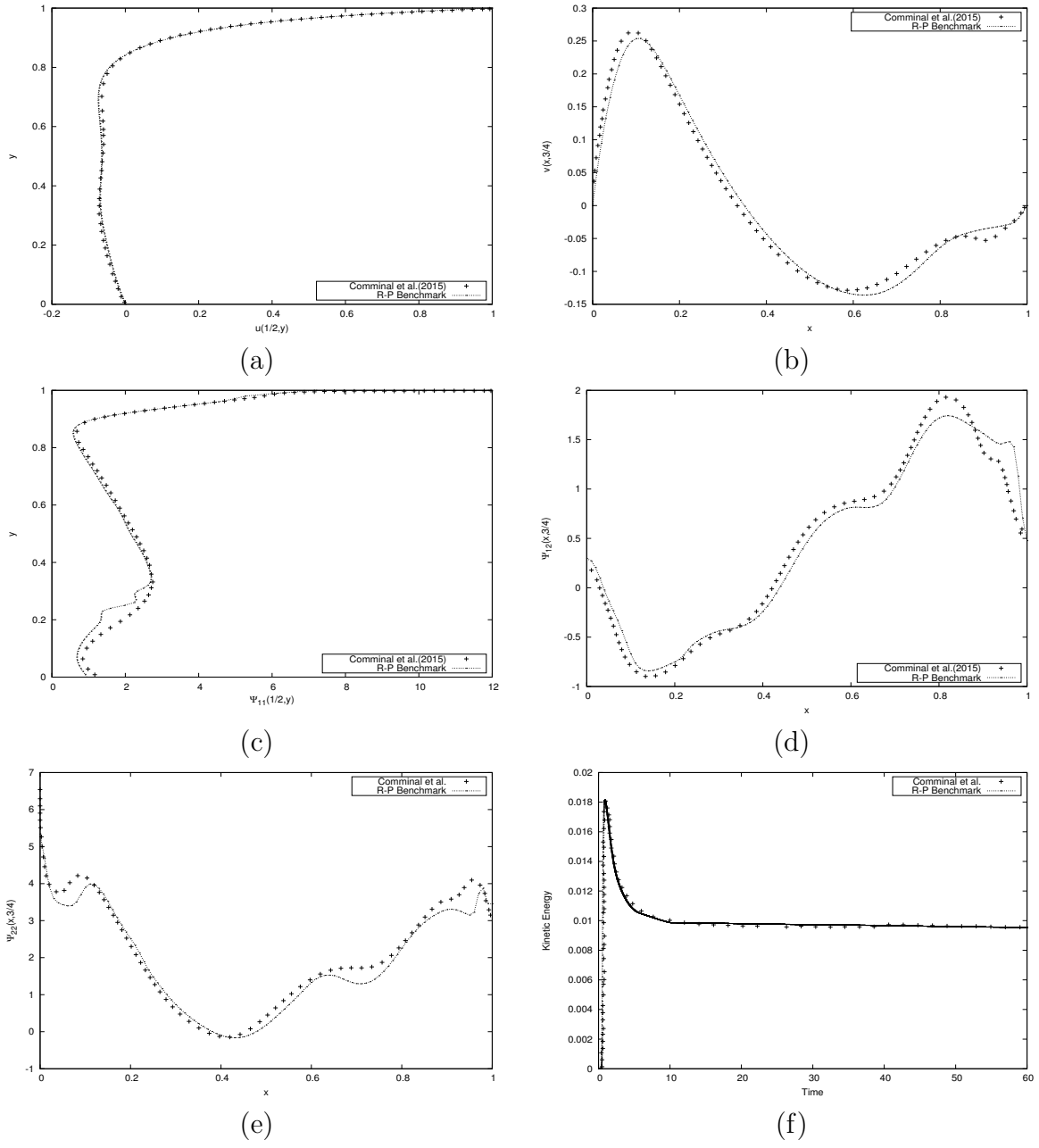

FIGURE 2.13: Results for LCR at time $t = 40$, for $De = 3$: velocity and stress profiles along the lines $x = 1/2$ and $y = 3/4$ (compared with references [2]) and history of the kinetic energy

To validate the DEVSS method, we only use the velocity profile along lines $x = 1/2$ and $y = 3/4$ and history of specific kinetic energy since there are no log-conformation tensors. The results are plotted in Figures 2.14 - 2.16.

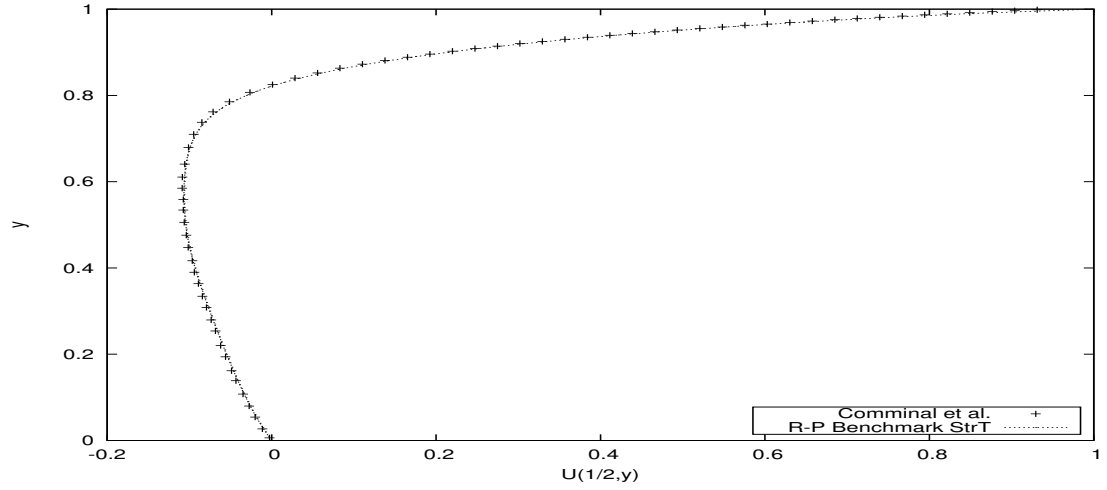

(a)

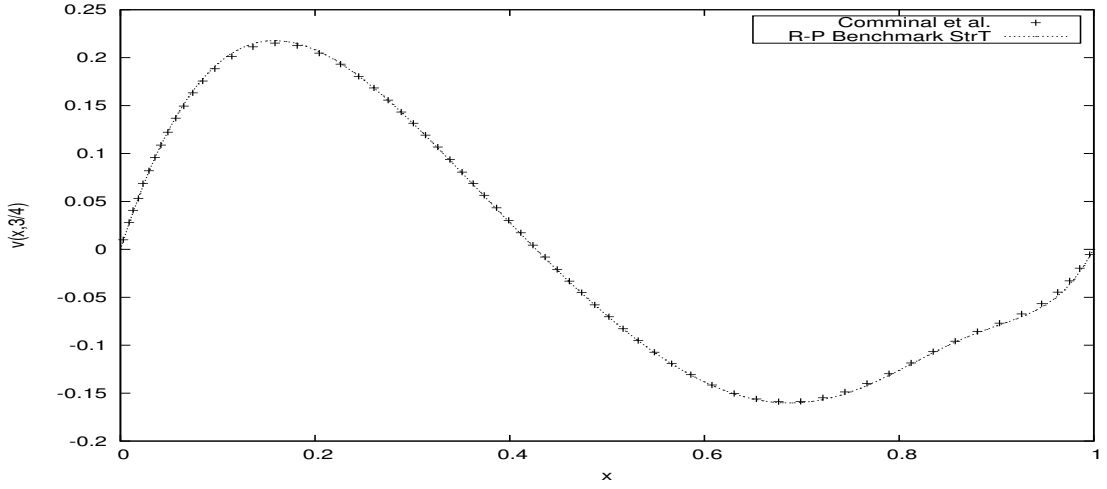

(b)

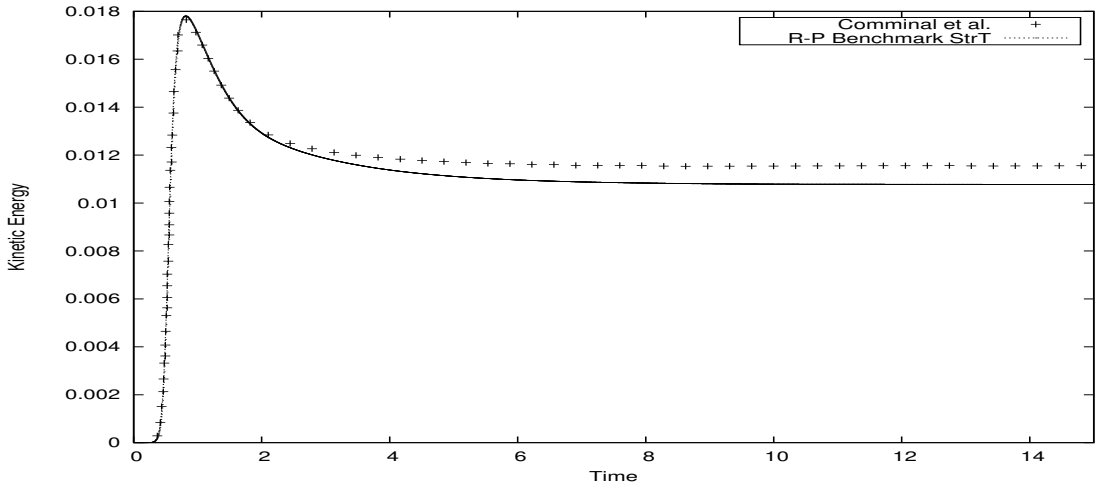

(c)

FIGURE 2.14: Results via the DEVSS approach at time $t = 40$ for $De = 1$ as compared with references [2]. velocity profiles along the lines $x = 1/2$ (a); velocity profiles along the lines $y = 3/4$ (b); history of the kinetic energy (c).

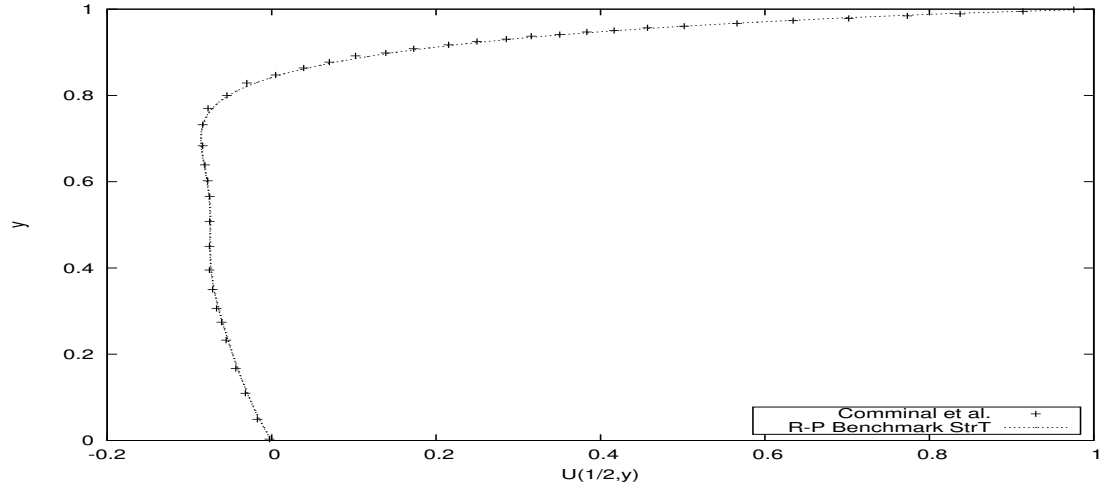

(a)

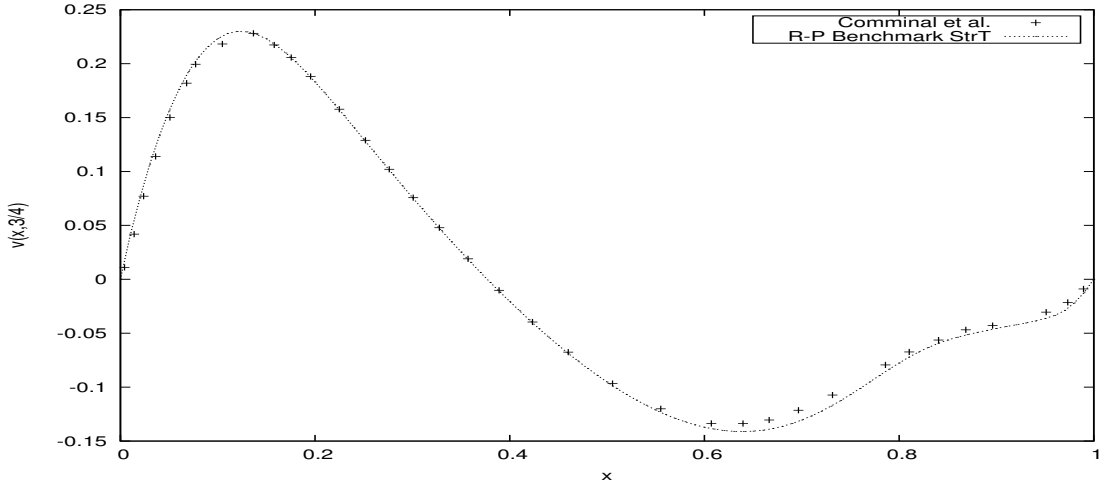

(b)

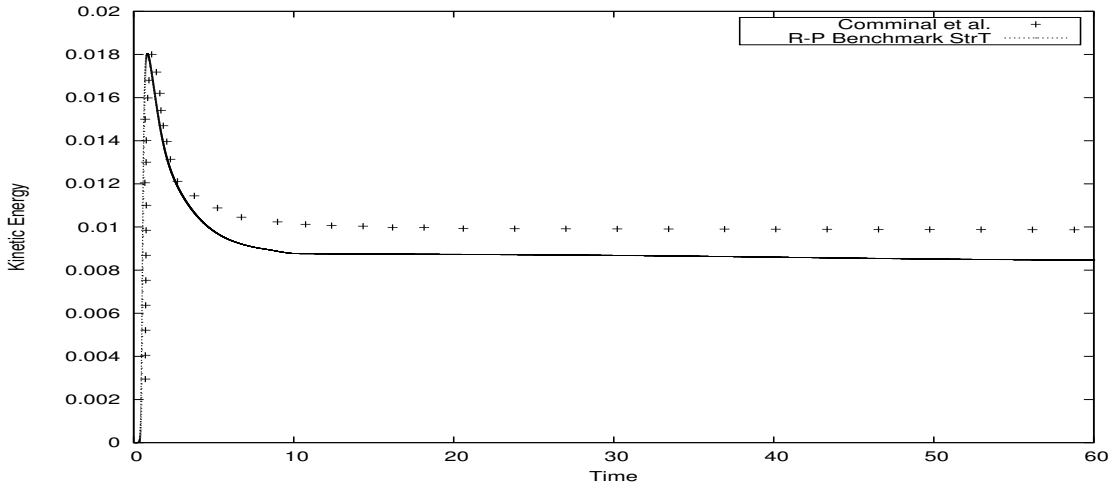

(c)

FIGURE 2.15: Results via the DEVSS approach at time $t = 40$ for $De = 2$ as compared with references [2]. velocity profiles along the lines $x = 1/2$ (a); velocity profiles along the lines $y = 3/4$ (b); history of the kinetic energy (c).

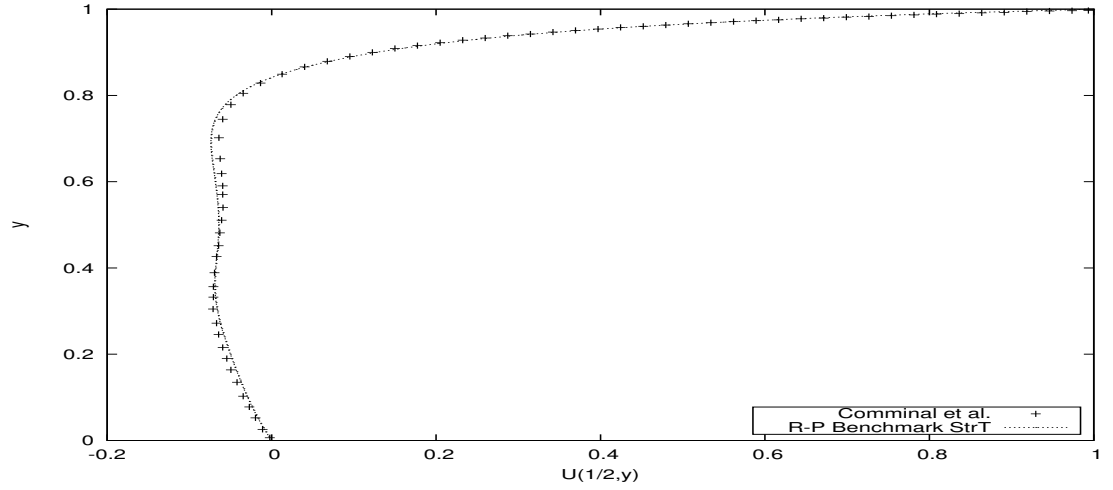

(a)

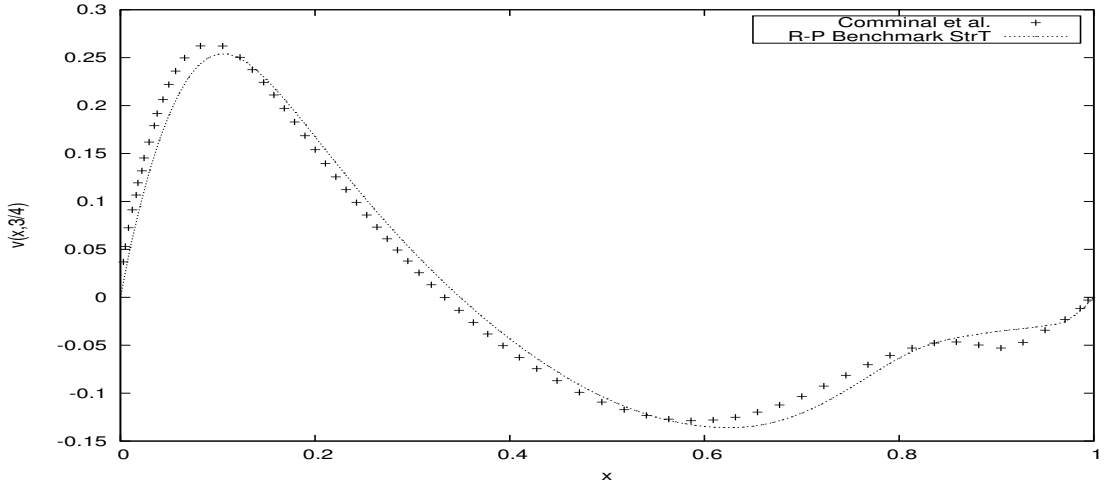

(b)

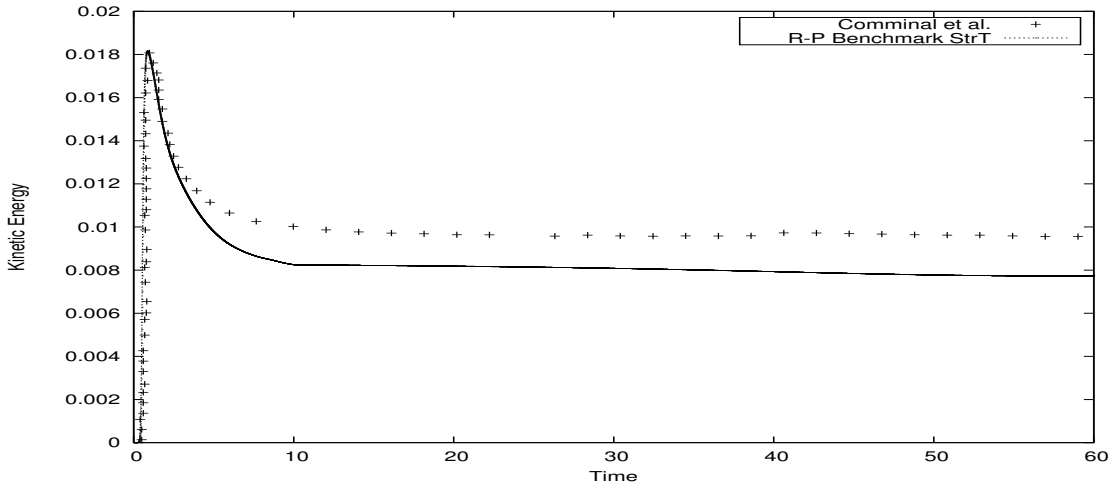

(c)

FIGURE 2.16: Results via the DEVSS approach at time $t = 40$ for $De = 3$ as compared with references [2]. velocity profiles along the lines $x = 1/2$ (a); velocity profiles along the lines $y = 3/4$ (b); history of the kinetic energy (c).

The predicted velocity and stress profiles and history of kinetic energy together with the results from literature are plotted in Figures 2.14 - 2.16. Quantitative results for the log-conformation tensors for Deborah number 1 as shown in Figures 2.2, 2.3 and 2.4 and for Deborah number 2 as shown in Figures 2.6, 2.7 and 2.8 show good agreement with the existing literature. This is supported by the velocity profiles, stress profiles and history of kinetic energy shown in Figs. 2.5 and 2.9 for $De = 1$ and $De = 2$ respectively.

Figures 2.10, 2.11 and 2.12 show that for Deborah number 3, there are slight differences in the stress profiles which can also be seen from the stress profiles 2.13. However, there is some degree of convergence (with the existing literature) in the velocity profiles and history of the kinetic energy.

The simulated results using the DEVSS method are presented in Figures 2.14, 2.15 and 2.16. The results shown in Figs. 2.14 and 2.15 show convergence in the velocity profiles for Deborah numbers 1 and 2 with slight differences in the history of the kinetic energy. However, Deborah number 3 has slight differences even in the velocity profiles as shown in Figure 2.16. Following satisfactory agreement between the simulation results and results from Comminal [2] for this geometry, we then proceed to present our solver's predicted lid-driven cavity results for the full Rolie-Poly constitutive model.

2.4.3 Lid-driven cavity results for the full Rolie-Poly model

In this section we present the results for the numerical simulation for the lid-driven cavity flow for the full Rolie-Poly constitutive model with $0 < \lambda_R < \infty$. As in the previous sections, we will also make comparisons between the DEVSS and the LCR stabilization methods. The velocity components and the components of the log-conformation tensor are computed and plotted. The components of the tensor, the velocity and log-conformation profiles along vertical line $x = 1/2$ and along horizontal line $y = 3/4$ are presented in Figure 2.17.

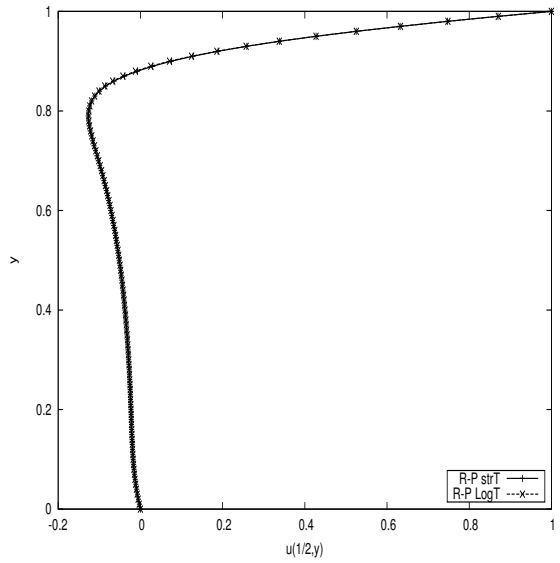
R-P strT
R-P LogT
y
u(1/2,y)

(a)

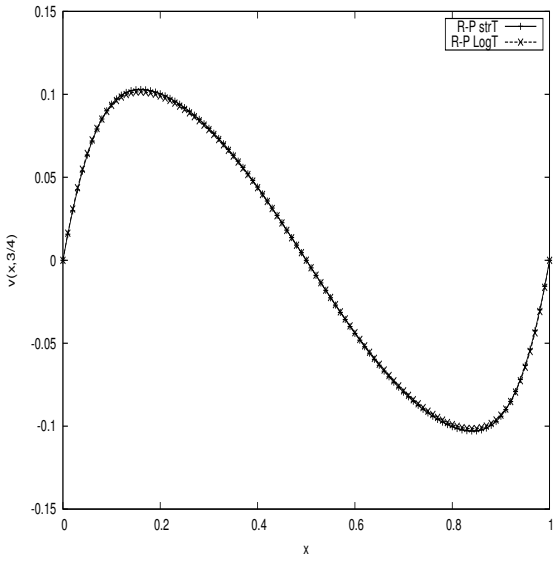
R-P strT
R-P LogT
v(x,3/4)
x

(b)

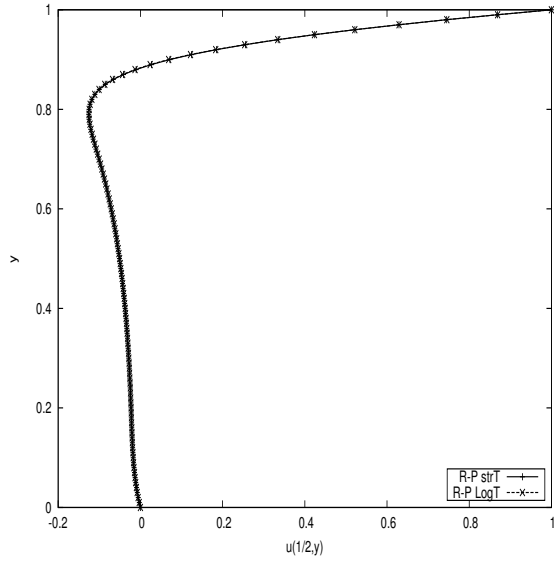
R-P strT
R-P LogT
y
u(1/2,y)

(c)

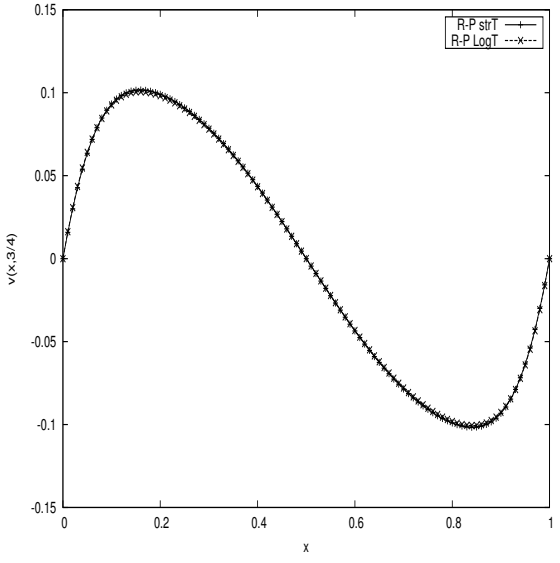
R-P strT
R-P LogT
v(x,3/4)
x

(d)

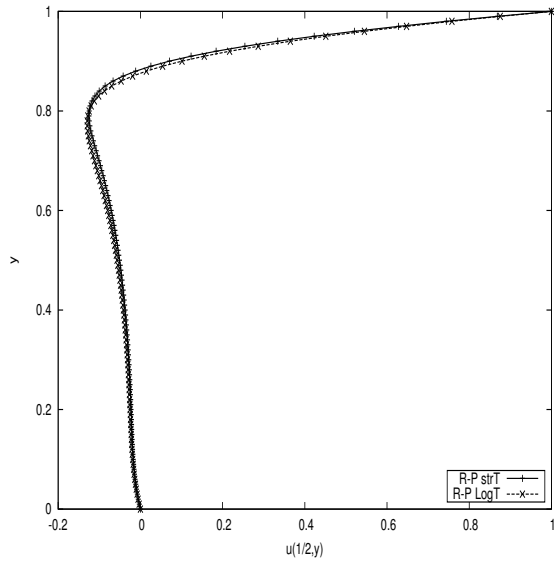

(e)

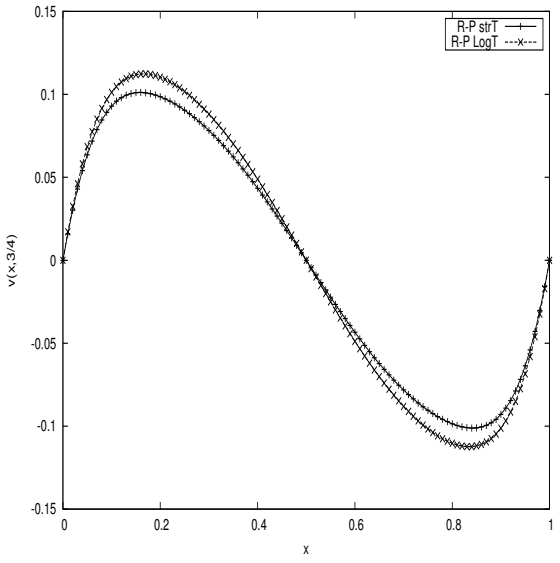

(f)

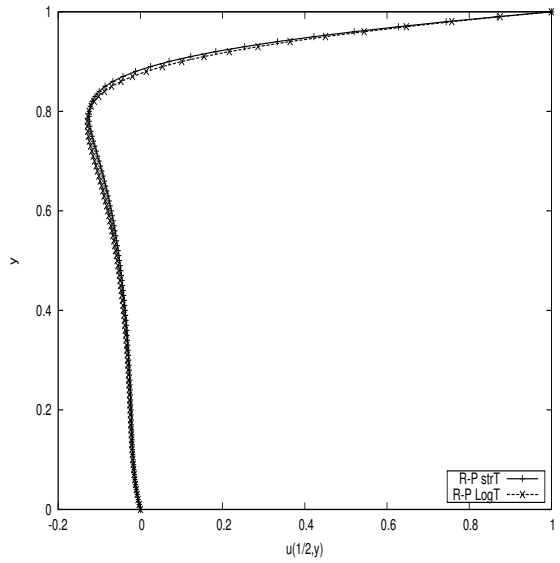

(g)

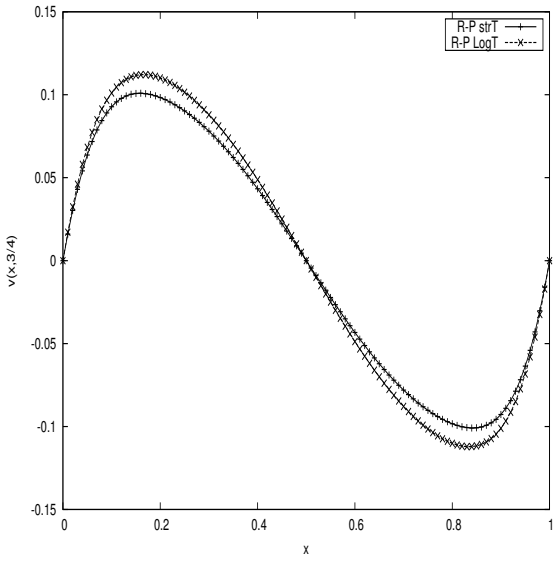

(h)

Figure 2.17 shows no apparent difference between the LCR method and the DEVSS results for Deborah numbers 1 and 2. There is a slight difference in the velocity profiles from Deborah numbers 3. Due to the better convergence of the LCR method to existing literature as demonstrated in previous section, we expect the LCR results to be the more accurate ones.

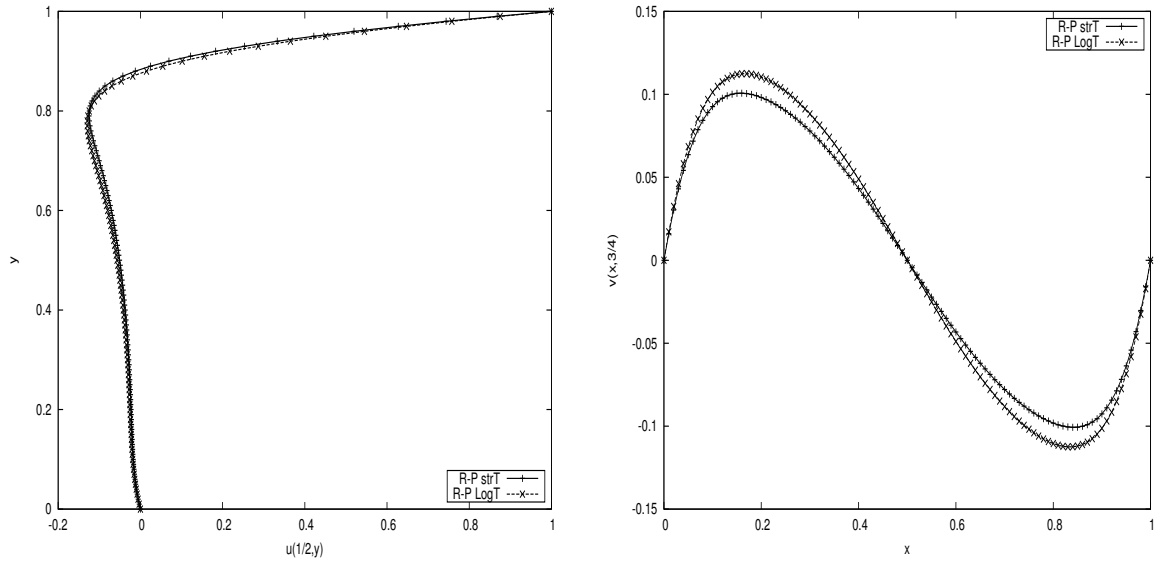

(i) (j)

FIGURE 2.17: Simulation results for Rolie-Poly constitutive equation for velocity profiles along the lines $x = 1/2$ and $y = 3/4$ comparing LCR (R-P LogT) and DEVSS (R-P StrT) at time $t = 10$, for $De = 1, 2, 3, 4$ and 5 respectively.

2.4.4 Vortex formation and growth

The flow of viscoelastic fluids in lid driven cavity flow geometries, such as the one under investigation, usually leads to the formation of corner vortices. We conclude this section by presenting the stream- lines diagrams for the flow of Rolie-Poly fluids in the lid driven cavity geometry for the purposes of investigating the formation (and growth) of corner vortices. Figures 2.18 (a)-(d), show the formation and growth of the corner vortices for various values of the Deborah number and also for both the LCR and DEVSS stabilization methodologies. We observe no discernible difference in the size of the corner vortices with an increase in the Deborah number.

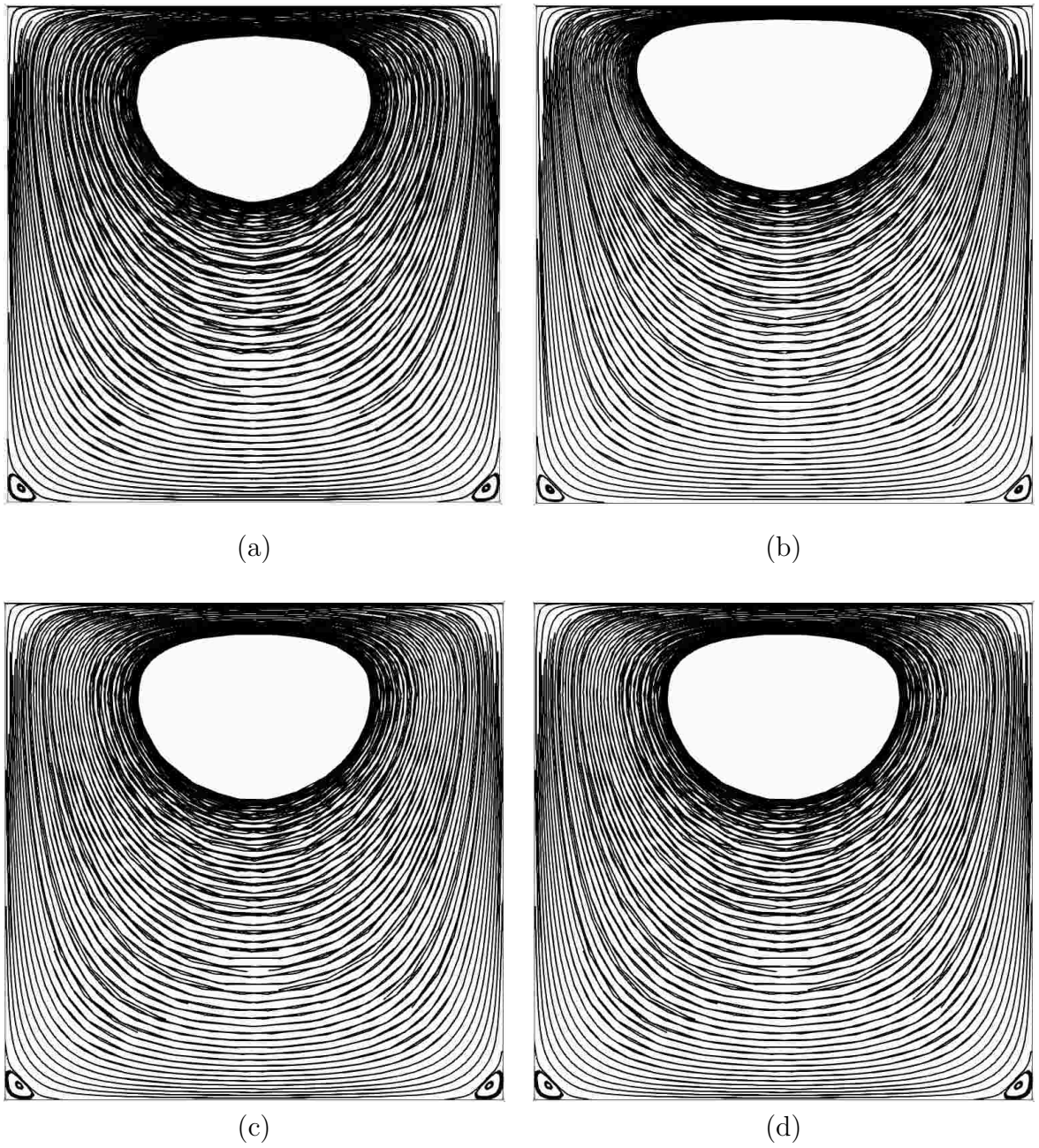

(a) (b)

(c) (d)

FIGURE 2.18: Streamline patterns in for the lid-driven cavity flow using for $De = 1$ and 3 respectively for LCR(LogT) simulations (RHS) and DEVSS (StrT) simulations (LHS).

2.5 4:1 PLANAR CONTRACTION FLOW

2.5.0.1 Geometry and Boundary conditions

For 4:1 planar contraction flow, two different dimensions were used, one for validation and the other for comparison of the DEVSS and LCR methods. For validation

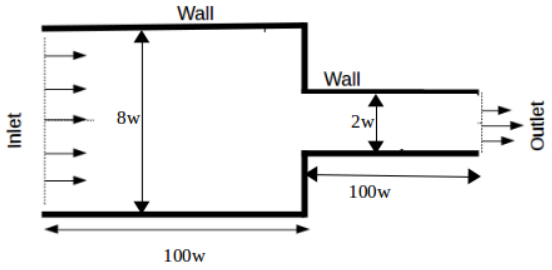

FIGURE 2.19: Geometry of 4:1 planar contraction

purposes, the downstream channel has a width of $2w$ and the upstream channel has a width $4w$ with both channels having an upstream and downstream length of $100w$ as is shown schematically in Figure 2.19. These dimensions were chosen in line with the existing validating literature.

For comparison between the LCR and DEVSS, the geometry similar to the one used for validation and has an upstream thickness of $2H = 0.0256m$ and downstream thickness of $2h = 0.0064m$ with an upstream length of $80h$ and a downstream length of $50h$.

To differentiate between the geometries, we will refer to the former geometry as planar 1 and the later as planar 2.

At the inlet, a uniform velocity profile is enforced. No-slip boundary conditions are enforced at the walls. Due to the long downstream channel, we assume that the velocity profile is fully developed and hence that the inflow and outflow conditions don't affect the flow in the contraction region.

For pressure, a zero-gradient condition is imposed at the inlet and normal to the wall. At the outlet, pressure is assigned a fixed value of zero. The stress is assigned a fixed value at the inlet and a zero-gradient condition at the outlet. As in similar 2D computation studies of viscoelastic fluid dynamics, say [63, 64, 65] the stresses will be linearly extrapolated at the walls.

2.5.0.2 Mesh convergence

Three different hexahedral meshes were used to analyse the mesh convergence. The characteristics of the three meshes are listed in Table 2.1 for Planar 1 and Table 2.2 for Planar 2. All the meshes used are such that there is a higher refinement near the walls and in the vicinity of the contraction since these regions are known to possess the largest velocity and stress gradients.

TABLE 2.1: Details of meshes used in Planar 1.

Mesh	$\Delta x_{\min}/h$	$\Delta y_{\min}/h$	Number of Control Volumes
M1	0.0042	0.0042	11991
M2	0.0029	0.0029	22287
M3	0.0020	0.0020	43491

TABLE 2.2: Details of the meshes used for Planar 2

Mesh	$\Delta x_{\min}/h$	$\Delta y_{\min}/h$	Number of Control Volumes
M1	0.0098	0.026	9200
M2	0.0065	0.017	20700
M3	0.0049	0.013	36800

Our simulated results for the velocity profile and stress profile τ_{xx} for the full Rolie-Poly constitutive model obtained via the LCR approach and using the three meshes are compared in Figure 2.20. The greatest differences are observed in the vicinity the contraction region. The differences are more significant for the stress profile τ_{xx} when comparing meshes 1 and 3.

To quantitatively compare the predictions of the velocity and stress τ_{xx} for the different meshes for geometry Planar 2, the percentage normalized error was calculated in the following way

$$PNE = Max_{j=1}^{N} \left(\frac{x_j^i - x_j^{ref}}{Max|x^{ref}|} \right) \times 100 \tag{2.15}$$

where N is number of discretization points, X_j is the value of the variable to be considered at a mesh point of the line of symmetry and X_j^{ref} are the values obtained in Mesh 3. The values of the percentage normalized error (PNE) for Deborah number $De = 3$ calculated using Equation 2.15 are shown in Table 2.3.

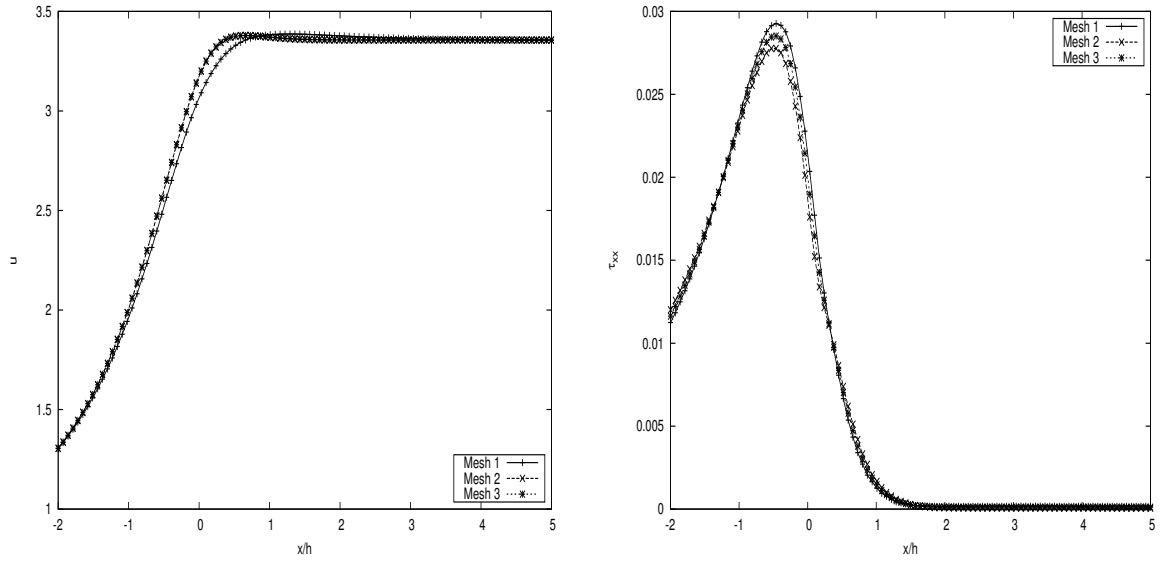

(a) (b)

FIGURE 2.20: Axial velocity $\boldsymbol{u}$ (a) and stress profile τ_{xx} (b) as functions of the axial position at the line of symmetry for the LCR stabilized Rolie-Poly model for Deborah number 3 and for the different meshes, using the Planar 2 geometry.

TABLE 2.3: Planar 2 PNE of mesh 1 and mesh 2 compared to mesh 3 for Deborah number 3

	Mesh	Percentage normalized error		
		U	τ_{xx}	N_1
Rolie-Poly(StrT)	M1	1.7464	10.9305	10.0934
	M2	0.7230	4.8755	4.5190
Rolie-Poly (LogT)	M1	1.6700	5.029	5.0220
	M2	0.5572	2.7506	2.3430

The PNE values for Mesh 2 in relation to Mesh 3 for both the velocity and stress profiles τ_{xx} are lower than 5% implying that greater accuracy is obtained by using Mesh 3. Due to high computational costs related to using Mesh 3, Mesh 2 will be used with an error of less than 5%.

2.5.1 Numerical Validation

We assess the accuracy of the Rolie-Poly viscoelastic solver by benchmarking our results against the known results for the Oldroyd-B model. Similarly to the lid-driven cavity validation, we recover the Oldroyd-B constitutive model directly

from our Rolie-Poly model, essentially achieved by switching off the λ_R terms. The numerical results for the Oldroyd-B model from the existing literature on 4:1 planar contraction flow, [66] are then used to benchmark and validate the results from our solver.

The Rolie-Poly constitutive model has a retardation constant of $\beta = 1/9$ and the simulations are done at low Reynolds number flow ($Re = 0.01$). The flow is simulated for a wide range of Deborah numbers $1 \leq De \leq 12$. The evolution of the non-dimensional corner vortex size X_R and the non-dimensional lip vortex size X_L as functions of Deborah number, De, are also compared with results from the existing literature. Tables 2.4 and 2.5 display results from existing literature for the Oldroyd-B model [66] compared with our simulated results of the recovered Oldroyd-B model from the constitutive Rolie-Poly model, for the different mesh sizes. Table 2.4 displays the non-dimensional corner vortex and Table 2.5 displays the results for the non-dimensional lip-vortex.

TABLE 2.4: Corner vortex size X_R as a function of Deborah number obtained using the different meshes

	M1			M2			M3		
De	[66]	LogT	StrT	[66]	LogT	StrT	[66]	LogT	StrT
1	1.360	1.360	1.359	1.362	1.361	1.361	1.363	1.363	1.363
2	1.173	1.173	1.171	1.171	1.171	1.176	1.170	1.170	1.221
3	0.978	0.977	0.976	0.969	0.968	0.963	0.969	0.968	1.241
4	0.808	0.807	0.809	0.788	0.787	0.977	0.785	0.783	1.084
5	0.674	0.673	0.675	0.641	0.640	0.888	0.636	0.631	1.074
6	0.590	0.592	0.593	0.536	0.530	0.898	0.526	0.570	1.073
7	0.600	0.629	0.764	0.465	0.456	0.968	0.450	0.471	1.054
8	0.875	0.850	0.944	0.419	0.462	1.013	0.400	0.440	1.059
9	1.235	1.124	1.044	0.633	0.619	1.039	0.358	0.505	1.171
10	1.475	1.335	1.126	1.123	1.084	1.098	0.328	1.014	1.366
12	1.836	1.628	1.418	1.621	1.385	1.281	1.242	1.127	1.418

The results are displayed for the range of Deborah numbers from 1 to 12 for the corner vortex size and for the lip vortex size, Deborah numbers 1 to 6. The lip vortex size is a more sensitive parameter than the corner vortex size.

Generally, for the corner vortex size, good agreement is observed between our, LCR based, results and those of Pimenta and Alves [66] for Deborah numbers

TABLE 2.5: Lip vortex size X_L as a function of Deborah number De computed in different meshes.

	M1			M2			M3		
De	[66]	LogT	StrT	[66]	LogT	StrT	[66]	LogT	StrT
1	0.056	0.055	0.045	0.044	0.044	0.036	0.038	0.038	0.034
2	0.132	0.132	0.131	0.115	0.117	0.119	0.097	0.100	0.106
3	0.241	0.241	0.205	0.191	0.193	0.207	0.160	0.163	0.204
4	0.385	0.387	0.374	0.290	0.292	0.317	0.387	0.384	0.298
5	0.590	0.597	0.402	0.447	0.480	0.486	0.593	0.351	0.350
6	0.852	0.845	0.443	0.649	0.686	0.536	0.852	0.509	0.412

1 to 5 and for the Meshes 1 and 2 and for Deborah numbers 1 up to 4 for the third mesh. The relative error for the values for Deborah numbers 1 to 4 for LCR approach is lower than 0.5 percent.

For the DEVSS method good agreement is observed for Deborah numbers 1 and 2 only with a relative percentage error of less than 3.5 percent for the first two meshes. The lip-corner vortex is a sensitive parameter and there is agreement for LCR for Deborah numbers 1 to 4 whereas for DEVSS, agreement is only observed for Deborah numbers 1 and 2.

The results indicate that our solver can be used with relative accuracy for Deborah numbers of up to 5, especially using the LCR stabilization method.

2.5.2 Comparison between DEVSS and LCR

Comparison of Rolie-Poly LCR and DEVSS stabilization approaches was done using Mesh 2 for Planar 2 due to the high computational cost of using Mesh 3. The axial velocity and axial normal stress as a function of the axial position at the line of symmetry for the Rolie-Poly model for different Deborah numbers were obtained. No significant difference was observed between the LCR and DEVSS methods in the axial velocities and as such only the velocity profiles for Deborah numbers 4 and 5 were presented, see Figure 2.21.

Figure 2.21 shows that the velocity profiles are indistinguishable, because they do not display substantial variations as with the stress profiles. The figure also

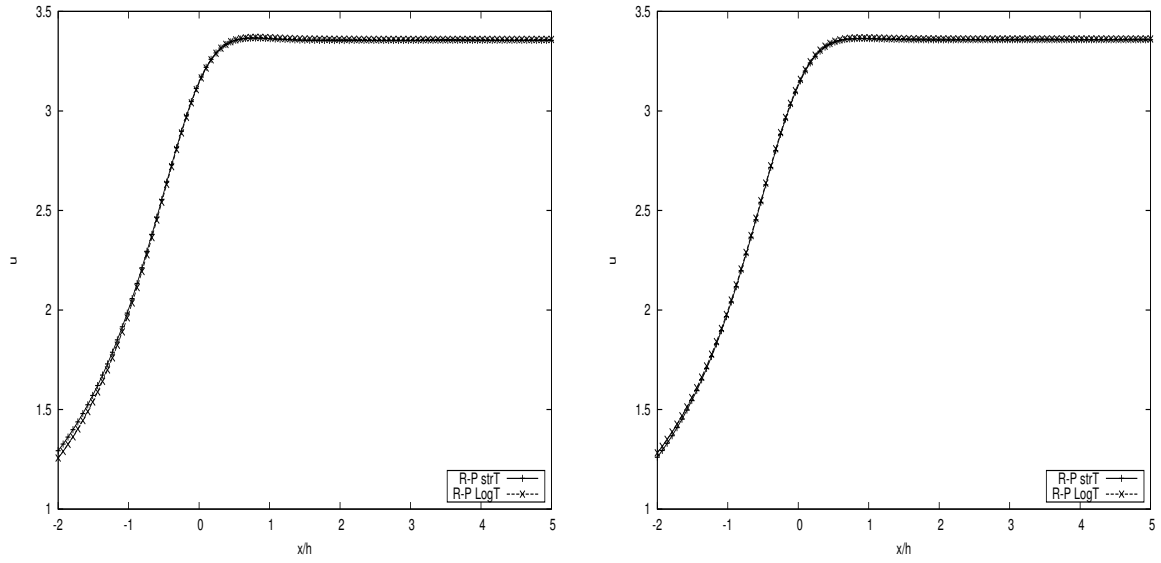

FIGURE 2.21: Axial velocity $\boldsymbol{u}$ as a function of the axial position at the line of symmetry for the Rolie-Poly model for Deborah numbers 4 (a) and 5 (b) using Planar 2, Mesh 2.

shows that the flow rapidly accelerates from the fully developed flow upstream into the smaller contraction channel leading to large extensional stresses near the contraction plane as was observed by [67] in their experimental work. This causes the maximum stress τ_{xx} to occur just upstream of the contraction plane as is seen in Figure 2.22. The stresses then recede from this maximum.

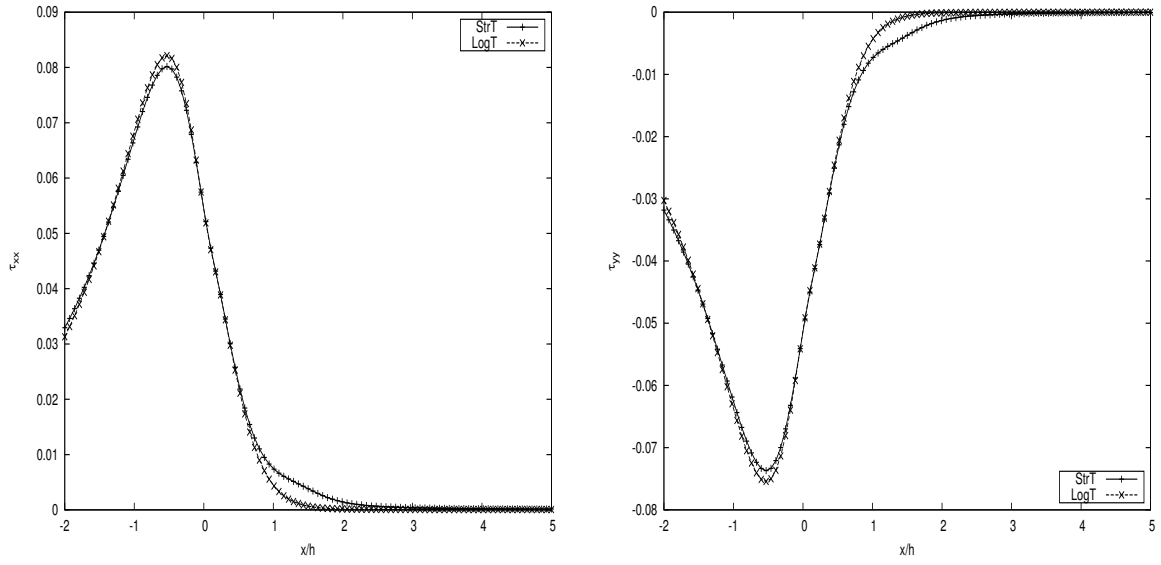

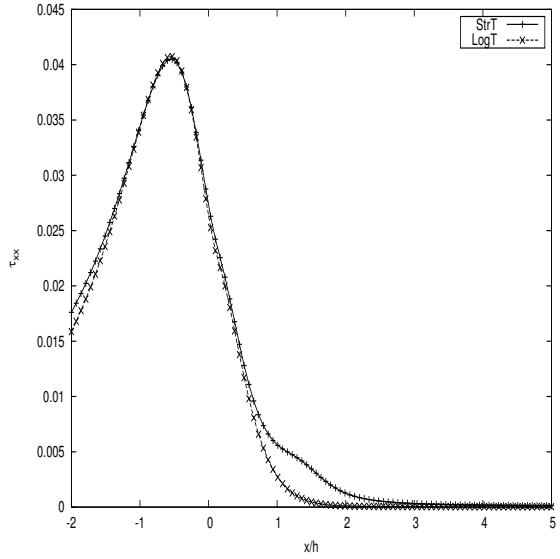
StrT
LogT
τxx
x/h

(c)

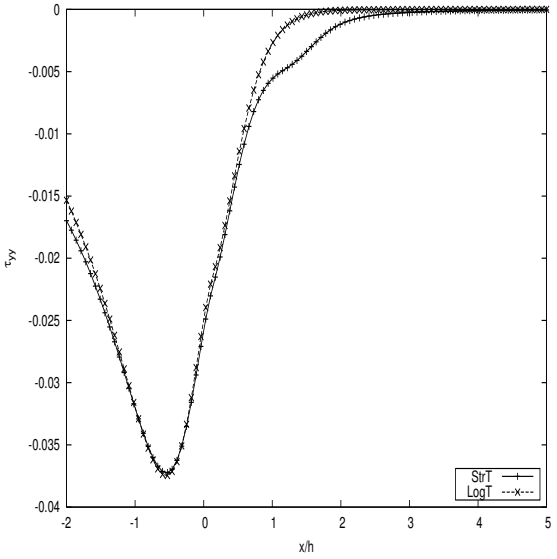
StrT
LogT
τyy
x/h

(d)

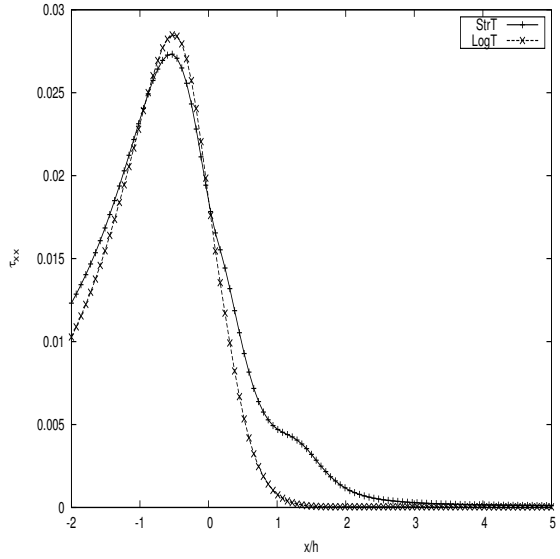
StrT
LogT
τxx
x/h

(e)

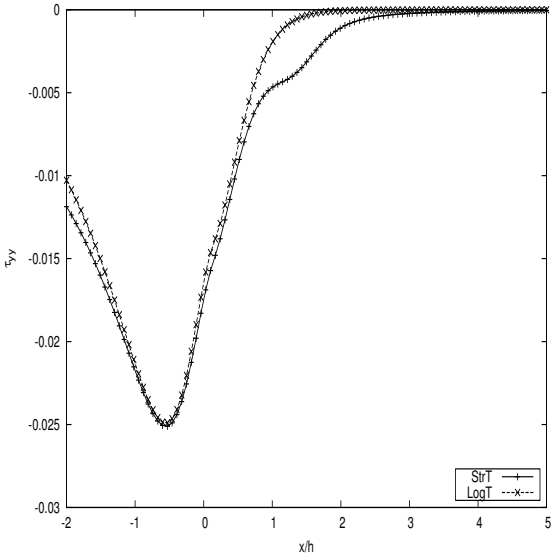
StrT
LogT
τyy
x/h

(f)

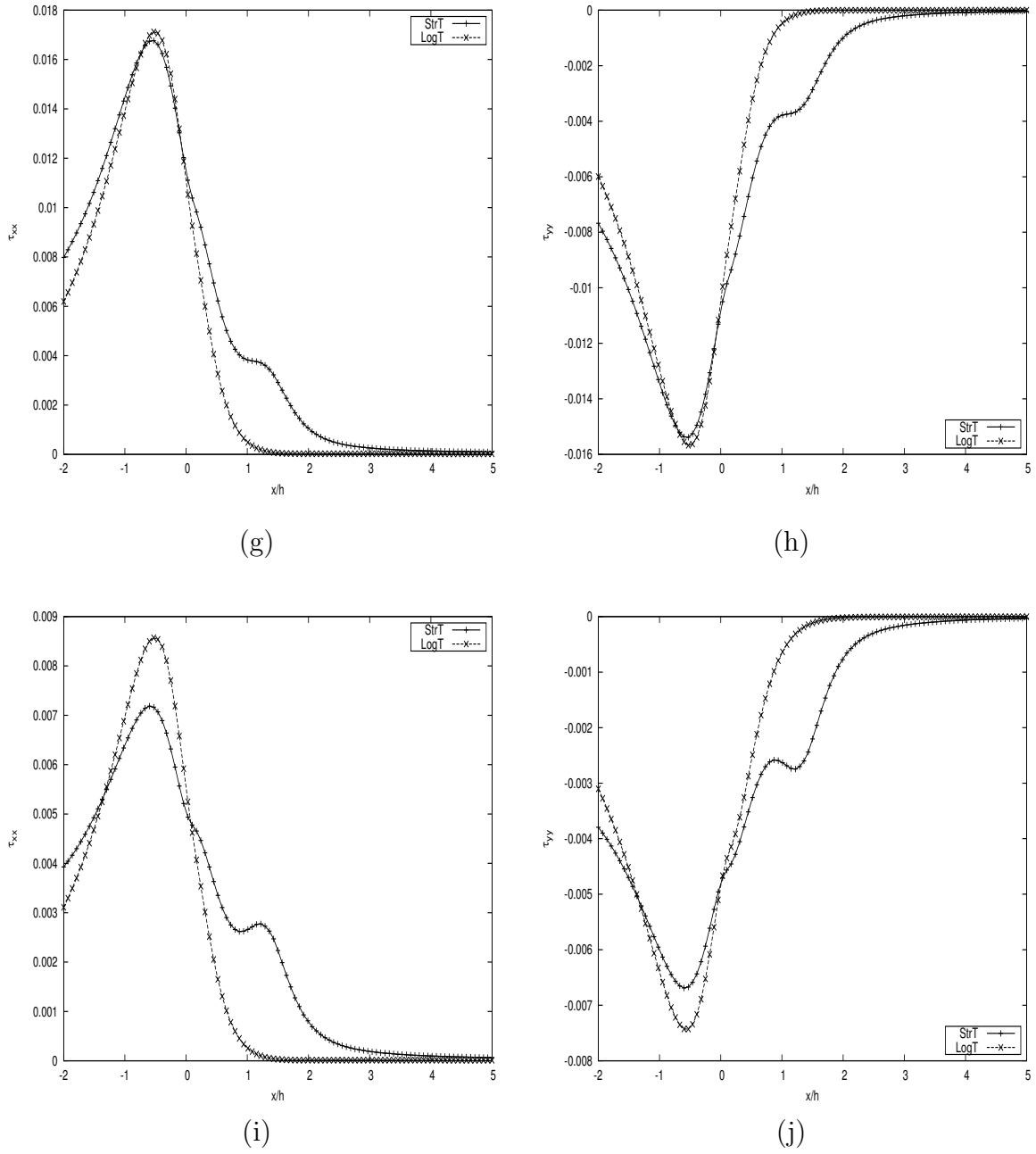

FIGURE 2.22: Simulation results comparing LCR (LogT) and DEVSS (StrT) Rolie-Poly constitutive equation for stress profiles τ_{xx} and τ_{yy} at the line of symmetry using Planar 2, Mesh 2, for $De = 1, 2, 3, 4$ and 5 respectively.

Unlike the velocity profiles, the polymer stress profiles τ_{xx} and τ_{yy}, on the other hand, do display significant differences for the different Deborah numbers as illustrated in Figure 2.22. We also notice, from Fig. 2.22, that increasing the Deborah number leads to a decrease in the maximum value of stress value τ_{xx} as is reported in [67].

The velocity profile and stress profiles τ_{xx} and τ_{yy} are plotted at different positions as shown in Figure 2.23. No significant difference is observed in the velocities, differences are however observed in the stress profiles.

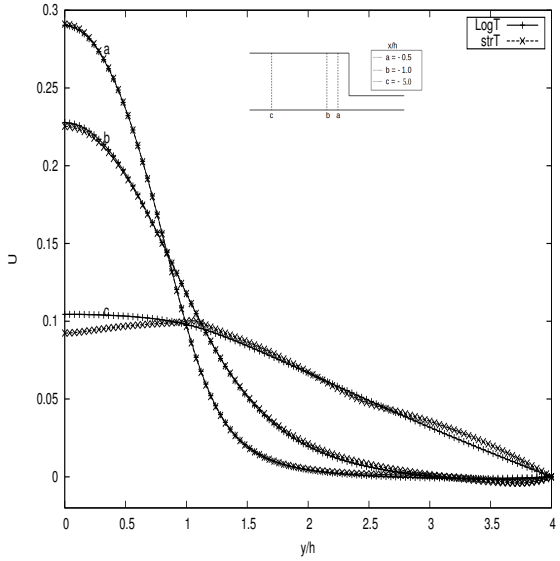

(a)

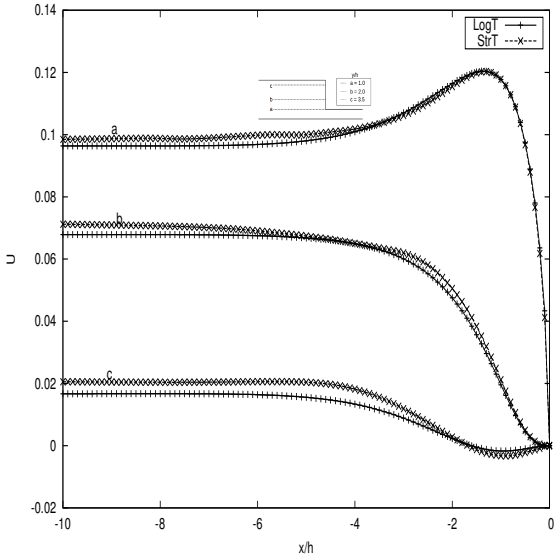

(b)

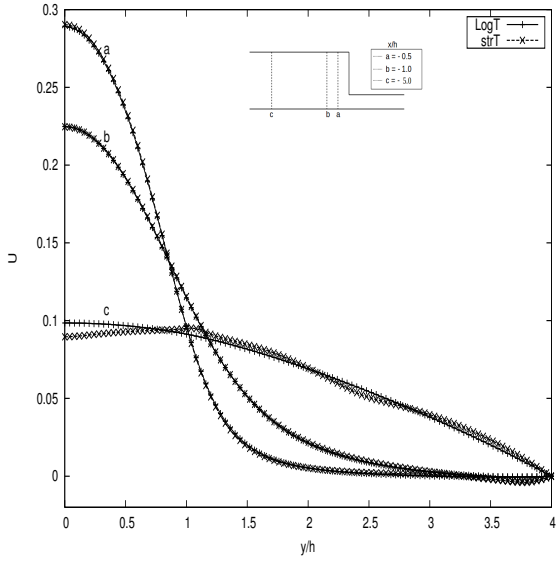

(c)

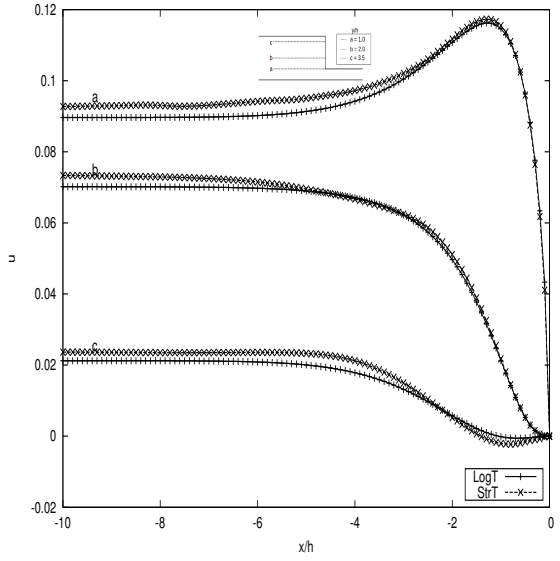

(d)

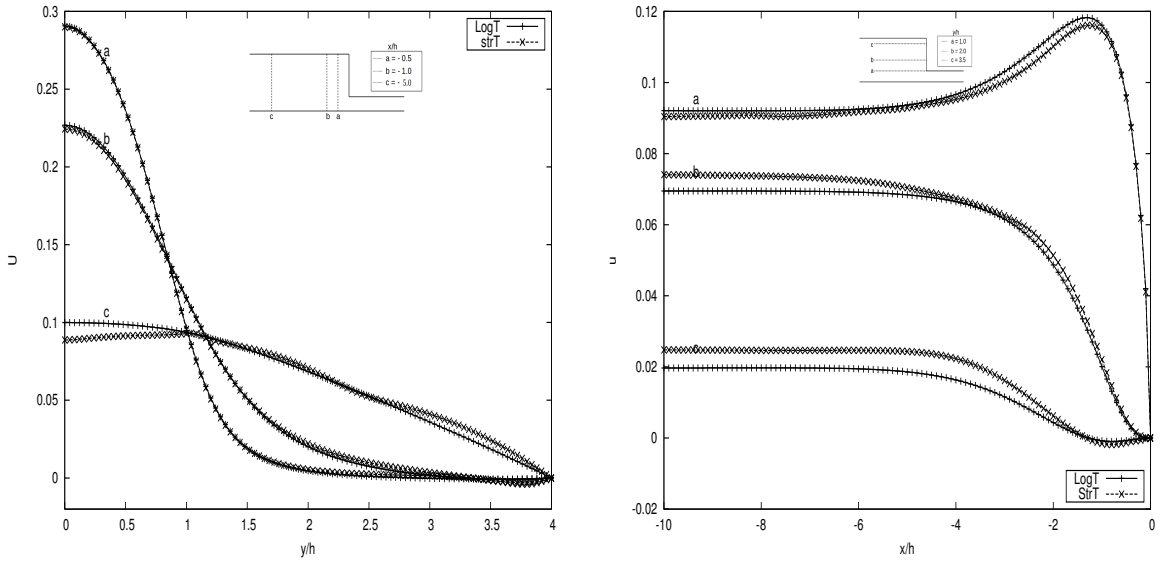

(e) (f)

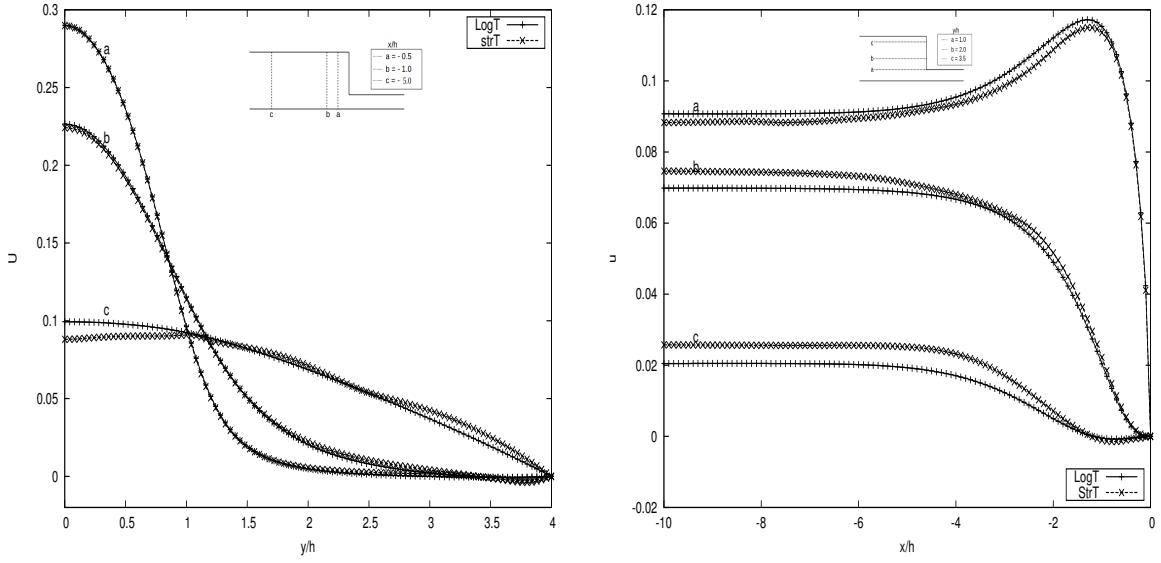

(g) (h)

Figure 2.23 presents the axial velocity profiles at different x positions (LHS) and different y positions (RHS) in the upstream channel. It is expected that there will be slight differences between the LCR and DEVSS method since the velocity profiles have insubstantial variations as opposed to the stress profiles. Figures 2.24 and 2.25 which present the stress profiles at different x and y positions, therefore display a greater disparity between the LCR and DEVSS methods with increasing Deborah number. This could be due to the LCR method's ability to mitigate the HWNP better than the DEVSS.

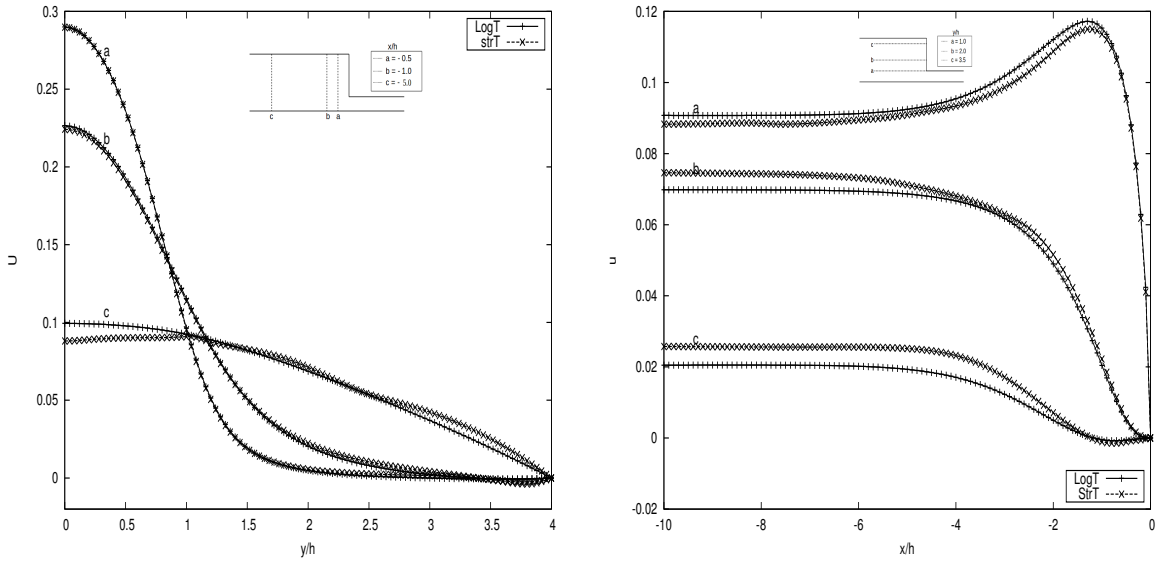

(i) (j)

FIGURE 2.23: Simulation results comparing LCR (LogT) and DEVSS (StrT) Rolie-Poly constitutive equation for velocity profile u_x using Planar 2, Mesh 2, at different positions in the geometry for $De = 1, 2, 3, 4$ and 5 respectively.

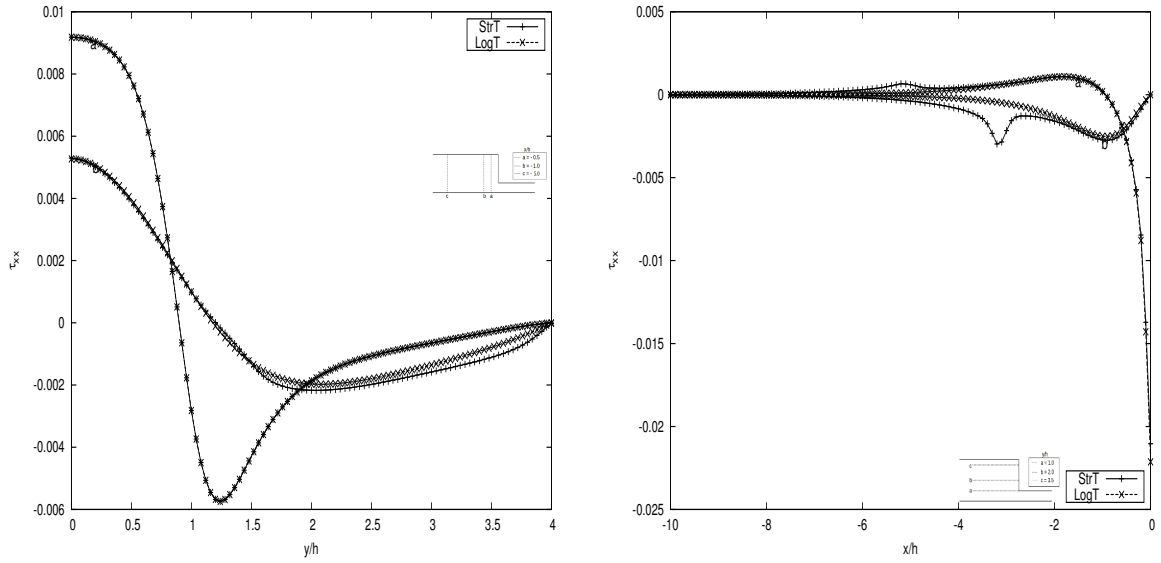

(a) (b)

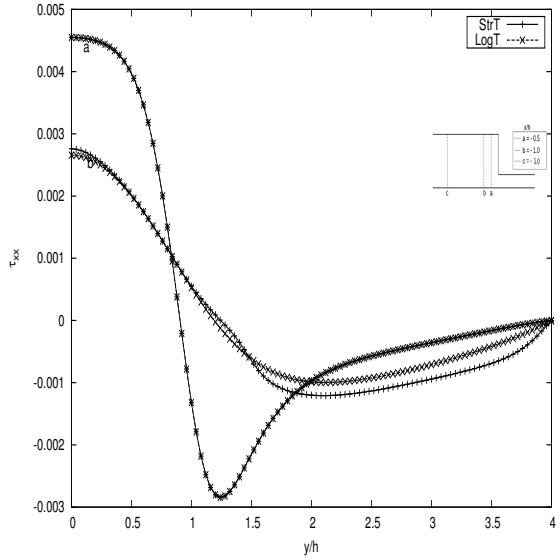
StrT
LogT
a
b
τ_{xx}
y/h

(c)

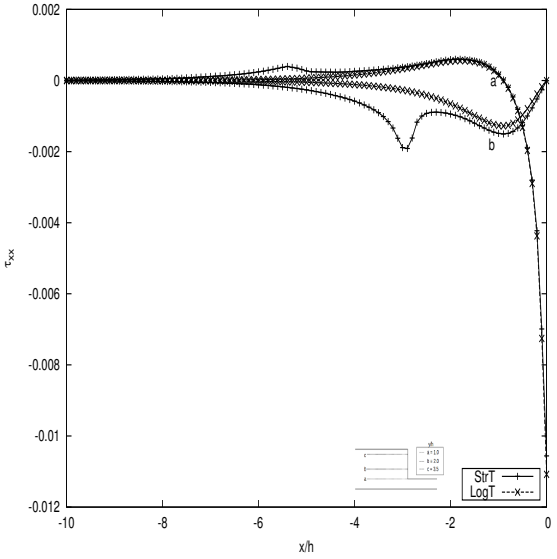
a
b
StrT
LogT
τ_{xx}
x/h

(d)

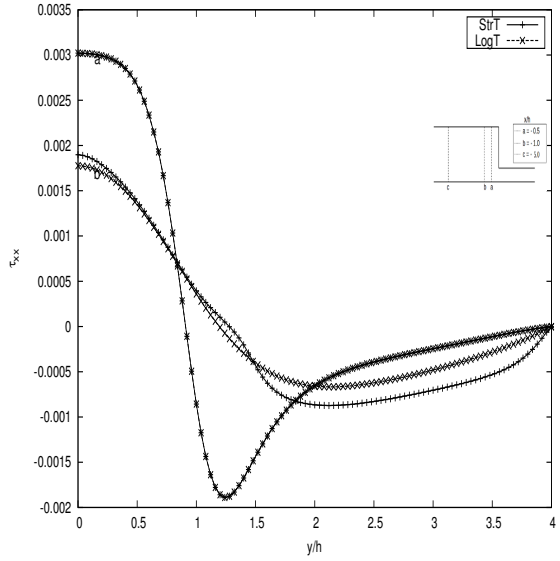
StrT
LogT
a
b
τ_{xx}
y/h

(e)

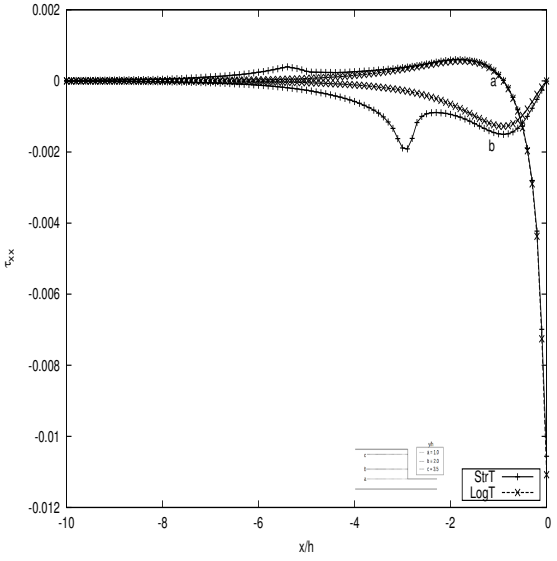
a
b
StrT
LogT
τ_{xx}
x/h

(f)

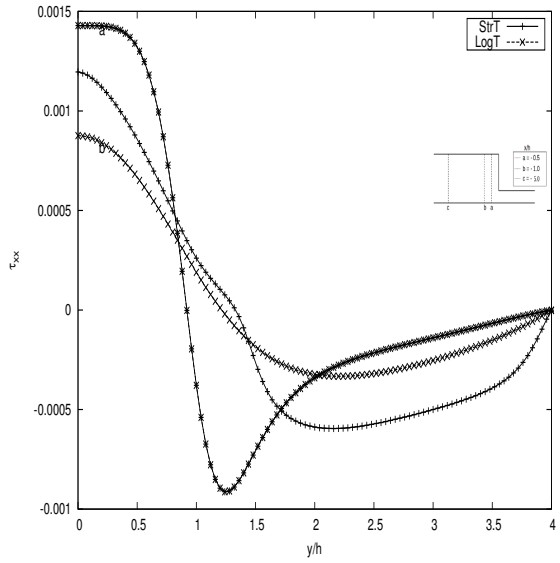

(g)

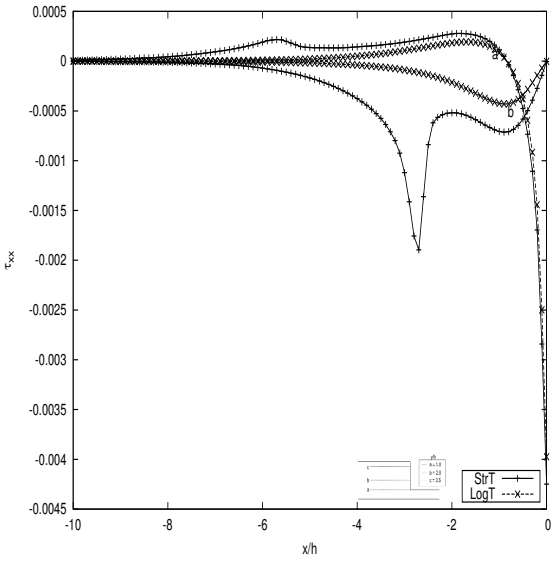

(h)

FIGURE 2.24: Simulation results comparing LCR (LogT) and DEVSS (StrT) Rolie-Poly constitutive equation for stress profile τ_{xx} using Planar 2, Mesh 2, at different positions in the geometry for $De = 1, 2, 3$ and 4 respectively.

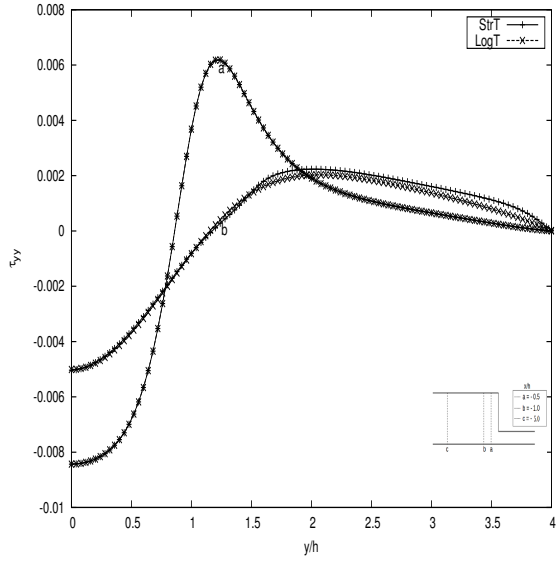

(a)

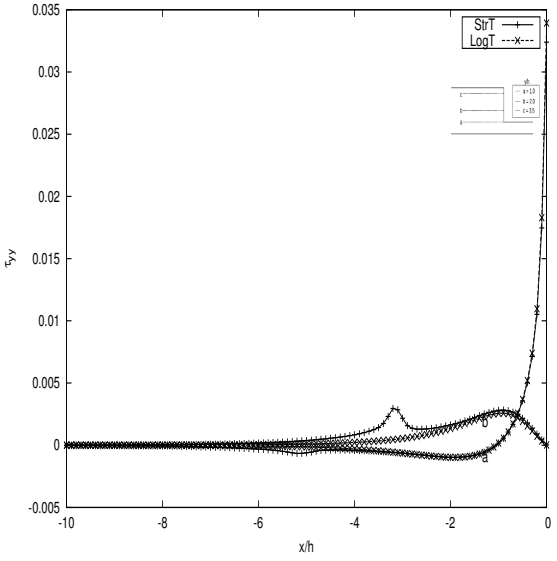

(b)

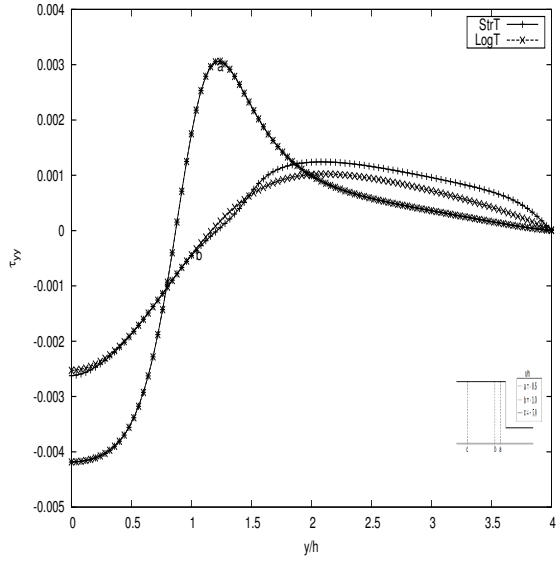

(c)

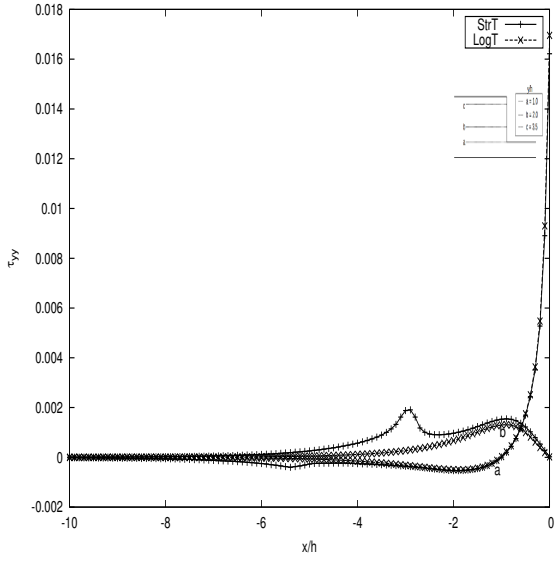

(d)

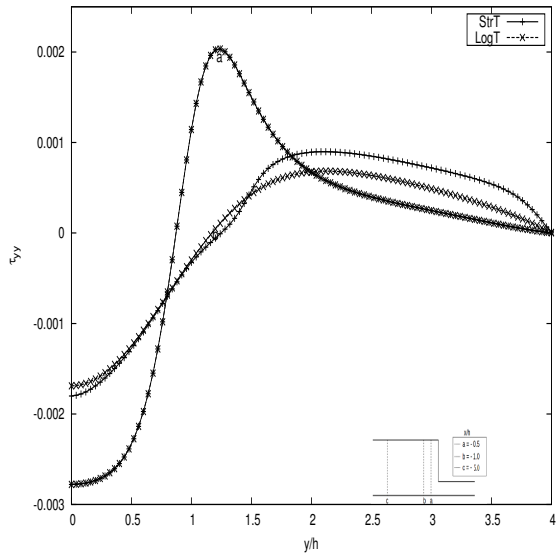

(e)

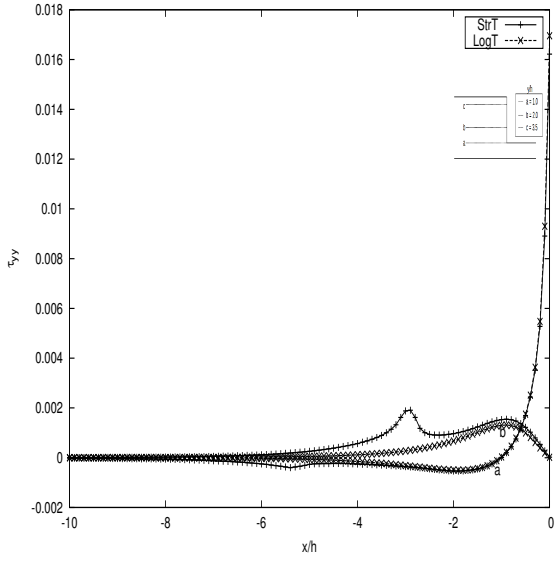

(f)

2.5.3 Vortex growth

We obstain streamlines are obtained at the end of simulation. From figure 2.26, it is clear that there is a reduction in the corner vortices with an increase in the Weissenberg number. Similar behaviour was observed by both Alfonso *et al.* [68] and Raphaël *et al.* [2] in their 4:1 contraction simulation of the Oldroyd-B model. The corner vortices in all LCR (LogT) simulations (RHS) are smaller than those calculated with DEVSS (StrT) simulations (LHS).

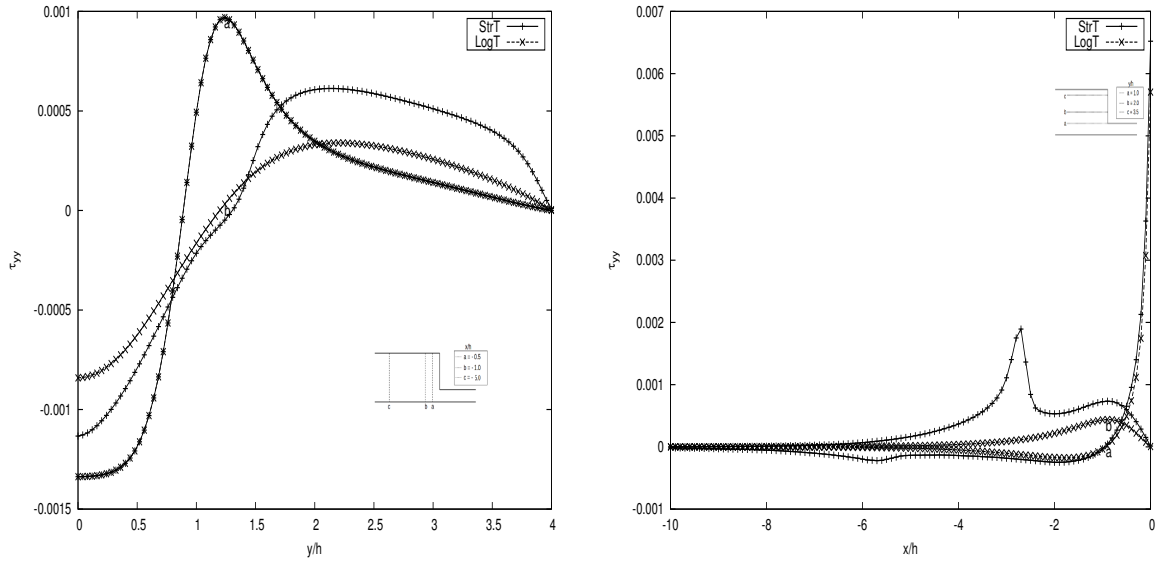

(g) (h)

FIGURE 2.25: Simulation results comparing LCR (LogT) and DEVSS (StrT) Rolie-Poly constitutive equation for stress profile τ_{yy} using Planar 2, Mesh 2, at different positions in the geometry for $De = 1, 2, 3$ and 4 respectively.

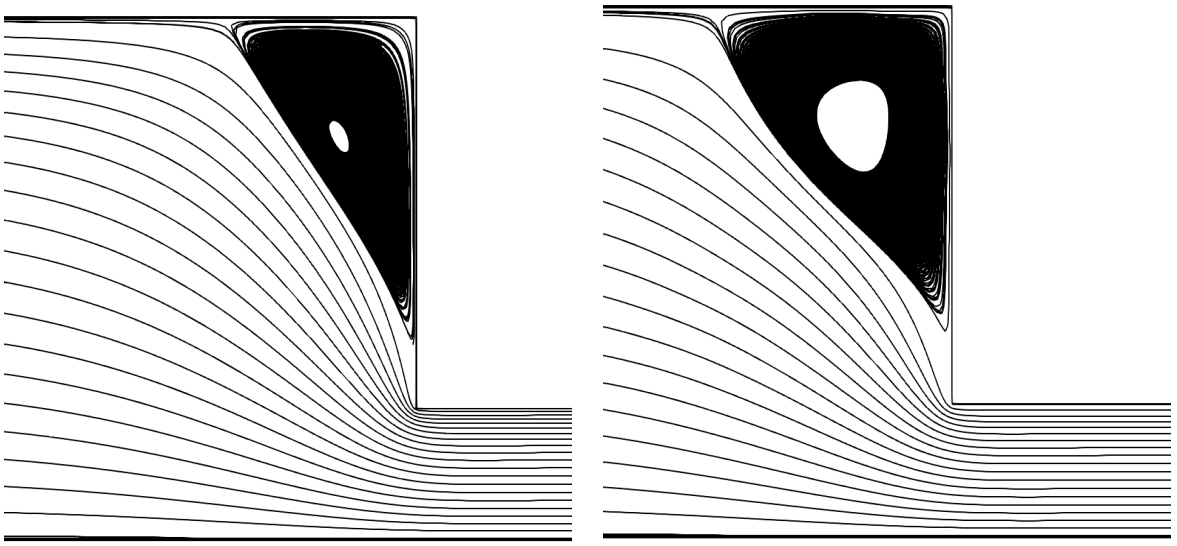

(a) (b)

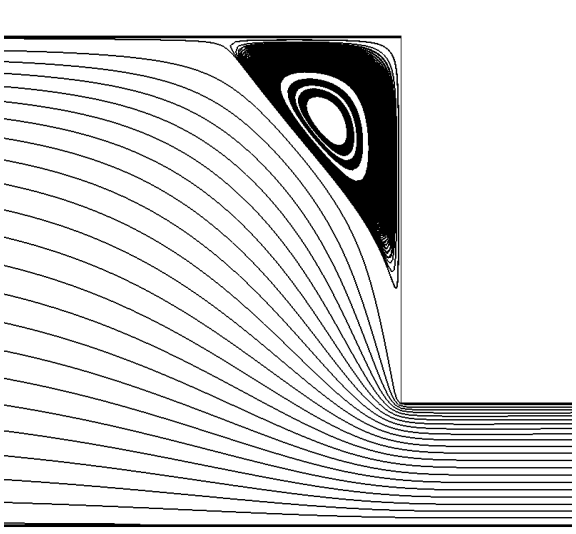

(c)

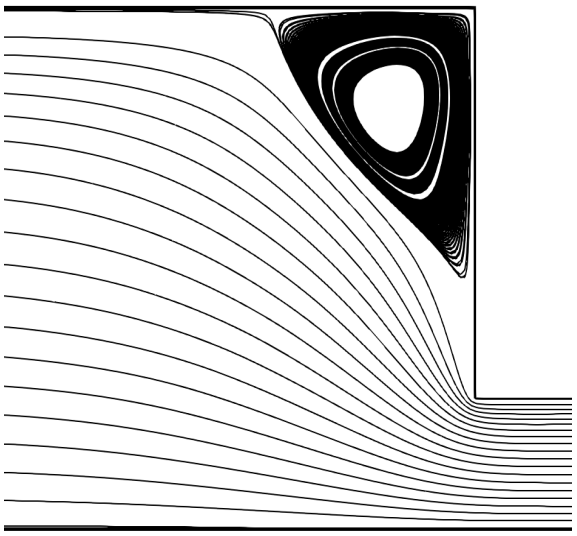

(d)

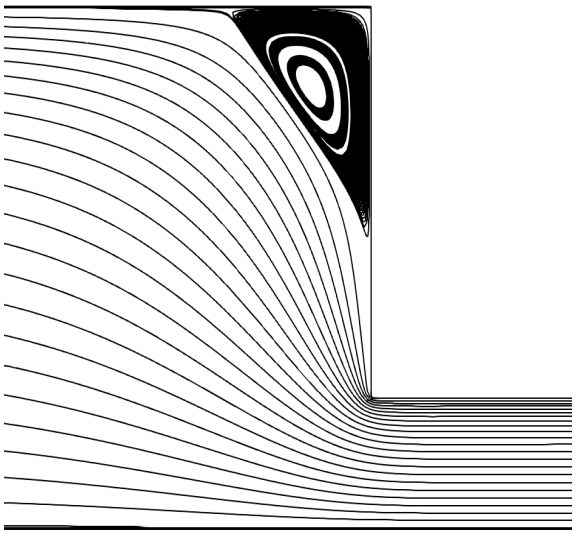

(e)

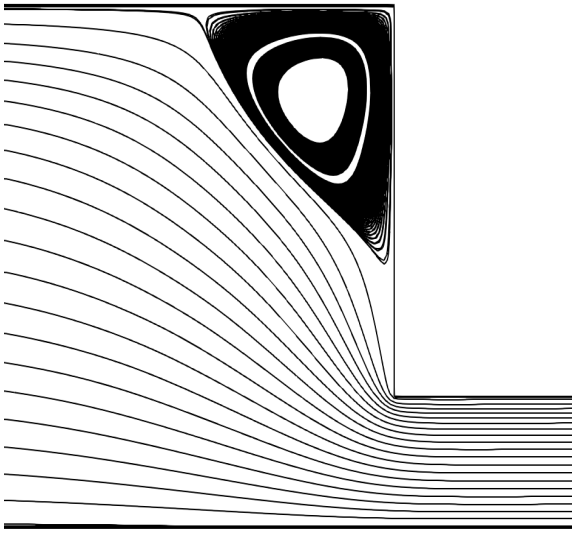

(f)

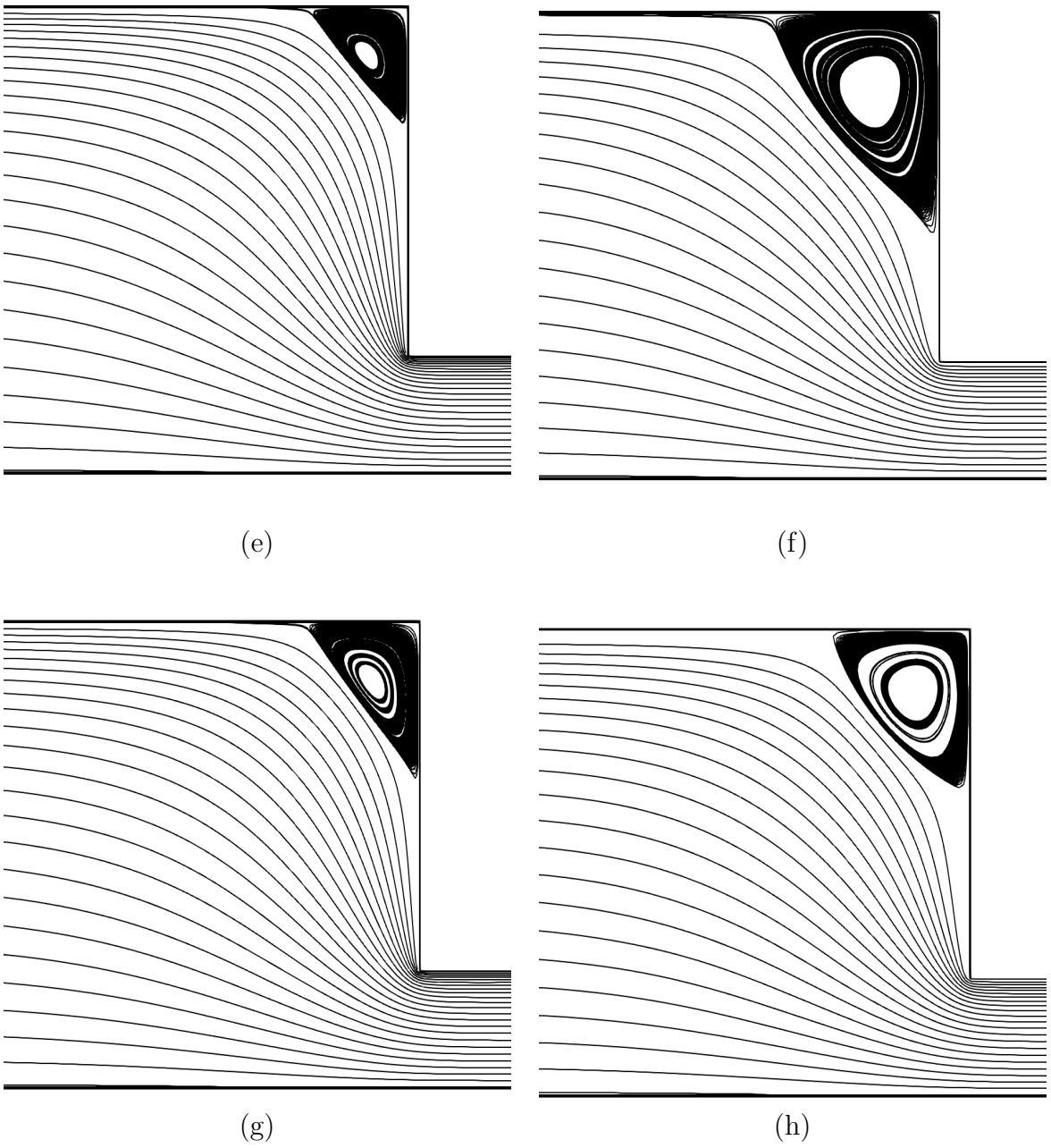

(e) (f)

(g) (h)

FIGURE 2.26: Streamline patterns in the contraction computed using Planar 2, Mesh 2, for $De = 1, 2, 3, 4$ and 5 respectively for LCR(LogT) simulations (RHS) and DEVSS (StrT) simulations (LHS).

2.6 COMPARISON WITH RHEOTOOL

In the course of this study, an FVM solver capable of handling complex fluids governed by the Rolie-Poly constitutive equation was added to the toolbox RheoTOOL to be used with OpenFOAM by Pimenta and Alves[66, 69]. We simulate Rolie-Poly fluid flow using the RheoTool solver 4:1 planar geometry and

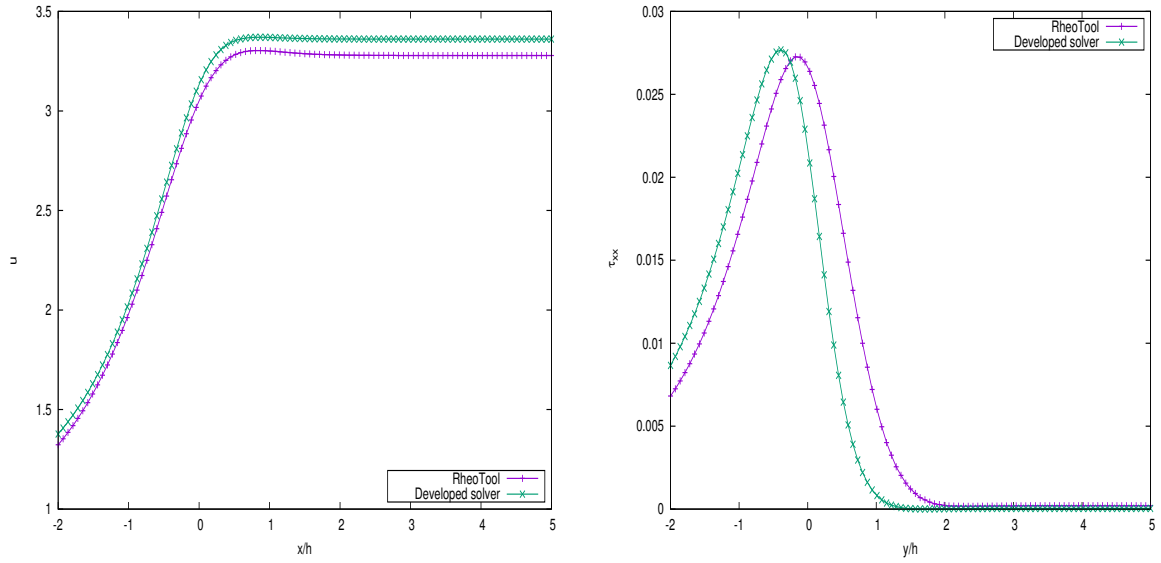

(a) (b)

FIGURE 2.27: Comparison of Axial velocity **u** and stress profile τ_{xx} as a function of the axial position at the line of symmetry for the Rolie-Poly model for Deborah number 1 using Planar 2, Mesh 2

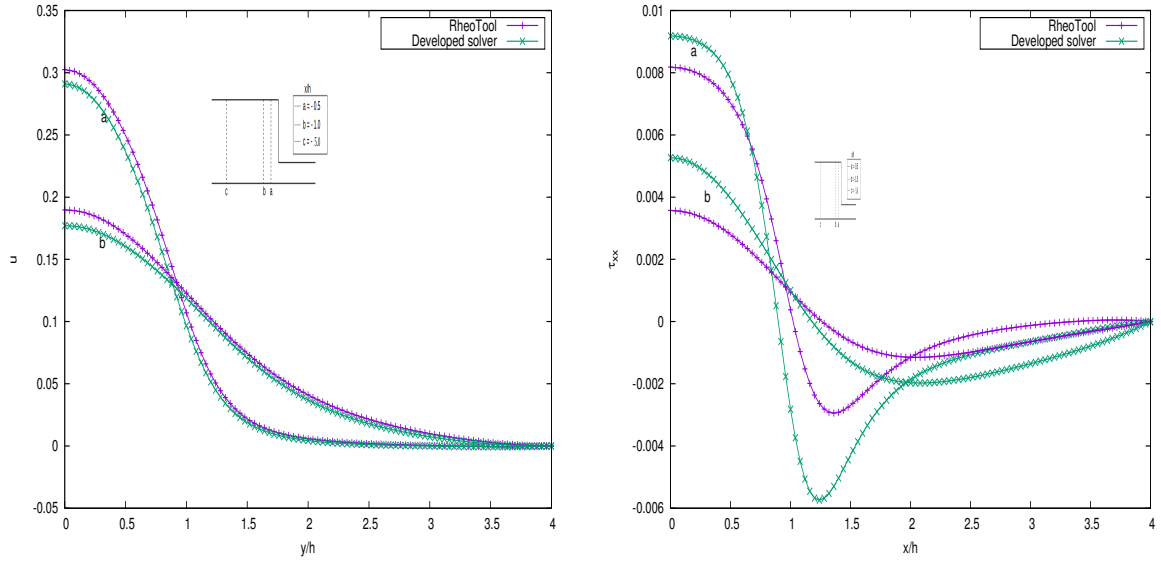

(a) (b)

FIGURE 2.28: Comparison of velocity profile **u** and stress profile τ_{xx} at different x positions on the geometry for Deborah number 1 using Planar 2, Mesh 2

boundary conditions stated the previous section for Deborah number 1. The stress values presented for the RheoTool solver have been scaled by a factor of 100. Comparison of the two solvers are presented in graphs 2.27, 2.28 and 2.29.

It is clear from graphs 2.27, 2.28 and 2.29 that there is no significant difference in

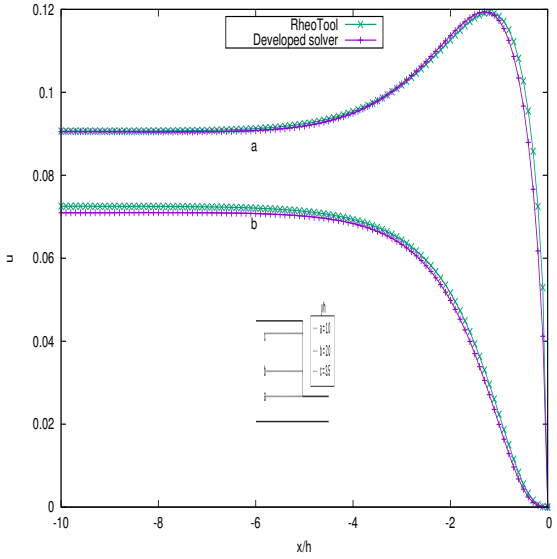

FIGURE 2.29: Comparison of velocity profile **u** at different y positions for Deborah number 1 using Planar 2, Mesh 2

the velocity profiles. However, there is some difference in the stress profiles as a scale of 100 had to be applied for comparisons be done. Both solvers predict the same flow behaviour albeit with a difference in the values of stress. This discrepancy in the value of stress could be explained by the fact that the RheoTool used a Rolie-Poly model with finite extensibility. To ascertain whether finite extensibility make a difference, further research needs to be done. It has been shown in [70] that the finite extensibility underestimate the values of principle stress difference(PSD). It is therefore important to research further on what the effect on stress profiles.

2.7 DISCUSSION AND CONCLUSION

We have developed and numerical solver for the computation of visco-elastic fluid flows. The solver is based on the finite volume method and implemented in the open source OpenFOAM® software platform. Additionally the solver is developed specifically for the simulation of flows of visco-elastic fluids that are governed by the Rolie-Poly constitutive model. The Rolie-Poly model reduces to the Oldroyd-B model for certain values of the material constants. We take advantage of this

relationship to validate our solver based on the existing benchmark solutions for Oldroyd-B fluids. We in particular focus attention on the two benchmark problems; lid-driven cavity flow as well as the 4:1 contraction flow. Such benchmark comparison of our data with the existing literature, [2] and [66], shows generally good agreement.

We report a significant improvement in dealing with the High Weissenberg Number Problem (HWNP) when using the LCR approach. The DEVSS stabilization method is also reliable, and also agrees with the results from the existing literature, but at lower values of the Deborah numbers than those achievable with the LCR approach. Based on our results, we can therefore confirm than the LCR stabilization technique is more reliable than widely used DEVSS stabilization method. We therefore recommend the LCR technique for the numerical stabilization of visco-elastic flow computations going forward.

In conclusion, this work has presented a new solver for the simulation of flows of visco-elastic fluids governed by the Rolie-Poly constitutive model. The results show that the solver is consistent with expectations as can be observed from the favourable comparison with results from the existing literature. Our results also demonstrate that the LCR method better mitigates against the HWNP as compared to the widely employed DEVSS method. Further studies however need to be conducted to investigate the disparities in the results for Deborah numbers greater than 7 especially for the LCR representation. In particular, it may well turn out that our results are indeed more accurate. Further theoretical, experimental and computational investigations are therefore invaluable in this direction.

ACKNOWLEDGEMENT

We would like to acknowledge support received from the Organisation for Women in Science in Developing countries (OWSD) and the Swedish International Development Cooperation Agency (SIDA). The resources from the Centrer for High Performance Computing (CHPC) in South Africa are gratefully acknowledged.

Chapter 3

Shear banding of flows of fluids governed by the Rolie-Poly two-fluid model using OpenFOAM [1]

3.1 ABSTRACT

Non-Newtonian flows can exhibit shear-banding since they are susceptible to flow instabilities. In this work, we give a numerical study of shear banding based on flow induced non-uniformities using the Rolie-Poly constitutive equation. The Rolie-Poly constitutive equation is chosen because it expresses precisely the shear rheometry of polymer solutions for a vast number of strain rates. To implement this, we use the two-fluid model where the stress is coupled with concentration equation. The work will be simulated using an efficient numerical methodology implemented in the software package OpenFOAM that we developed and validated. The methodology can accurately simulate the flow of complex fluids represented

[1] The contents of this chapter are from Abuga and Chinyoka [71]

by, among others, the Rolie-Poly constitutive equation. The numerical algorithm is based on the Finite volume Method (FVM).

Two stabilization techniques are used in the simulation of the flow, the Log-Conformation Reformulation and the Discrete Elastic Viscous Stress Splitting. Validation of shear-banding using the Giesekus and Johnson-Segalman models show good agreement with existing literature using the DEVSS technique. Comparison of the Rolie-Poly simulated results with existing literature for the concentration profile is also in good agreement.

3.2 INTRODUCTION

Shear banding is an occurrence observed in flows in a simple shear device. These flows develop a localized bands due to shear rates flow instabilities causing a difference in shear rates. These localised bands are called shear bands (see Figure 3.1). Some of the materials in which shear banding has been observed include worm-like micelle solutions [72, 73, 74], foams [75], granular flows [76], soft glasses [77], telechelic polymers [78], polymer solutions [79], and polymer melts [80]. A review with focus on polymer fluids and soft glass materials has been done by [81].

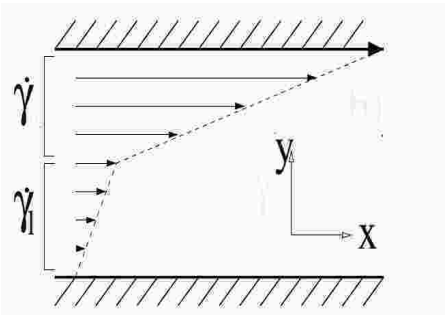

FIGURE 3.1: Shear banding profile showing two different shear rates (shear bands)

Some of the experimental methods used for observation of shear bands include Particle Tracking Velocimetry (PTV) [82], Particle Image Velocimetry (PIV) [83], PIV combined with global rheology [84], Optical Coherence Tomography Velocimetry [85] and Flow-Induced Birefringence (FIB) measurement [86, 87]. Other methods include Nuclear Magnetic Resonance (NMR) velocity imaging, which permits direct determination of velocity and consequently calculating the shear rate [88].

In an experimental approach designed and validated by Helgeson *et al.* [89], which enabled the direct measurement of the local fluid make-up for the complex fluids in shear flow, it was conclusively demonstrated that for worm-like micelle (WLM) fluids under shear flow, the coupling of flow-concentration has an effect on the concentration gradient. Observed results for the concentrations showed that the

development of concentrated paranematic phase had an effect on the isotropic phase.

Despite the increased research in shear banding, the mechanisms that gives rise to shear bands in semi-dilute polymers are not always the same and are not well understood [90]. Some current studies show that a non-monotonic shear-rate – shear-stress relationship is sufficient cause for shear banding and hence the Johnson-Segalman model is one of the most extensively used framework for shear banding studies, see for example [91, 92, 93, 3] and the references therein. To analyse the effects of stress diffusion and the size of annular gap on the choice of shear stress path for non-isothermal flow, a diffusive Johnson-Segalman (DJS) constitutive model has been used [93].

A Johnson-Segalman model which was modified by adding a general term was used to analyse a steady planar shear flow, [94]. It was observed that the added non-local term allowed for determination of the stress at which two "phases" coexisted. The behaviour of Johnson-Segalman fluid in couette flow was also investigated in [94] via analytical techniques, numerical simulation and controlled experiments to explain spurt phenomena which is a physical manifestation of shear banding. Paul et al. [95] implemented the Johnson-Segalman model in the OpenFOAM open-source software. Their simulations showed good agreements with experimental results.

In addition to the constitutive model based non-monotonic stress–strain mechanisms, an alternative mechanism to trigger shear banding in flows of viscoelastic fluids is, induced concentration fluctuations. The premise of this concept is the Helfand-Fredrickson mechanism (HF). It enables polymer migration due to the stress gradient as a result of concentration inhomogeneity, thus the polymer concentration becomes non-uniform [96].

In the study of Hua *et al.* [97], it was unclear whether small scale concentration fluctuations were responsible for the shear thinning to banding transition but it was observed that the large scale fluctuations were not the causative mechanism for shear banding since the relaxation time of these fluctuations was greater than the shear bands' life span. They observed steady state shear only in the solution with a non-monotonic constitutive relation and global migration had no significant effect on the shear banding as there was no distinction in the concentration profiles of the shear bands.

The effect of coupling concentration and stress using the two-fluid model on the formation of shear bands has been clearly explained in [98]. It is clear from the phase diagrams that the concentration affects shear banding since an increased concentration caused normal micellar strain component gradients to be steeper.

The Rolie-Poly constitutive model was used by Adams and Olmsted because of its ability to capture instabilities related to shear banding. Shear bands were observed for flows with sufficiently non-homogeneous aggregate stress and transient phenomena displayed inhomogeneities akin to shear banding, even for weakly stable fluids [99]. They later on used the same model to study transient shear banding in entangled polymers and showed that instability was triggered by perturbations that were caused by inhomogeneous stress profiles. A similar behaviour is observed for entangled polymer solutions [100].

Using the stress-concentration coupling via a two fluid model for the Rolie-Poly constitutive equation, Cromer *et al.* [6] showed shear banding for the velocity profile. They later extended their study to show that flow-induced non-uniformities of concentration in polymer solutions under extensional flow can trigger shear banding notwithstanding the monotonicity of shear-stress – shear-rate relationship. The constitutive model used was the modified Rolie-Poly model that takes into account finite extensibility since it provides a realistic rheological projection for entangled

polymeric solutions [101]. In [6], it was shown that with an imposed initial defect in the polymer concentration, the velocity still reached a banded steady state despite undergoing a non-trivial temporal evolution. Incorporating identical elastic input in their extended equation, they observed that there was no effect of the elastic input in the kinetics of a single phase, incompressible polymer fluid. However, it had an effect in the two-fluid model as thus, it could not be neglected. For Taylor-Couette geometry, shear bands were observed at significantly lower times making the Taylor-Couette geometry conducive for experimental studies [102].

Despite all the studies done, there is little available literature on the investigation of shear banding via the Rolie-Poly constitutive equation. We therefore seek to use the OpenFOAM platform to investigate shear banding using the Rolie-Poly constitutive equation. The concentration is coupled to stress profile and as in [6], we use a two fluid approach for the study.

3.3 Governing Equations

We implement our constitutive equation in open source software OpenFOAM using a developed viscoelastic solver for the Rolie-Poly constitutive equation. The code is based on the finite volume method (FVM). We follow a two-fluid model approach in which the polymer and the solvent are considered as two separate, inter-penetrating fluids. The velocities of the solvent ($\mathbf{v}_s$) and polymer ($\mathbf{v}_p$) are coupled by a friction term. A more detailed modelling of the equations can be found in [6, 7]. The volume-averaged velocity is given as $\mathbf{v} = \phi_s \mathbf{v}_s + \phi_p \mathbf{v}_p$ where ϕ_s and ϕ_p denote the volume fraction of the solvent and polymer respectively, whose sum is one. Thus, the continuity equation reads,

$$\nabla \cdot \mathbf{v} = 0. \tag{3.1}$$

The momentum equations for the solvent and polymer fluids respectively read,

$$\frac{D}{Dt}(\rho_s \phi_s \mathbf{v}_s) = \eta_s \nabla^2 \mathbf{v}_s - \nabla p - \zeta(\mathbf{v} - \mathbf{v}_p), \tag{3.2}$$

$$\frac{D}{Dt}(\rho_p \phi_p \mathbf{v}_p) = \nabla \cdot \boldsymbol{\sigma}_p - \nabla \pi_0 + \zeta(\mathbf{v} - \mathbf{v}_p), \tag{3.3}$$

where π_0 is the osmotic pressure, $\boldsymbol{\sigma}_p$ is the polymer elastic stress, ζ is a friction coefficient and ϕ is the local volume fraction. For $\phi \ll 1$ it is assumed that the polymer inertia is negligible and in addition to that, the total inertia in the system can be ignored for certain flow conditions. Thus the left hand side of Eqs. (3.2) and (3.3) are usually set to zero. The two equations can then added to obtain an overall momentum balance equation which is written as,

$$\eta_s \nabla^2 \mathbf{v} + \nabla \cdot \boldsymbol{\sigma}_p - \nabla(p + \pi_0) = 0. \tag{3.4}$$

The polymer velocity can then be obtained as,

$$\mathbf{v}_p = \mathbf{v} + \left(\frac{1}{\zeta}\right)(\nabla \cdot \boldsymbol{\sigma}_p - \nabla \pi_0). \tag{3.5}$$

The osmotic pressure π_0 is determined from the mixed free energy,

$$\pi_0 = \chi_0^{-1}\left[\frac{1}{2}\phi^2 - \xi\phi\nabla^2\phi + \frac{1}{2}\left(\phi\frac{\partial \xi^2}{\partial \phi} - \xi^2\right)|\nabla\phi|^2\right], \tag{3.6}$$

where χ_0 is the osmotic susceptibility and ξ is the correlation length.

For the stress equation, we will employ the Rolie-Poly constitutive equation of Likhtman and Graham [26] to model the viscoelastic stress. At present, the Rolie-Poly model remains the most advanced differential constitutive formulation of the Doi-Edwards tube models for linear entangled polymer melts. The Rolie-Poly

constitutive equation is modified to include the relative motion between the solvent and the polymer, thus the configuration tensor equation is given as

$$\frac{\partial \mathbf{Q}}{\partial t} + \mathbf{v}\cdot\nabla\mathbf{Q} - \mathbf{Q}\cdot\nabla\mathbf{v} - (\nabla\mathbf{v})^T\cdot\mathbf{Q}$$

$$+\left\{\frac{1}{\zeta}\left[\nabla\cdot\boldsymbol{\sigma}_p - \nabla\pi_0\right]\cdot\nabla\mathbf{Q} - \left(\nabla\frac{1}{\zeta}\left[\nabla\cdot\boldsymbol{\sigma}_p - \nabla\pi_0\right]\right)^T\cdot\mathbf{Q} - \mathbf{Q}\cdot\nabla\frac{1}{\zeta}\left[\nabla\cdot\boldsymbol{\sigma}_p - \nabla\pi_0\right]\right\}$$

$$= -\tau_d^{-1}(\phi)(\mathbf{Q}-\mathbf{I}) - 2\tau_R^{-1}(1-\lambda^{-1})\left[\mathbf{Q} + \beta\lambda^{2\delta}(\mathbf{Q}-\mathbf{I})\right], \tag{3.7}$$

where $\mathbf{Q}$ is the conformation tensor, λ is the stretch parameter defined as $\sqrt{\mathrm{tr}(\mathbf{Q})/3}$, τ_d is the relaxation time, τ_R is the Rouse relaxation time, and β is the convective-constraint release (CCR) parameter which varies from 0 to 1. $\mathbf{I}$ is the identity tensor and tr denotes the trace. To ensure the monotonicity of the polymer stress equation, the CCR parameter, β is set to 1. The empirical parameter, δ, is obtained from experimental data and takes the value of $-1/2$.

To enable comparison with the results in the existing literature, we use the non-dimensional set of equations as given in [6]. The polymer stress equations, Eq. (3.7), is non-dimensionalized via the polymer velocity equation, Eq. (3.5). The resultant set of non-dimensional equations read,

$$\frac{\partial \mathbf{Q}}{\partial t} + \mathbf{v}_p\cdot\nabla\mathbf{Q} - \mathbf{Q}\cdot\nabla\mathbf{v}_p - (\nabla\mathbf{v}_p)^T\cdot\mathbf{Q} = -\tau_d^{-1}(\phi)(\mathbf{Q}-\mathbf{I}) - 2\theta(1-\lambda^{-1})\left[\mathbf{Q} + \lambda^{-1}(\mathbf{Q}-\mathbf{I})\right]. \tag{3.8}$$

The polymer stress tensor, $\boldsymbol{\sigma}_p$, is related to the conformation tensor, $\mathbf{Q}$, via the relation,

$$\boldsymbol{\sigma}_p = G_0(\phi)(\mathbf{Q} - I), \tag{3.9}$$

where $G_0(\phi)$ is a relaxation modulus. The values of the parameters used in this study are as given in [6]. The ratio of the reptation to rouse parameter, $\tau_d/\tau_r = \theta =$

10, $\zeta = \phi^{3/2}$, the ratio of elastic to osmotic moduli, $E = G_0/(\chi^{-1}\phi^2) = 0.33$. The reptation time is given as $\tau_d(\phi) = \phi^\beta$ and the relaxation modulus as $G_0(\phi) = \phi^\alpha$, where α and β are taken as 2.25 and 1.5 respectively.

3.4 Geometry and Boundary Conditions

For this study, we consider flow between two infinite parallel plates with the upper plate moving with a constant velocity. The bottom plate is kept fixed. No-slip boundary and impermeability conditions are ascribed to the velocity at the walls. The upper plate is assigned a velocity of $H\,\mathrm{We}\tanh(at)$ where H is the channel width, We is the Weissenberg number and a is the ramp speed parameter assigned the values of 1 and 0.01 as in [6].

Zero normal gradient boundary conditions are assigned for pressure, p. The polymeric extra stresses are linearly extrapolated at the walls. An initial defect is imposed in the polymer concentration of the order of $\phi = 1 + \delta\cos(\pi k y/H)$. We choose the values of k to be 1 for the sake of comparing our results to those of [6].

3.5 Numerical Method

The Finite volume method (FVM) implemented on the open source software OpenFOAM is used to discretize the governing equations. The Rolie-Poly model is added to the viscoelastic solver and the momentum equations, Eq. (3.4) also included. The SIMPLE algorithm is used to for the pressure-velocity coupling in the solver. To solve the pressure equation, we use the preconditioned conjugate gradient (PCG) method. The velocity and volume fraction equations are solved via the Bi-Conjugate Gradient Stabilized (BICGSTAB) method. The preconditioner used is the simplified Diagonal-based Incomplete Cholesky (DIC) for pressure and

simplified Diagonal-based Incomplete LU (DILU) for velocity and ILUO for the volume fraction.

The summary steps for the iterative algorithm are given as;

1. The variables are initialized;
2. The stress equations are solved and used to compute $\mathbf{Q}$;
3. The momentum equations are solved for the intermediate velocity field;
4. The pressure equation is then solved and the under-relaxation applied;
5. Both pressure and velocity are corrected via the SIMPLE algorithm;
6. The volume fraction is obtained;
7. The solutions at the next time level, $t_{new} = t_{old} + \delta t$, are obtained and the processes is repeated from step 2 until either the predetermined final time is reached or certain predetermined conditions are met.

3.6 Code Validation

To validate the shear banding results, we use the Johnson-segalman and the Giesekus models and compare our results using those in the existing literature. The Johnson-Segalman model exhibits a monotonic or non-monotonic relationship between the shear rate and shear stress depending on the parameter ξ whereas the Giesekus model can exhibit either a monotonic or non-monotonic relationship depending on the values of the anisotropy parameter, α, and solvent viscosity, η_s.

The governing equations for the flow of a general incompressible viscoelastic fluid include the continuity equation;

$$\nabla \cdot \mathbf{v} = 0. \tag{3.10}$$

The momentum equations;

$$\rho\frac{D\mathbf{v}}{Dt} = -\nabla p + \nabla\cdot(2\eta_s\mathbf{D} + \boldsymbol{\sigma}_p), \tag{3.11}$$

and the constitutive models for the extra stress tensor $\boldsymbol{\sigma}_p$ which will be given variously in each of the following sections. The rate of deformation tensor, $\mathbf{D}$, is defined as,

$$\mathbf{D} = \frac{1}{2}[\nabla\mathbf{v} + (\nabla\mathbf{v})^T], \tag{3.12}$$

and the material derivative (operating on a quantity $*$) is defined in the usual notation as,

$$\frac{D*}{Dt} = \frac{\partial *}{\partial t} + \mathbf{v}\cdot\nabla * . \tag{3.13}$$

3.6.1 Johnson-Segalman Model

For Johnson-segalman fluids, the stress constitutive equation is given as

$$\boldsymbol{\sigma}_p + \lambda\overset{\square}{\boldsymbol{\sigma}}_p = 2\eta_p\,\mathbf{D}, \tag{3.14}$$

where

$$\overset{\square}{\boldsymbol{\sigma}}_p = \frac{\xi}{2}\left(\frac{D\boldsymbol{\sigma}_p}{Dt} + \boldsymbol{\sigma}_p\cdot(\nabla\mathbf{v})^T + \nabla\mathbf{v}\cdot\boldsymbol{\sigma}_p\right) + \left(1-\frac{\xi}{2}\right)\left(\frac{D\boldsymbol{\sigma}_p}{Dt} - \boldsymbol{\sigma}_p\cdot(\nabla\mathbf{v})^T - \nabla\mathbf{v}\cdot\boldsymbol{\sigma}_p\right). \tag{3.15}$$

In keeping with the validation literature, we consider plane shear flow of a Johnson-Segalman fluid in a rectangular geometry. The flow is between two infinite parallel plates located at $y = 0$ and $y = 1$. The upper plate moves with a constant velocity while the lower plate is fixed.

Also in keeping with the validation literature, we consider non-dimensional equations and track the flow dynamics via the two dimensionless parameters, the Reynolds' number and the Weissenberg number, respectively defined as,

$$\mathrm{Re} = \frac{\rho V^* H}{\eta}, \tag{3.16}$$

and

$$\mathrm{We} = \frac{\lambda V^*}{H}, \tag{3.17}$$

where H is a typical length scale and $\eta = \eta_P + \eta_S$ is the total fluid viscosity.

We simulate our flow in the OpenFOAM solver and we employ two stabilization techniques; the Discrete Elastic Viscous Stress Splitting (DEVSS) technique as well as the Log-Conformation Reformulation (LCR) methodology [42, 43] which appear as LogT on the graphs. We compare our results with those of [3] using the parameters values; Re = 1, We = 1, $\Delta t = 0.005$, $\eta_S = 0.05$, $\eta_P = 0.95$, and $\xi = 0.8$.

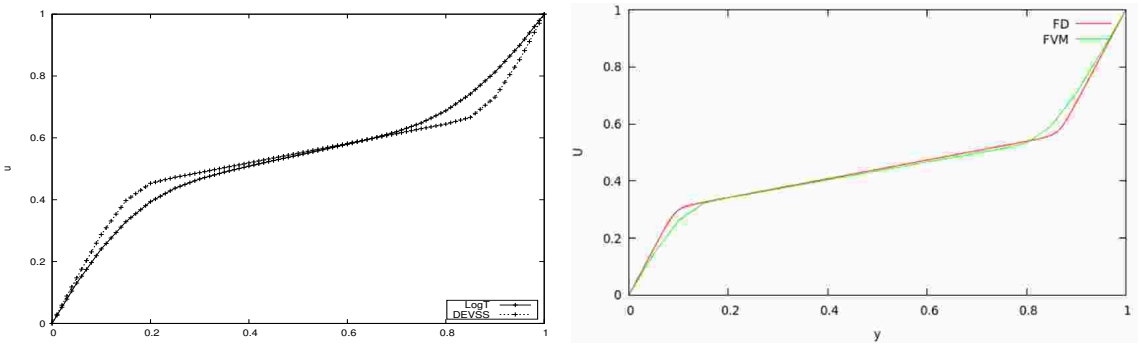

FIGURE 3.2: Velocity profile (v_x) for We = 2, $\eta_S = 0.05$, $\eta_P = 0.95$, $\xi = 0.8$, and Re = 1 for the Johnson-Segalman model (compared with reference [3] (RHS)).

The results are in qualitatively agreement. As also observed in [3], Fig. (3.2) shows that there is a rapid increase of velocity near the plates. The stress profiles, Figs. (3.3), (3.4) and (3.5), also agree favourably with those of [3] for the DEVSS method.

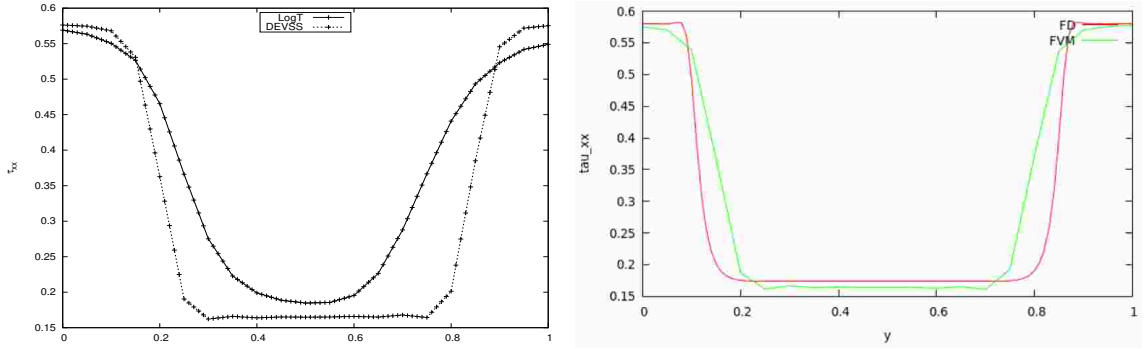

FIGURE 3.3: Normal stress profile ($\tau_{xx} = \sigma_{p_{xx}}$) for We = 2, $\eta_S = 0.05$, $\eta_P = 0.95$, $\xi = 0.8$, and Re = 1 for the Johnson-Segalman model (compared with reference [3] (RHS)).

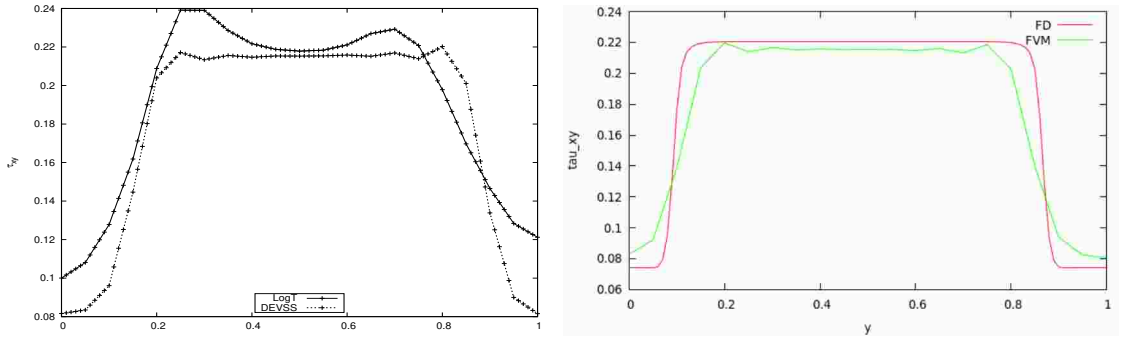

FIGURE 3.4: Shear stress profile ($\tau_{xy} = \sigma_{p_{xy}}$) for We = 2, $\eta_S = 0.05$, $\eta_P = 0.95$, $\xi = 0.8$, and Re = 1 for the Johnson-Segalman model (compared with reference [3] (RHS)).

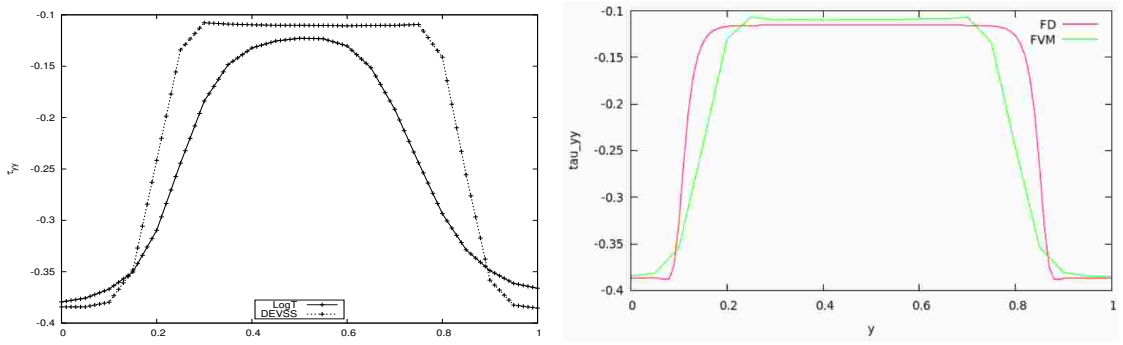

FIGURE 3.5: Normal stress profile ($\tau_{yy} = \sigma_{p_{yy}}$) for We = 2, $\eta_S = 0.05$, $\eta_P = 0.95$, $\xi = 0.8$, and Re = 1 for the Johnson-Segalman model (compared with reference [3] (RHS)).

To compare our results with the analytical solutions given in [4], the values of $\eta_S = 0.05$, We = 1, $\xi = 0.2$, Re = 0, and $V = 3$ are used and the graphs compared qualitatively.

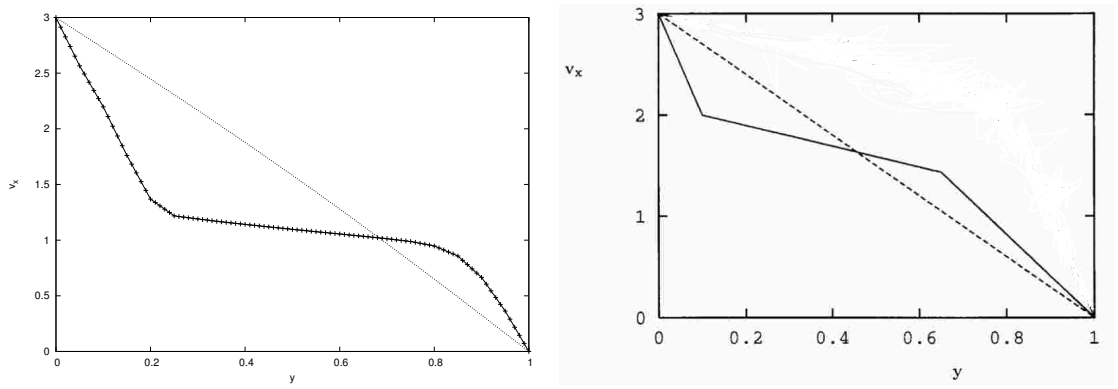

FIGURE 3.6: Velocity profile for We = 1, $\eta_S = 0.05$, $\xi = 0.2$, We = 0, and $V = 3$ (compared with the analytic solution from reference [4] (RHS)). The dashed line is the final steady state.

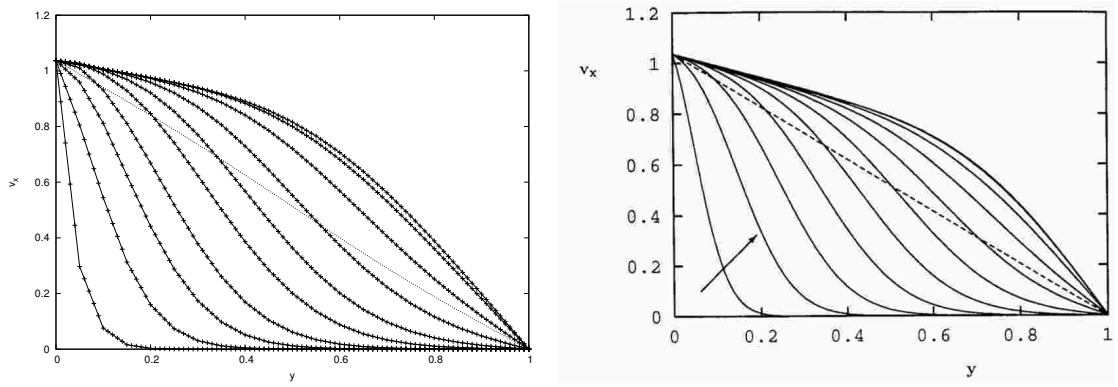

FIGURE 3.7: Evolution of v_x during the inception of simple shear flow for times up to $t = 1.05$ using, We = 1, $\eta_S = 0.05$, $\xi = 0.2$, Re = 1, and $V = 1.037$ (compared with the analytic solution from reference [4] (RHS)). The dashed line is the final steady state.

3.6.2 Giesekus Model

The constitutive stress equation for the Giesekus model in terms of the conformation tensor, $\mathbf{c}$, is given as in [103];

$$\frac{d\mathbf{c}}{dt} = -\mathbf{v}\cdot\nabla\mathbf{c} + \mathbf{c}\cdot\nabla\mathbf{v} + (\nabla\mathbf{v})^T\cdot\mathbf{c} - \frac{1}{\lambda}\left[(1-\alpha)\mathbf{I} + \alpha\xi\mathbf{c}\right]\cdot(\mathbf{c}-\xi\mathbf{I}) + D\nabla^2\mathbf{c}. \quad (3.18)$$

The equation for the deviatoric stress, $\mathbf{T} = 2\eta_s\mathbf{D} + \boldsymbol{\sigma}_p$, is,

$$\mathbf{T} = G_0 \left(\frac{K}{k_B T} \mathbf{c} - \mathbf{I} \right) + \eta_s \left[\nabla \mathbf{v} + (\nabla \mathbf{v})^T \right]. \tag{3.19}$$

In keeping with the validation literature [5, 103], we employ parameters values for the Giesekus models that were obtained using a small amplitude oscillatory shear data. Such data is used to determine the effective relaxation time and the anisotropy factor estimated by fitting the Giesekus model to the steady-state shear stress and first normal stress difference plotted as a function of the shear rate. This procedure is outlined in detail in [103].

Comparative validation of our results against those of [5] will therefore be based on the parameters values given in Table 3.1.

TABLE 3.1: Giesekus parameters

Parameter	Symbol	value
Solvent viscosity	η_S	0.099Pa
Plateau Modulus	G_0	150Pa
Relaxation time	λ	0.013s
Anisotropy factor	α	0.91
Viscoelastic parameter	ξ	1
Diffusion coefficient	D	$5m^2/s$

The viscoelastic parameter, ξ in Table 3.1 corresponds to the fraction,

$$\xi = \frac{K}{k_B T}.$$

Simulated results are for the Couette flow for both anti-symmetric and symmetric cases. In the anti-symmetric case, the upper plate moves with a velocity of $1m/s$ whereas the lower plate is fixed while in the symmetric case, the upper and lower plates respectively move with a velocity of $1m/s$ and $-1m/s$, essentially moving in opposite directions at the same velocity.

The velocity profiles are obtained at different times and qualitatively compared with those of [5]. The time taken to obtain similar results as in [5] was double the time they took and with a smaller time step of $\triangle T = 0.001$. Thus, the time given in our graphs is scaled by 1/2

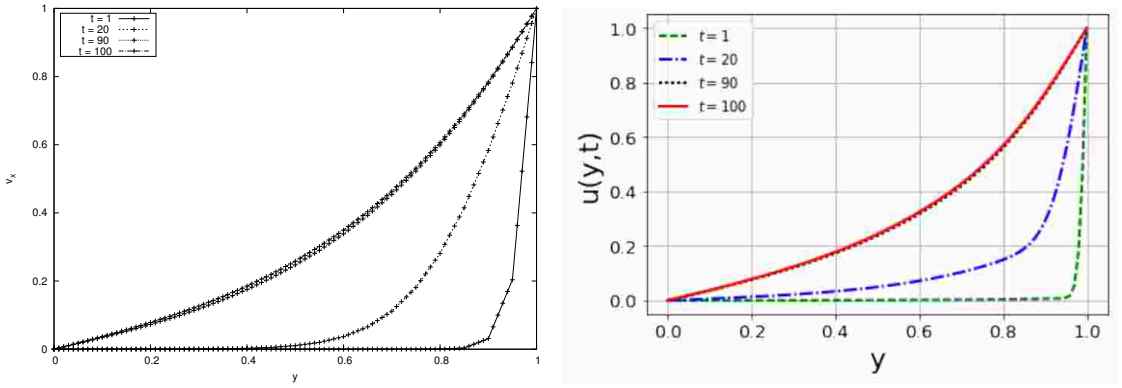

FIGURE 3.8: Velocity profile v_x for the anti-symmetric case (compared with reference [5] (RHS)).

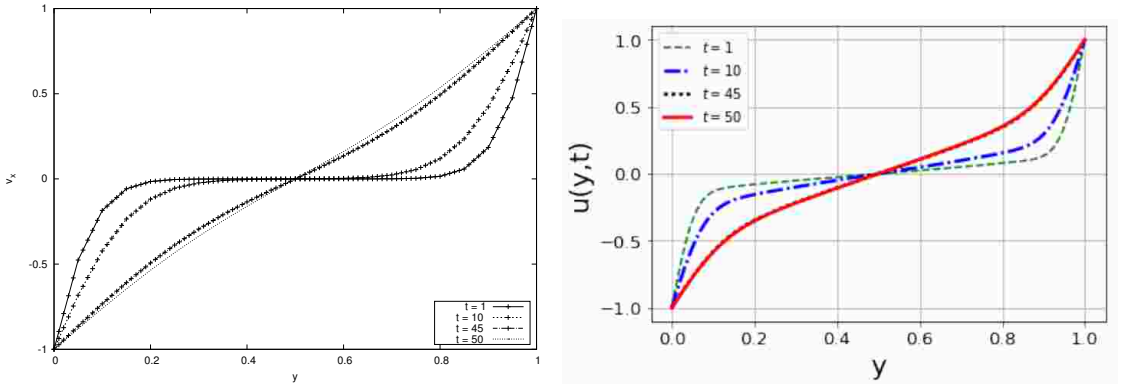

FIGURE 3.9: Velocity profile v_x for the symmetric case (compared with reference [5] (RHS)).

3.7 Results for the Rolie-Poly Model

Having validated our results with existing literature for the Johnson-Segalman and Giesekus models, we now proceed with the main aim to simulate the two-fluid model for the Rolie-Poly constitutive equations. The results are qualitatively compared with [6] for $k = 1$. Also following [6, 7], we employ non-dimensional equations in the simulations.

Figures (3.10) and (3.11) show that the DEVSS method again better simulates the results in the existing literature for concentration, ϕ, as compared to the LCR method. There is however no signification difference in terms of the velocity profile

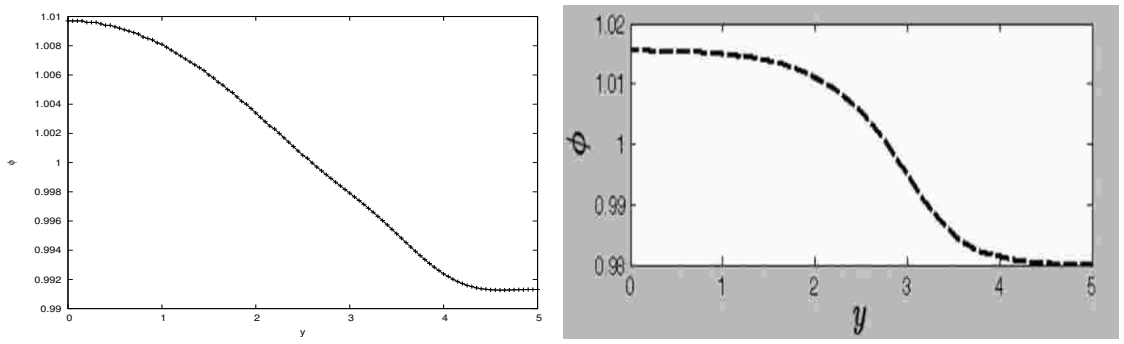

FIGURE 3.10: Concentration profile ϕ for $k = 1$ using the LCR method (LHS) (compared with references [6] (RHS)).

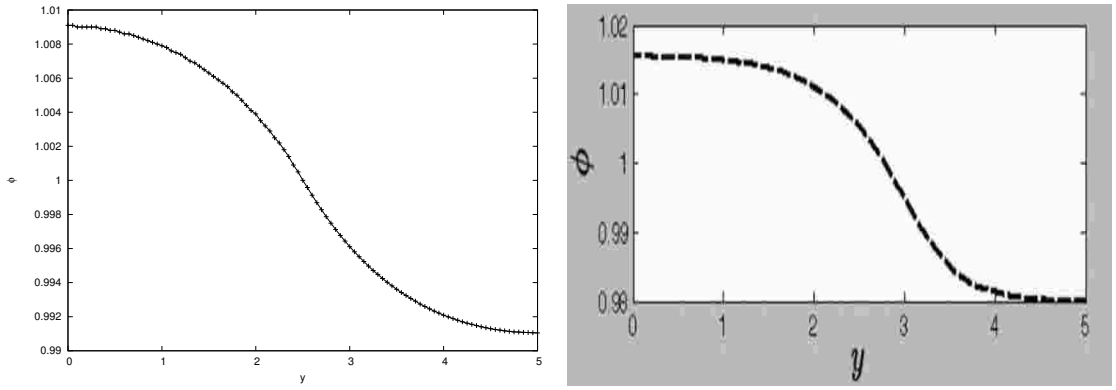

FIGURE 3.11: Concentration profile ϕ for $k = 1$ using the DEVSS method (LHS) (compared with references [6] (RHS)).

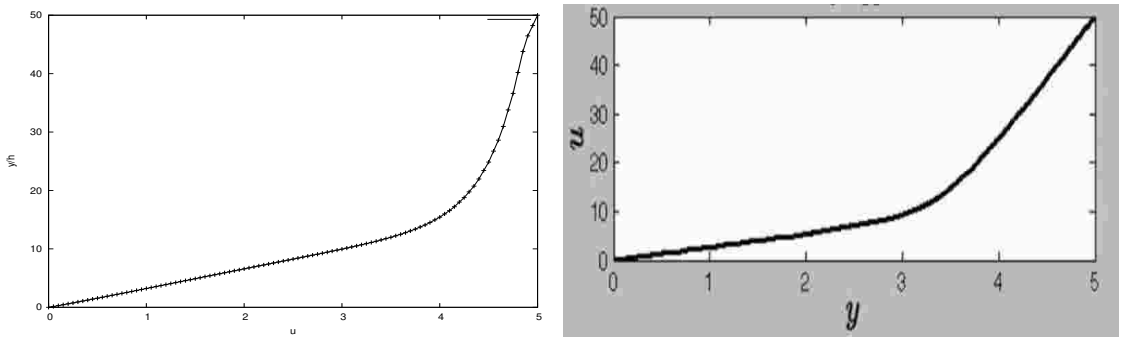

FIGURE 3.12: Velocity profile for $k = 1$ using the LCR method (compared with references [6] (RHS)).

simulations between the DEVSS and LCR methods as seen in Figs. (3.12) and (3.13).

Our simulated results are also compared to those of [7], see Figs. (3.14) and (3.15) and they show good qualitative agreement. The DEVSS and LCR simulations show no significant difference in the simulated results. Due to the restrictively high

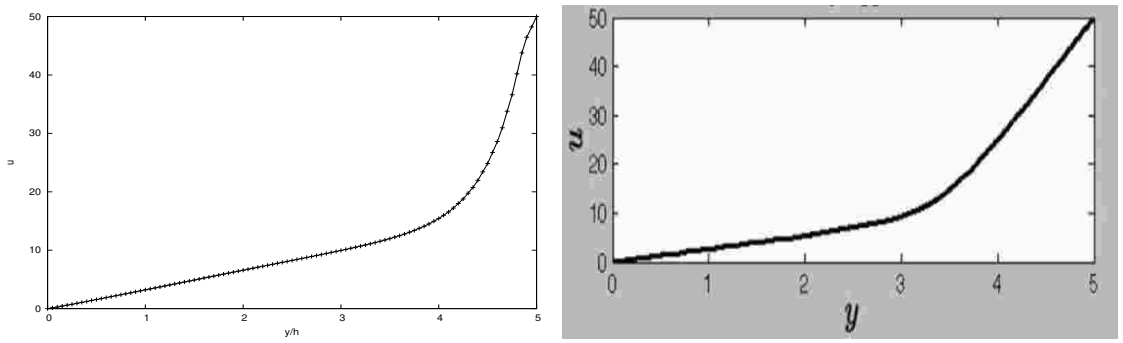

FIGURE 3.13: Velocity profile for $k = 1$ using the DEVSS method (compared with references [6] (RHS)).

computational costs involved, we were unable to resolve the simulations when using the small values of H as used in [6, 7]. This could explain the slight quantitative differences between the results.

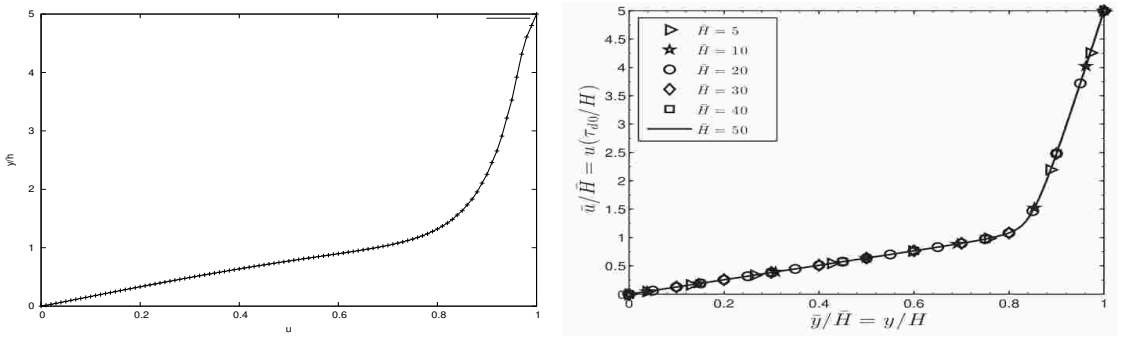

FIGURE 3.14: Velocity profile for $k = 1$ using the DEVSS method (compared with references [7] (RHS)).

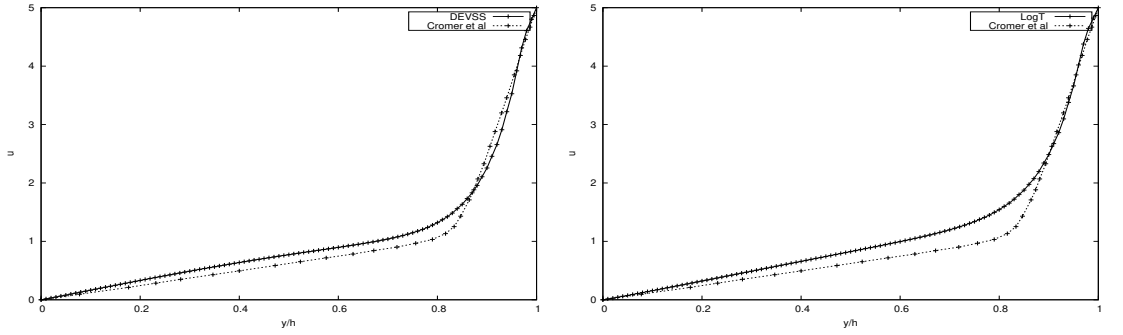

FIGURE 3.15: Velocity profile for $k = 1$ using the DEVSS method (LHS) and the LCR method (RHS) (compared with references [7]).

3.8 Discussion and Conclusion

In this work, we develop a numerical solver based on the finite volume method to simulate complex (shear banded) dynamics of viscoelastic fluids in shear flow. The solver is implemented on the open source OpenFOAM platform and is tested using various viscoelastic constitutive models including the non-homogeneous Rolie-Poly constitutive model. Comparison of our simulated results against those in the existing literature, [3] and [5], for the Johnson-Segalman and Giesekus models respectively gives good agreement. There is also good agreement between our simulated results for the Rolie-Poly two-fluid model and those of [6, 7].

Due to the restrictively high computational costs involved, we were unable to resolve the simulations when using the small values of H as used in [6, 7]. This could explain the slight quantitative differences between the results.

Acknowledgements

We would like to acknowledge support received from the Organization for Women in Science for the Developing World (OWSD) and the Swedish International Development Cooperation Agency (SIDA). The resources from the Centrer for High Performance Computing (CHPC) in South Africa are gratefully acknowledged.

Chapter 4

Conclusion

The complex flows of complex fluids are of importance due to their applications in industry. The focus of this work has been to develop an efficient computational platform to be used in the open source software OpenFOAM to simulate complex fluids that are governed by the Rolie-Poly constitutive equation.

Validation of this solver is done by using lid-driven cavity and planar 4:1 geometry. A regularized lid-velocity is used to mitigate corner singularities.

The High Weissenberg Number Problem (HWNP) is a challenge in simulation of flows in complex geometries. To address this issue, we use two stabilizing techniques, the Log-Conformation Reformulation (LCR) and the Discrete Elastic Viscous Stress Splitting (DEVSS) method.

Since, a lot of research has been done on the Oldroyd-B both for lid-driven cavity and the planar 4:1, we use existing literature to compare with our results. It is important to note that the Oldroyd-B equation can be recovered as rouse time $\lambda_R -> \infty$. We therefore recover the Oldroyd-B constitutive equation in our solver and compare the results with existing literature. Our simulated numerical results are in good agreement with existing literature. As indicated in literature, the LCR method yields better results for high Deborah numbers than the DEVSS method. Furthermore, we compare our developed solver with one that was, in the course of this study, included in the RheoTool solver. The predicted flow behaviour are similar for both solvers, however, the stress values differ by a factor of 100. The

second part of the study focuses on using the developed Rolie-Poly solver for computational investigations of the shear-banding. Shear banding phenomena has been observed in complex fluids that have a non-monotonic shear rate-stress relationship. For monotonic equations, instabilities are triggered by using a two-fluid model which is obtained by coupling the concentration to stress.

Johnson-Segalman and Giesekus constitutive models are simulated and the results obtained are compared with existing results. Our results are in good agreement. We couple stress and concentration equations for the two fluid model. With this coupling, we have been able to reproduce shear-banding using the Rolie-Poly constitutive equation solver added to OpenFOAM. The simulated results for the concentration when compared with existing literature show good agreement when using DEVSS method. However, there is a slight difference when using the Log-conformation reformulation. Our velocity profile results show good agreement when compared with existing literature. Despite the LCR being proven a better method to mitigate the HWNP, DEVSS method yielded better results for the concentration values and velocity profiles. Thus, more work needs to be carried out to resolve this discrepancy.

Appendix A

Shear Banding Governing Equations

For the two-fluid model, two sets of equations for the polymer and the solvent are considered. The volume fraction of the polymer and solvent are denoted as ϕ_p and ϕ_s respectively, their sum being 1.
The continuity equation is given as:

$$\nabla \cdot \mathbf{v} = 0 \tag{A.1}$$

where $\mathbf{v} = \phi_s \mathbf{v}_s + \phi_p \mathbf{v}_p$. The conservation of mass equations for the solvent and polymer are given as:

$$\frac{D_s \phi_s}{D_s t} = \frac{\partial \phi_s}{\partial t} + \nabla \cdot (\phi_s \mathbf{v}_s) \tag{A.2}$$

$$\frac{D_p \phi_p}{D_p t} = \frac{\partial \phi_p}{\partial t} + \nabla \cdot (\phi_p \mathbf{v}_p) \tag{A.3}$$

The two conservation equations are then linked together using friction whose form is given as $\zeta (\mathbf{v}_s - \mathbf{v}_p)$ with ζ as the friction coefficient. Consequently, rewriting using the friction linear form, the Equations A.2 and A.3 become:

$$\frac{D_s \rho_s \phi_s \mathbf{v}_s}{Dt} = \eta_s \nabla^2 \mathbf{v}_s - \nabla p - \zeta (\mathbf{v}_s - \mathbf{v}_p) \tag{A.4}$$

$$\frac{D_p \rho_p \phi_p \mathbf{v}_p}{Dt} = \nabla \cdot \sigma_p - \nabla \pi_0 + \zeta(\mathbf{v}_s - \mathbf{v}_p) \tag{A.5}$$

where π_0 is the Osmotic pressure given as:

$$\pi_0 = \chi_0^{-1} \left[\frac{1}{2}\phi^2 - \xi\phi\nabla^2\phi + \frac{1}{2}\left(\phi \frac{\partial \xi^2}{\partial \phi} - \xi^2 \right) |\nabla\phi|^2 \right] \tag{A.6}$$

For Equation A.4, the left hand side is set to zero since the polymer inertia is negligible because $\phi_p \leqslant 0$ due to the assumption that the polymer is dilute yet entangled. On that account, the density and velocity of the solvent correspond to the density, ρ and volume-averaged velocity, $\mathbf{v}$. Consequently, the entire inertia in the system is disregarded. Therefore, the conservation equations are:

$$0 = \eta_s \nabla^2 \mathbf{v} - \nabla p - \zeta \left(\mathbf{v} - \mathbf{v}_p \right) \tag{A.7}$$

$$0 = \nabla \cdot \sigma_p - \nabla \pi_0 + \zeta(\mathbf{v} - \mathbf{v}_p) \tag{A.8}$$

The comprehensive momentum for the fluid, obtained by summing up the two equations A.7 and A.8 is given as:

$$\eta_s \nabla^2 \mathbf{v} + \nabla \cdot \sigma_p - (p + \pi_0) = 0 \tag{A.9}$$

The polymer mass balance is given as:

$$\frac{\partial \phi}{\partial t} + \nabla \cdot (\phi \mathbf{v}_p) = 0 \tag{A.10}$$

Using the polymer velocity, $\mathbf{v}_p = \mathbf{v} + \left(\frac{1}{\zeta}\right)(\nabla \cdot \sigma_p - \nabla \pi_0)$, that is got from Equation A.8, the polymer mass balance becomes:

$$\frac{\partial \phi}{\partial t} = -\mathbf{v} \cdot \nabla \phi + \nabla \cdot \left[\frac{\phi}{\zeta} \left(\nabla \pi_0 - \nabla \cdot \sigma_p \right) \right] \tag{A.11}$$

The stress constitutive models given as:

$$\frac{\partial \mathbf{Q}}{\partial t} + \mathbf{v} \cdot \nabla \mathbf{Q} - \mathbf{Q} \cdot \nabla \mathbf{v} - \nabla \mathbf{u})^T \cdot \mathbf{Q}$$

$$+\left\{\frac{1}{\zeta}\left[\nabla\cdot\sigma_p-\nabla\pi_0\right]\cdot\nabla\mathbf{Q}-\left(\nabla\frac{1}{\zeta}\left[\nabla\cdot\sigma_p-\nabla\pi_0\right]\right)^T\cdot\mathbf{Q}-\mathbf{Q}\cdot\nabla\frac{1}{\zeta}\left[\nabla\cdot\sigma_p-\nabla\pi_0\right]\right\}$$

$$=-\tau_d^{-1}(\phi)(\mathbf{Q}-\mathbf{I})-2\tau_R^{-1}(1-\lambda^{-1})\left[\mathbf{Q}+\beta\lambda^{2\delta}(\mathbf{Q}-\mathbf{I})\right] \tag{A.12}$$

Which, using the polymer velocity, can be rewritten as: The stress constitutive models given as:

$$\frac{\partial\mathbf{Q}}{\partial t}+\mathbf{v}_p\cdot\nabla\mathbf{Q}-\mathbf{Q}\cdot\nabla\mathbf{v}_p-\nabla\mathbf{v}_p)^T\cdot\mathbf{Q}=$$

$$-\tau_d^{-1}(\phi)(\mathbf{Q}-\mathbf{I})-2\tau_R^{-1}(1-\lambda^{-1})\left[\mathbf{Q}+\beta\lambda^{2\delta}(\mathbf{Q}-\mathbf{I})\right] \tag{A.13}$$

The polymer stress is given as

$$\sigma_p=G(\phi)(\mathbf{Q}-\mathbf{I}) \tag{A.14}$$

where $G(\phi)$is the plateau modulus.

The Equations A.1, A.9, A.11, A.6, A.13 and A.14 are non-dimensionalised to obtain the final set of equations as:

$$\bar{\nabla}\cdot\bar{\mathbf{v}}=0 \tag{A.15}$$

$$\bar{\omega}\bar{\nabla}^2\bar{\mathbf{v}}+\bar{\nabla}\cdot\bar{\sigma}_p-(\bar{p}+\bar{\pi}_0)=0 \tag{A.16}$$

$$\frac{\partial\bar{\phi}}{\partial\bar{t}}=-\bar{\mathbf{v}}\cdot\bar{\nabla}\bar{\phi}+\bar{\nabla}\cdot\left[\frac{\bar{\phi}}{\bar{\zeta}}\left(\nabla\bar{\pi}_0-E\bar{\nabla}\cdot\bar{\sigma}_p\right)\right] \tag{A.17}$$

$$\bar{\pi}_0=\left[\frac{1}{2}\bar{\phi}^2-\bar{\xi}^2\bar{\phi}\bar{\nabla}^2\bar{\phi}+\frac{1}{2}\left(\bar{\phi}\frac{\partial\bar{\xi}^2}{\partial\bar{\phi}}-\bar{\xi}^2\right)|\bar{\nabla}\bar{\phi}|^2\right] \tag{A.18}$$

$$\frac{\partial\mathbf{Q}}{\partial\bar{t}}+\bar{\mathbf{v}}_p\cdot\bar{\nabla}\mathbf{Q}-\mathbf{Q}\cdot\bar{\nabla}\bar{\mathbf{v}}_p-\bar{\nabla}\bar{\mathbf{v}}_p)^T\cdot\mathbf{Q}=$$

$$-\bar{\tau}_d^{-1}(\bar{\phi})(\mathbf{Q}-\mathbf{I})-2\theta(1-\lambda^{-1})\left[\mathbf{Q}+(\mathbf{Q}-\mathbf{I})\right] \tag{A.19}$$

$$\bar{\sigma}_p=\bar{\phi}^{\alpha}(\mathbf{Q}-\mathbf{I}) \tag{A.20}$$

To compare, values from [6, 7] are used and given as $\tau_d/\tau_r=\theta=10$, $\zeta=\phi^{3/2}$, $E=G_0/(\chi^{-1}{\phi_0}^2=0.33$, $\tau_d(\phi)=\phi^{\beta}$ and the plateau modulus as $G_0(\phi)=\phi^{\alpha}$ where α and β are 2.25 and 1.5 respectively.

Bibliography

[1] H K Versteeg and W Malalasekera. *An Introduction to Computational Fluid Dynamics*. Pearson Education Limited, 2nd edition edition, 2007.

[2] R. Comminal, J. Spangenberg, and J.H. Hattel. Robust simulation of viscoelastic flows at high weissenberg numbers with the steamfunction/log-conformation formulation. *Journal of Non-Newtonian Fluid Mechanics*, 223:37–61, 2015.

[3] Faniry Nadia Zazaravaka Rahantamialisoa. Complex fluid dynamical computations via the finite volume method, 2018.

[4] Georgios C. Georgiou and Dimitris Vlassopoulos. On the stability of the simple shear flow of a johnson-segalman fluid. *Journal of Non-Newtonian Fluid Mechanics*, 75:77–97, 1998.

[5] David Kibe Muchiri. Modelling of shear banding in viscoelastic fluids via the giesekus model (scholarly project), 2018.

[6] Michael Cromer, Michael C. Villet, Glenn H.Fredrickson, and L. Gary Leal. Shear banding in polymer solutions. *Physics Of Fluids*, 25(5):1–7, 2013.

[7] Michael Cromer, Glenn H.Fredrickson, and L. Gary Leal. A study of shear banding in polymer solutions. *Physics Of Fluids*, 26(6):1–17, 2014.

[8] Fridtjov Irgens. *Rheology and Non-Newtonian Fluids*. Springer Cham Heidelberg, 2014.

[9] H.A. Barnes, J.F.Hutton, and K.Walters F.R.S. *An introduction to rheology*. Elsevier Science Publishers B.V, first edition edition, 1989.

[10] Non-newtonian fluids:an introduction. http://www.physics.iitm.ac.in/ compflu/Lectnotes/chhabra.pdf.

[11] H. Yamaguchi. *Engineering Fluid Mechanics*. Springer, 2008.

[12] R. Byron Bird, Robert C. Armstrong, and Ole Hassager. *Dynamics of polymeric liquids, volume 1: Fluid mechanics*. Wiley-Inter science Publication : John Wiley and Sons, 2nd edition edition, 1987.

[13] G. Astarita and G. Marrucci. *Principles of non-Newtonian fluid mechanics*. McGraw-Hill, 1974.

[14] Michel O. Deville and Thomas B. Gatski. *Mathematical Modeling for Complex Fluids and Flow*. Springer-Verlag, 2012.

[15] Daniel Bonn and Morton M. Denn. Yield stress fluids slowly yield to analysis. *Science*, 324:1401–1402, 2009.

[16] E.B.Bagley and F.R.Dintzis. Shear thickening and flow induced structures in foods and biopolymer systems. *Rheology Series*, 8:63–86, 1999.

[17] Nhan Phan-Thien. *Understanding Viscoelasticity: Basics of Rheology*. Springer-Verlag, 1st edition, 2002.

[18] R. P. Chhabra and J.F. Richardson. *Non-Newtonian Flow and Applied Rheology: Engineering Applications*. Butterworth Heinemann Publication, Oxford, 2nd edition, 2008.

[19] Michael Renardy. *Mathematical Analysis of Viscoelastic Flows*. Society for Industrial and Applied Mathematics, 2000.

[20] P.J. Dotson R.B. Bird and N.L. Johnson. Polymer solution rheology base on a finitely extensible bead-spring chain model. *Journal of Non-Newtonian*, 7:218–286, 1980.

[21] C.F. Chan Man Fong and D. De Kee. Constitutive equations from transient network theory. *Advances in the Flow and Rheology of Non-Newtonian Fluids*, 8:385– 427, 1999.

[22] R. Byron Bird and John M. Wiest. Constitutive equations for polymeric liquids. *Annual reviews of Fluid Mechanics*, 27:169–193, 1995.

[23] Shizuo Hayashi. A network theory of nonlinear viscoelasticity. *Polymer Journal*, 10:59–67, 1978.

[24] Thien N. P and Tanner R. I. A new constitutive equation derived from network theory. *Journal of Non-Newtonian Fluid Mechanics*, 2(4):353–365, 1977.

[25] M. Doi and S. F. Edwards. *The Theory of Polymer Dynamics*. Clarendon Press, Oxford University Press,, 1986.

[26] Alexei E. Likhtman and Richard S. Graham. Simple constitutive equation for linear polymer melts derived from molecular theory: Rolie-poly equation. *Journal of Non-Newtonian Fluid Mechanics*, 114:1–12, 2003.

[27] J. Clerk Maxwell. On the dynamical theory of gases. *Philosophical Transactions of the Royal Society of London*, 157:49–88, 1867.

[28] T. Bodnár, M. Pires, and J. Janela. Blood flow simulation using traceless variant of johnson-segalman viscoelastic model. *Mathematical Modelling of Natural Phenomena*, 9(6):117–141, 2014.

[29] Randal J. Leveque. *Finite volume method for hyperbolic problems*. Cambridge university press, 2002.

[30] Robert Eymard, Thierry Gallouët, and Raphaèle Herbin. *The finite volume method Handbook of Numerical Analysis*, volume VII. Elsevier, 2000.

[31] Robert Eymard and Thierry Gallouët and Raphaèle Herbin. Finite volume method, 2010.

[32] R. I. Issa. Solution of the implicitly discretized fluid flow equations by operator-splitting. *Journal of Computational Physics*, 62:40–65, 1986.

[33] Cfd direct. https://cfd.direct/openfoam/about/.

[34] Goong Chen, Qingang Xiong, Philip J. Morris, Eric G. Paterson, Alexey Sergeev, and Yi-Ching Wang. Openfoam for computational fluid dynamics. *Notices of the American Mathematical Society*, 61(4):354–363, 2014.

[35] Openfoam. https://cfd.direct/openfoam/user-guide/v6-introduction.

[36] Openfoam v5 user guide: 4.1 file structure of openfoam cases. https://cfd.direct/openfoam/user-guide/v5-case-file-structure.

[37] Openfoam. https://en.wikipedia.org/wiki/OpenFOAM.

[38] J.L. Favero, A.R. Secchi, N.M. Cardozo, and H. Jasak. Viscoelastic flow simulation: Development of a methodology of analysis using the software openfoam and differential constitutive equations. *Computer Aided Chemical Engineering*, 27:915–920, 2009.

[39] J.L.Favero, A.R.Secchi, N.S.M.Cardozo, and H.Jasak. Viscoelastic flow analysis using the software openfoam and differential constitutive equations. *Journal of Non-Newtonian Fluid Mechanics*, 23-24:1625–1636, 2010.

[40] R. Keunings. On the high weissenberg number problem. *Journal of Non-Newtonian Fluid Mechanics*, 20:209–226, 1986.

[41] Amith Balasubramanya. Cfd with opensource software : Viscoelasticity and constitutive relation. http://www.tfd.chalmers.se/ hani/kurser/OS˙CFD˙2015/Amith/Viscoelasticity˙Final.pdf.

[42] R. Fattal and R. Kupferman. Time-dependent simulation of visocelastic flows at high weissenberg number using the log-conformation representation. *Journal of Non-Newtonian Fluid Mechanics*, 126:23–37, 2005.

[43] R. Fattal and R. Kupferman. Constitutive laws for the matrix-logarithm of the conformation tenser. *Journal of Non-Newtonian Fluid Mechanics*, 123:281–285, 2004.

[44] Jade G. Abuga and Tiri Chinyoka. Benchmark solutions of the stabilized computations of flows of fluids governed by the rolie-poly constitutive model. Currently under review, 2018.

[45] P.N. Shankar and M.D. Deshpande. Fluid mechanics in the driven cavity. *Annual Review Fluid Mechanics*, 32:93–136, 2000.

[46] A.M. Grillet, B. Yang, B. Khomami, and E.S.G. Shaqfeh. Modeling of viscoelastic lid driven cavity flow using the finite element simulations. *Journal of Non-Newtonian Fluid Mechanic*, 88:99–131, 1999.

[47] R.G. Sousa, R.J. Poole, A.M. Afonso, F.T. Pinho, P.J. Oliveira, A. Morozov, and M.A. Alves. Lid-driven cavity flow of viscoelastic fluids. *Journal of Non-Newtonian Fluid Mechanics*, 234:129–138, 2016.

[48] F. Habla, H. Marschall, O. Hinrichsen, L. Dietsche, H. Jasak, and J.L. Favero. Numerical simulation of viscoelastic two-phase flows using OpenFOAM. *Chemical Engineering Science*, 66(22):5487–5496, 2011.

[49] M. Fortin, R. Guenette, and R. Pierre. Numerical analysis of the modified evss method. *Computer methods in Applied Mehcanics and Engineering*, 143(1-2):79–95, 1997.

[50] D. Rajagopalan, R.C. Armstrong, and R.A. Brown. Finite element methods for calculation of steafy viscoealstic flow using constitutive equation with a newtonian viscosity. *Journal of Non-Newtonian Fluid Mechanics*, 36:159–192, 1990.

[51] M. Fortin and A. Fortin. A new approach for the fem silumation of viscoelastic flows. *Journal of Non-Newtonian Fluid Mechanics*, 32:295–310, 1989.

[52] J.M. Marchal and M.J. Crochet. A new mixed finite element for calculating viscoelastic flows. *Journal of Non-Newtonian Fluid Mechanics*, 26:77–114, 1987.

[53] A. Afonso, P.J. Oliveira, F.T. Pinho, and M.A. Alves. The log-conformation tensor approach in the finite-volume method framework. *Journal of Non-Newtonian Fluid Mechanics*, 157(1-2):55–65, 2009.

[54] F. Habla, M.W. Tan, J. Hasslberger, and O. Hinrichsen. Numerical simulation of the viscoelastic flow in a three-dimensional lid-driven cavity using the log-conformation reformulation in openfoam. *Journal of Non-Newtonian Fluid Mechanics*, 212:47–62, 2014.

[55] T.W. Pan and J. Hao. Numerical simulation of a lid-driven cavity viscoelastic flow at high weissenberg numbers. *C. R. Acad. Sci. Paris, Ser. I*, 344:283–286, 2007.

[56] Raphaël Comminal, Jesper H. Hattel, Manuel A. Alves, and Jon Spangenberg. Vortex behavior of the oldroyd-b fluid in the 4-1 planar contraction simulated with the streamfunction-log-conformation formulation. *Journal of Non-Newtonian Fluid Mechanics*, 237:1–15, 2016.

[57] T.W. Pan, J. Hao, and R. Glowinski. On the simulation of time-dependent cavity flow of an oldroyd-b fluid. *International journal for numerical methods in fluids*, 60:791–808, 2009.

[58] L.F.L.R. Silva and P.L.C. Lage. Development and implementation of a polydispersed multiphase flow model in OpenFOAM. *Computers and Chemical Engineering*, 35(12):2653–2666, 2011.

[59] J.L. Favero. Viscoelastic flow simulation in openfoam :presentation of the viscoelasticfluidfoam solver. Technical report, Universidade Federal do Rio Grande do Sul - Department of Chemical Engineering, 2009.

[60] J.P. Van Doormal and G.D. Raithby. Enhancements of the simple method for predicting incompressible fluid flows. *Numerical Heat transfer*, 7:147–163, 1984.

[61] D.S. Jang, R. Jetli, and S. Acharya. Comparison of the piso, simpler and simplec algorithms for the treatment of the pressure-velocity coupling in steady flow problems. *Numerical Heat Transfer*, 10:209–228, 1986.

[62] M.A.Alves, P.J.Oliveira, and F.T.Pinho. A convergent and universally bounded interpolation scheme for the treatment of advection. *International Journal for Numerical methods in fluids*, 41:47 –75, 2003.

[63] T. Chinyoka. Viscoelastic effects in double-pipe single-pass counterflow heat exchangers. *International Journal for Numerical Methods in Fluids*, 59(6):677 – 690, 2009.

[64] T. Chinyoka. Modeling of cross-flow heat exchangers with viscoelastic fluids. *Nonlinear Analysis: Real World Applications*, 10(6):3353 – 3359, 2009.

[65] T. Chinyoka. Two-dimensional flow of chemically reactive viscoelastic fluids with or without the influence of thermal convection. *Communications in Nonlinear Science and Numerical Simulation*, 16(3):1387 – 1395, 2011.

[66] F. Pimenta and M. Alves. Stabilization of an open-source finite volume solver for viscoelastic fluid flows. *Journal of Non-Newtonian Fluid Mechanics*, 239:85–104, 2017.

[67] L.M. Quinzani, R.C. Armstrong, and R.A. Brown. Birefringence and laser-doppler velocimetry (ldv) studies of viscoelastic flow through a planar contraction. *Journal of Non-Newtonian Fluid Mechanics*, 52:1–36, 1994.

[68] A. M. AFonso, P.J.Oliveira, F.T.Pinho, and M. A. Alves. Dynamics of high-deborah-number entry flows: a numerical study. *Journal of Fluid Mechanics*, 677:272–304, 2011.

[69] Rheotool : https://github.com/fppimenta/rheotool.

[70] Qingsheng Liu, Jie Ouyang, Chuntao Jiang, Xin Zhuang, and Wuming Li. Finite volume simulations of behavior for polystyrene in a cross-slot flow based on rolie-poly model. *Rheological Acta*, 55(2):137–154, 2016.

[71] Jade G. Abuga and Tiri Chinyoka. Shear banding of flows of fluids governed by the rolie-poly two-fluid model using openfoam. Submitted, 2018.

[72] Benjamín Marcos Marín-Santibá nez, José Pérez-González, Lourdes de Vargas, Jean Paul Decruppe, and Guadalupe Huelsz. Visualization of shear banding and entry poiseuille flow oscillations in a micellar aqueous solution. *Journal of Non-Newtonian Fluid Mechanics*, 157:117–125, 2009.

[73] J.P. Garcià-Sandoval, O. Manero, F. Bautista, and J.E. Puig. Inhomogeneous flows and shear banding formation in micellar solutions: Predictions of the bmp model. *Journal of Non-Newtonian Fluid Mechanics*, 179 -180:43–54, 2012.

[74] Youngri Kim, Abdulrazaq Adams, William H. Hartt, Ronald G. Larson, and Michael J. Solomon. Transient, near-wall shear-band dynamics in channel flow of wormlike micelle solutions. *Journal of Non-Newtonian Fluid Mechanics*, 232:77–87, 2016.

[75] Alexandre Kabla and Georges Debrgeas. Local stress relaxation and shear banding in a dry foam under shear. *Physical Review letters*, 90(25):1–4, 2003.

[76] Daniel M. Mueth, Georges F. Debregeas, Greg S. Karczmar, Peter J. Eng, Sidney R. Nagel, and Heinrich M. Jaeger. Signatures of granular microstructure in dense shear flows. *Letters to nature*, 406:385 – 388, 2000.

[77] William M. Holmes, Paul T. Callaghan, Dimitris Vlassopoulos, and Jacques Roovers. Shear banding phenomena in ultrasoft colloidal glasses. *Journal of Rheology*, 48:1085–1102, 2004.

[78] Joris Billen, Mark Wilson, and Arlette R.C. Baljon. Shear banding in simulated telechelic polymers. *Chemical Physic*, 446:7–12, 2015.

[79] L. Hilliou and D. Vlassopoulos. Time-periodic structures and instabilities in shear- thickening polymer solutions. *Ind. Eng. Chem. Res.*, 25(41):6246–6255, 2002.

[80] Yuye Fang, Guanglin Wang, Nan Tian, Xiao Wang, Xiangyang Zhu, Panpan Lin, Guanglei Ma, and Liangbin Li. Shear inhomogeneity in poly(ethylene oxide) melts. *Journal of Rheology*, 55:939 –949, 2011.

[81] Thibaut Divoux, Marc A. Fardin, Sebastien Manneville, and Sandra Lerouge. Shear banding of complex fluids. *Annual Reviews of Fluid Mechanics*, 48:81–103, 2016.

[82] Benjamín Marcos Marín-Santibá nez, José Pérez-González, Lourdes de Vargas, Francisco Rodríguez González, and Guadalupe Huelsz. Rheometry-piv of shear-thickening wormlike micelles. *Langmuir*, 22:4015–4026, 2006.

[83] Arturo F. Méndez-Sánchez, Jóse Pérez-González, Lourdes de Vargas, J. Rafael Castrejón-Pita, Alfonso A, Castrejón-Pita, and Guadalupe Huelsz. Particle image velocimetry of the unstable capillary flow of a micellar solution. *Journal of Rheology*, 47:1455–1466, 2003.

[84] Shi-Qing Wang, S. Ravindranath, and P. E. Boukany. Homogeneous shear, wall slip, and shear banding of entangled polymeric liquids in simple-shear rheometry: A roadmap of nonlinear rheology. *Macromolecules*, 44:183–190, 2011.

[85] Shaden Jaradat, Matthew Harvey, and Thomas A. Waigh. Shear-banding in polyacrylamide solutions revealed via optical coherence tomography velocimetry. *Soft Matter*, 8:11677–11686, 2012.

[86] J. Y. Lee, G. G. Fuller, N. E. Hudson, and X.-F. Yuan. Investigation of shear-banding structure in wormlike micellar solution by point-wise flow-induced birefringence measurements. *Journal of Rheology*, 49(2):537 –550, 2005.

[87] J.P. Decruppe, R. Cressely, R. Makhloufi, and E. Cappelaere. Flow birefringence experiments showing a shear-banding structure in a ctab solution. *Colloid and Polymer Science*, 273(4):346–351, 1995.

[88] R. W. Mair and P. T. Callaghan. Observation of shear banding in worm-like micelles by nmr velocity imaging. *EuroPhysics Letters*, 36(9):719–724, 1996.

[89] Matthew E. Helgeson, Lionel Porcar, Carlos Lopez-Barron, and Norman J. Wagner. Direct observation of flow-concentration coupling in a shear-banding fluid. *Physical Review Letters*, 105(084501):1–4, 2010.

[90] Soroush Hooshyar and Natalie Germann. A thermodynamic study of shear banding in polymer solutions. *Physics of Fluids*, 28(063104), 2016.

[91] T. Chinyoka. Suction-injection control of shear banding in non-isothermal and exothermic channel flow of johnson-segalman liquids. *ASME Journal of Fluids Engineering*, 133(7):1–12, 2011.

[92] I.E. Ireka and T. Chinyoka. Non-isothermal flow of a johnson-segalman liquid in a lubricated pipe with wall slip. *Journal of Non-Newtonian Fluid Mechanics*, 192:20–28, 2013.

[93] I.E. Ireka and T. Chinyoka. Analysis of shear banding phenomena in non-isothermal flow of fluids governed by the diffusive johnson-segalman model. *Applied Mathematical Modelling*, 40:3843–3859, 2016.

[94] P. Español, X.F.Yuan, and R.C. Ball. Shear banding flow in the johnson-segalman fluid. *Journal of Non-Newtonian Fluid Mechanics*, 65:93–109, 1996.

[95] Paul F. Salipante, Charles A. E. Little, and Steven D. Hudson. Jetting of a shear banding fluid in rectangular ducts. *Physical Review Fluids*, 3(2):1–41, 2017.

[96] Eugene Helfand and Glenn H. Fredrickson. Large fluctuations in polymer solutions under shear. *Physical Review Letters*, 62(21):2468–2471, 1989.

[97] Y. T. Hua, C. Palla, and A. Lips. Comparison between shear banding and shear thinning in entangled micellar solutions. *Journal of Rheology*, 52:379–400, 2008.

[98] S.M. Fielding and P.D. Olmsted. Flow phase diagrams for concentration-coupled shear banding. *European Physics Journal E*, 11, 2003.

[99] J. M. Adams and P. D. Olmsted. Nonmonotonic models are not necessary to obtain shear banding phenomena in entangled polymer solutions. *Physical Review Letters*, 102:1–4, 2009.

[100] J. M. Adams andS. M. Fielding and P. D. Olmsted. Transient shear banding in entangled polymers: a study using the rolie-poly model. *Journal of Rheology*, 5(55):1007–1032, 2011.

[101] Michael Cromer, Michael C. Villet, Glenn H.Fredrickson, L.Gary Leal, and Roman Stepanyan. Concentration fluctuations in polymer solutions under extensional flow. *Journal of Rheology*, 57(4):1211 –1235, July/August 2013.

[102] Joseph D. Peterson, Michael Cromer, Glenn H. Fredrickson, and L. Gary Leal. Shear banding predictions for the two-fluid rolie-poly model. *Journal of Rheolology*, 60:927–951, 2016.

[103] Natalie Germann, A. Kate Gurnon, Lin Zhou, L. Pamela Cook, Antony N. Beris, and Norman J. Wagner. Validation of constitutive modeling of shear banding, threadlike wormlike micellar fluids. *Journal of Rheology*, 60(5):983–999, 2016.